UNIVERSITY OF COPENHAGEN

MSc in Quantum Physics

Whispering-gallery-modes in QD-embedded micro disc resonators for optical routing

Arianne Brooks

Supervised by Nir Rotenberg, Leonardo Midolo and Peter Lodahl

In close collaboration with Xiao-Liu Chu

September 2021

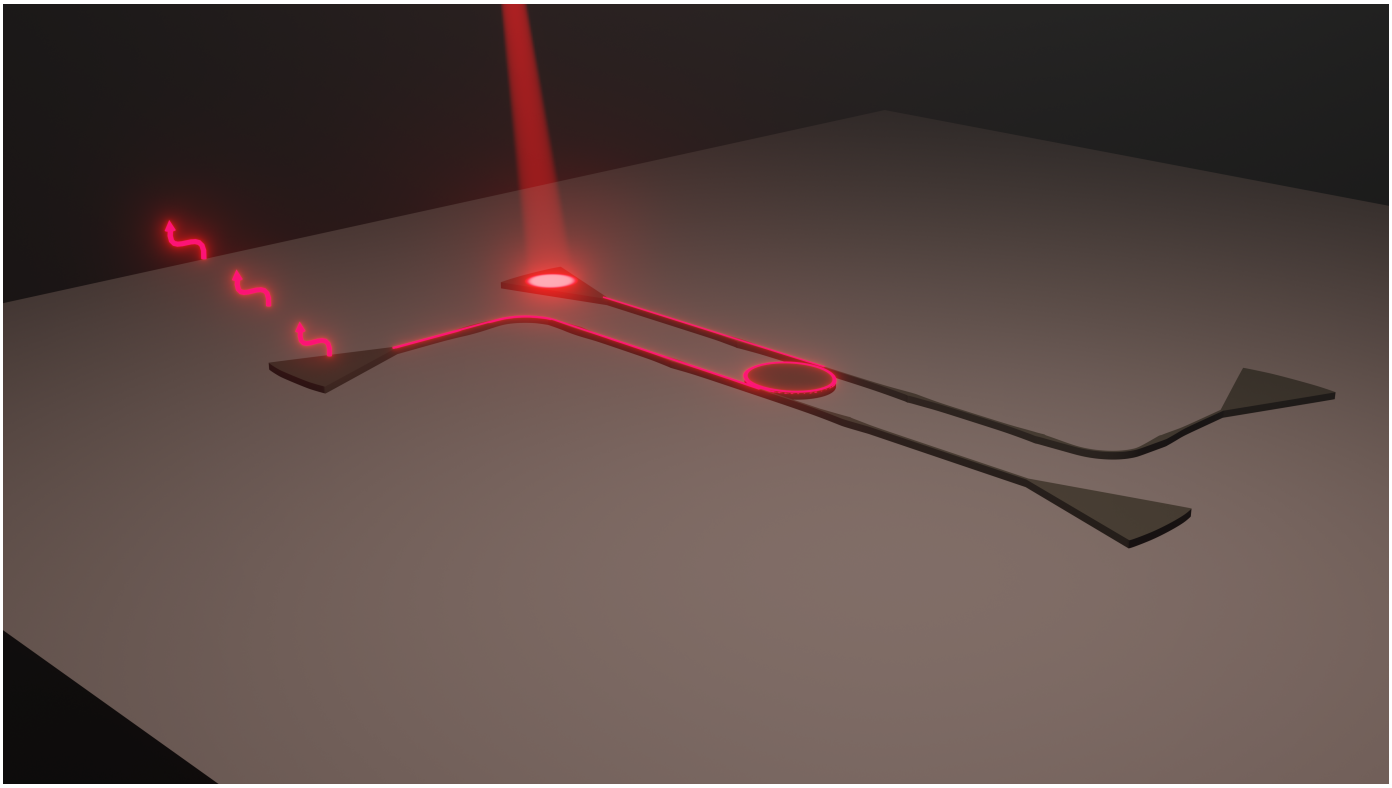

Arianne Brooks

Whispering-gallery-modes in QD-embedded micro disc resonators for optical routing

MSc in Quantum Physics, September 2021

Supervisors: Nir Rotenberg, Leonardo Midolo and Peter Lodahl

University of Copenhagen

Niels Bohr Institute

Masters Degree in Quantum Physics

Blegdamsvej19

2200 Copenhagen N

Acknowledgements

First and foremost, I would like to thank Prof. Peter Lodahl for granting me the opportunity to work with such an exciting project and for the interesting and helpful discussions we have had throughout the course of my project. I furthermore want to thank my primary supervisor, Prof. Nir Rotenberg, for conceiving the project and believing in me and pushing me whenever I needed it. Our conversations throughout the years, be it about physics or life, always turn out interesting. I also want to thank Prof. Leonardo Midolo for taking on the role as my new supervisor in a time that was *very* busy. A special thanks goes out to Zhe Liu who has trained me in the cleanroom. Your patience is a true virtue! In addition, I want to thank Aslı Uğurlu for joining me in my epoxy-adventure in the cleanroom as well as late-night beer drinking and dancing at your family house.

It takes a forest to perform decent quantum experiments, and I want to thank the entire Quantum Photonics group for all of your inputs and battles fought alongside me. Who knew fibers and cryostats had minds of their own?

I furthermore want to express my gratitude towards my friends, many of which have had to hear me speak about photons and lasers for durations that could not have been healthy. Thank you for encouraging me and thank you for asking so many questions!

My absolutely biggest thanks goes out to Dr. Xiao-Liu Chu, without whom this project would have been a lesser version of itself. Your knowledge and your drive has been a constant inspiration for me. In research as well as in life, I often find myself thinking "What would Liu do now?". So thank you for your patience, your ideas, your constructive criticism and thank you for doing this project with me.

Abstract

The field of quantum information technology has vastly expanded over the past decades, and planar quantum photonic circuits are paving the way for a big-scale integrated quantum network. One key element in photonic circuits is the generation and control of single-photons and their coherent interaction with nodes across the network. Tailored photonic resonators allow enhancing light-matter interaction, ultimately leading to a fully coherent quantum interface. In this work we present the design, fabrication and characterisation of an integrated whispering-gallery-mode micro disc resonator coupled to an embedded quantum dot single-photon emitter. The cavity-emitter system is shown to coherently route photons between two different access waveguides with a measured routing efficiency of $\Delta I = (23 \pm 3)\%$ while having a Purcell factor of $F = (6.9 \pm 0.9)$ with a cavity quality factor of approximately $10,000$. We show how the routing can be controlled through detuning of the quantum dot and the resonator, and that the fabricated device operates at a critical photon number < 1. We discuss the strengths and limitations of the device and focus on an optimisation of the device that includes electrically contacting the disc resonators in order to reduce charge noises and control the bandgap of the quantum dot. Electrically contacting of the disc resonators require the crossing of metal wire onto the disc. As the wire will intersect with suspended nanoscale structures and confined optical modes, issues concerning mode loss due to absorption and scattering arise, thus introducing another bottleneck in the upscaling of quantum photonic circuits. In this work, we furthermore propose a robust fabrication process for realising crossings between suspended planar photonic structures embedded with quantum emitters and metal wires. The proposal includes the fabrication of > 1 μm thick polymer epoxy claddings across the disc resonators. Initial results indicates a low amount of loss introduced by the claddings, and quality factors of $> 30,000$ are measured in the cladded disc resonators.

Contents

1 Introduction

The rapid evolution of classical information technology has defined the modern world where global and instantaneous communication is essential. Since the beginning of the 21st century, internet in the form of short optical pulses has protruded and become a key implementation in most homes and institutions, as it enables worldwide connectivity and data sharing. For such a classical network, information is stored in bits which take the values 0 or 1. A series of bits can encompass any classical information, examples being an image, a text message or a set of data. Transmission of sensitive data can be secured by using encryption and security protocols. Classical encryption is, however, not infallible, and suffers from weaknesses that are seemingly difficult to overcome within the classical regime of operation. In the wake of the revolutionary developments of quantum mechanics throughout the 20th century, the *quantum internet* embodies a new frontier of modern day technology, as it enables security applications that are fundamentally unreachable for the classic internet [1]–[3]. The quantum internet distinguishes itself from the classical by encoding the information in *qubits*, which can take not only the states $|0\rangle$ or $|1\rangle$ but also any superposition of the two states. In addition, a special correlation between the two states can be manifested in which the states are *entangled* [4]. A well-known application of the quantum internet is quantum key distribution (QKD), where an encryption key relies on the entanglement of a pair of qubits [5]. A key element of QKD rests on the quantum mechanical "no-cloning theorem", which states that the sent information carrier is unique [6]. Upon receival of the information, the sender and receiver are certain that no so-called eavesdropper has acquired the information too [7]; a principle fundamentally impossible to impose within the classical regime. A global network of QKD would require large-scale generation and distribution of entangled qubits across the globe, both of which can in principle be achieved by heralded entanglement generation as well as entanglement swapping in quantum repeaters. These protocols can be realised with an optical Bell state analyser [8]. The realisation of a Bell state analyser requires a fast optical router [9]. In this thesis we will design, fabricate and characterise disc resonators which are shown to operate as single-photon routing devices.

Optical routing is one out of several constituents of a quantum network, other components being a source of single photons, phase shifters or single-photon detectors [10]–[12]. In combination, these devices can form an integrated photonic quantum circuit [10]. Individual elements of an on-chip quantum circuit have been realised with prosperous success, including the generation of pure and highly indistinguishable photons [13]. The disc resonators discussed in this thesis are fabricated on-chip and are thus compatible with the integration of quantum circuits [14]. Efforts towards integrating an entire quantum circuit on a single chip include designing and optimising several micro- and nanoscale devices. Fig. 1.1 depicts how the individual components, including an optical router, can ultimately be joined into a full circuit.

An operational chip will potentially contain a great magnitude of devices that are all to be interconnected. However, issues concerning the scaling of the quantum photonic integrated circuits are yet to be addressed.

Several nanoscale devices require electrical contacting, and the ability to build electrical intersections that can cross devices on the chip without reducing transmission efficiency is paramount towards further scaling of the technology [15]. Using the disc resonators designed and fabricated within this work, we furthermore propose a robust fabrication process for realising intersections between metal wires and photonic nanoscale devices, such that individual photonic devices can be electrically accessed without introducing significant transmission losses.

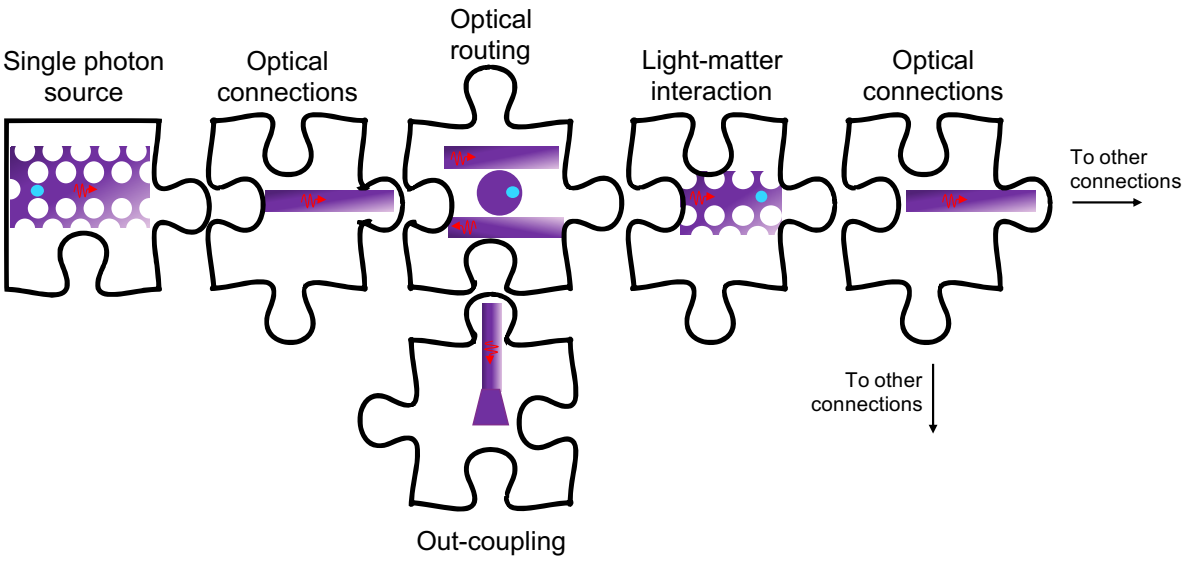

Figure 1.1.: Conceptual depiction of quantum photonic circuit. Various photonic components, including a single photon source using a quantum dot (blue), waveguides and optical routers, integrated into one chip will serve as a controllable photonic circuit.

The outline of this thesis is as follows. In Ch. 2 a theoretical foundation of the disc resonators is presented in which we see how these devices will function as single-photon routers. The chapter includes a theoretical model describing the transmission of light through the designed resonator devices, numerical simulations estimating device specific properties, and an introduction to the quantum emitters used throughout this work.

In order to realise single-photon routing, the disc resonators are designed and fabricated. Ch. 3 outlines the employed fabrication techniques for the construction of the resonators studied in this work. In particular, we introduce common lithographic methods and standard fabrication protocols including etching methods and metal deposition. We then propose and optimise a novel method of accessing individual isolated nanophotonic devices with metal wires as well as creating wire intersections by using epoxy claddings as bridges.

In Ch. 4 we present the optical setup used for characterising the fabricated samples. More specifically, two main methods of exciting the quantum emitters are discussed. Additionally, we discuss the optical properties of the devices designed and fabricated within this work. Lastly, we present an analysis of the parameters of the resonators and their effect on device performance. This chapter serves as an overview of the average functionality of the disc resonators fabricated in this work.

Experimental results from coupled cavity-emitter systems are presented in Ch. 5. Initially, we present methods to establish cavity-emitter coupling along with a statistical analysis of emitter decay rates within the devices. Sequentially, we study a distinguished cavity-emitter system and extract important figures of merit, such as coupling strength, system cooperativity, and routing efficiency, for this particular cavity-emitter system. The chapter is concluded with several future implementations to ultimately improve the system efficiency.

One path towards improving the routing efficiency of the devices is to electrically contact the disc resonators. Experimental results of initial investigations of electrically contacting the disc resonators are presented in Ch. 6. We investigate the possibility of leading a metal wire onto isolated resonators using epoxy claddings as bridges. By optically characterising epoxy cladded disc resonators we gauge the losses introduced by the epoxy structures.

Finally, conclusions and outlook of the work are presented in Ch. 7.

2 Theoretical background of whispering gallery modes

Throughout this chapter we will be presenting the theoretical foundation of the cavity-based experiments performed in this work. Firstly, we introduce basic cavity quantum electrodynamics (CQED). Important figures of merit within the photonics and quantum information community, such as cavity quality factor, cavity-emitter coupling strength and emitter cooperativity, will be described. Being an extensively studied field of research, the CQED described in this chapter has a vast basis of literature in both classical textbooks [16]–[18] as well as state-of-the-art publications [19]–[21]. Secondly, we demonstrate numerical simulations of the system studied throughout this work and estimate quality factors and mode volumes. Lastly, we introduce the theoretical foundation of the quantum emitters used in this work.

2.1 Cavity quantum electrodynamics

Optical resonators confine light at resonance frequencies according to the geometry of the cavity. Light will be transmitted or reflected depending on the properties of the resonator. The simplest cavity designs, Fabry-Perot cavities [16], can be helpful to understand more complex cavity configurations such as the micro discs that are the focus of this thesis.

Two mirrors form a simple cavity as depicted in Fig. 2.1a. By solving the Helmholtz equation it becomes clear that the cavity will support a discrete set of resonant modes, $f_{\mathrm{res},1},...,f_{\mathrm{res,n}}$, depending on the configuration of the cavity. The spectral separation of the modes is called the Free Spectral Range (FSR) and is dependent on the cavity properties as well as the frequency of the electromagnetic field:

$$FSR = \frac{\lambda^2}{nL} \tag{2.1}$$

Here λ is the wavelength of the mode, L is the length of the cavity and n is the refractive index of the material within which the mode propagates. The reflective and transmittive properties of the cavity determine whether the light stays in the cavity or is transmitted out. Assuming a non-ideal cavity, light will leak out of the cavity due to loss-mechanisms that will be discussed more in detail in later chapters. The loss-rate is described by κ and effectively broadens the cavity modes from discrete single-frequencies to a Lorentzian lineshape of frequencies [16]:

$$L(f) = \frac{1}{\eta} \frac{\frac{1}{2}\kappa}{(f - f_{\mathrm{res}})^2 + \left(\frac{1}{2}\kappa\right)^2}, \tag{2.2}$$

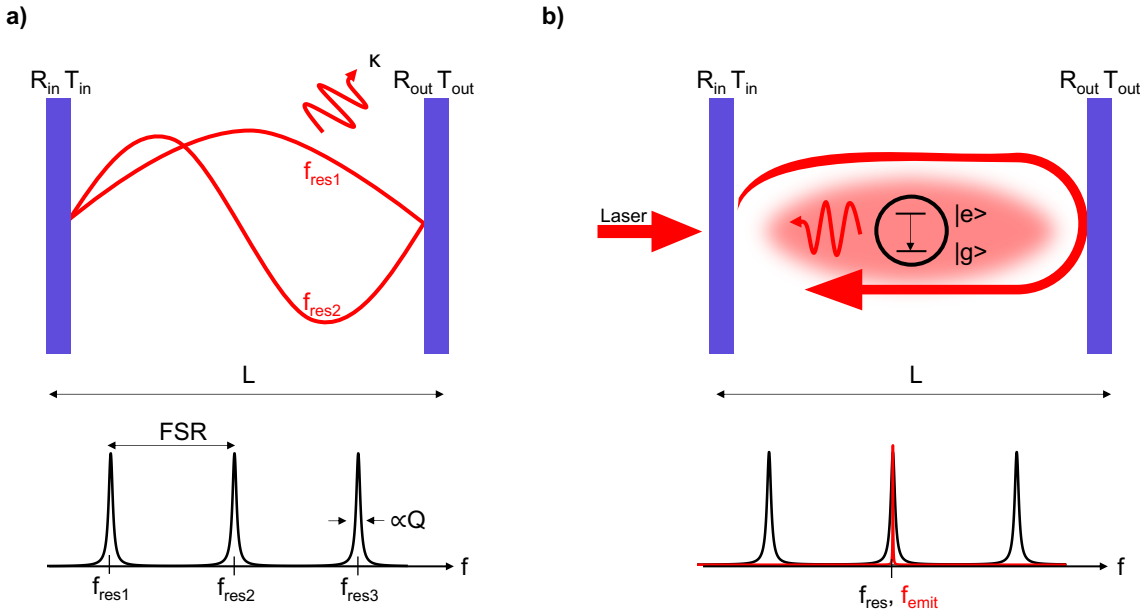

Figure 2.1.: Cavity quantum electrodynamics: a) A Fabry-Perot cavity consisting of two mirrors will support various spectral modes $f_{res,n}$ determined by the geometry of the cavity given by the length L. The frequency separation between the modes is called the Free Spectral Range (FSR). Transmission into and out of the cavity is controlled by reflection and transmission coefficients R and T. Mode losses are given by κ which will determine the spectral width of the cavity response and scales with the quality factor Q. b) Modes resonant with the cavity are transmitted from the laser into the cavity. A cavity enhances the Local Density of Optical States (LDOS) surrounding an emitter placed within the cavity, thus enhancing the decay rate of the emitter. A well-coupled emitter decays primarily into the cavity mode.

where f is frequency. Here, η is a normalisation factor. The quality factor (Q-factor) of the cavity is determined by the loss-rate and can be written as:

$$Q = \frac{f_{\text{res}}}{\kappa} \tag{2.3}$$

A high-Q cavity will confine resonant modes for a large number of round trips within the cavity. In practice, the Q-factor of cavities depends primarily on material surface roughness, as roughness will serve as scattering points for the resonant modes, and on material absorption. The choice of material highly influences the obtainable Q-factors. Planar silicon (Si) microdisc resonators have been reported to achieve Q-factors $> 10^6$ [22]. Within this work, we will be using gallium arsenide ($GaAs$) structures which have been reported to have Q-factors in the order of $\approx 10^4$ [23]–[26].

2.1.1 Purcell factor and coupling strength

A key element within quantum information processing is the realisation of a scalable network of qubits [10]. A promising approach is to encode information within single photons. As photons cannot interfere in vacuum, they need nodes of material to enable interaction, thus allowing operations to be performed

within the network. Within this work we will be using a coherent two-level system (TLS) as the interacting node of matter.

The derivation in this section will initially follow that of [17], but as the results are not new, we will mostly be highlighting important equations.

The essential property of a TLS is the spontaneous emission. The emitter depicted within the cavity in Fig. 2.1b is a TLS with a ground state $|g\rangle$ and an excited state $|e\rangle$. The energy separation is given by $\Delta E = \hbar\omega_{eg}$. Transitions between the states are given by the atomic creation and annihilation operators, $\hat{\sigma}_{eg} = |e\rangle\langle g|$ and $\hat{\sigma}_{ge} = |g\rangle\langle e|$, respectively. The quantised light field is given by

$$\hat{\mathbf{E}} = \mathcal{E}_0(\hat{a} - \hat{a}^\dagger), \tag{2.4}$$

where $\mathcal{E}_0 = i\left(\frac{\hbar\omega}{2\varepsilon_0 V}\right)^{1/2}\mathbf{e}$, where $\mathbf{e}$ is arbitrarily oriented polarisation vector, V is the mode volume and ω is the field frequency. Furthermore, we have introduced the field creation and annihilation operators operating on number states, $|n\rangle$:

$$\hat{a}^\dagger|n\rangle = \sqrt{n+1}\,|n+1\rangle \tag{2.5a}$$

$$\hat{a}|n\rangle = \sqrt{n}\,|n-1\rangle \tag{2.5b}$$

By applying an electric field to a TLS we perturb the system by altering the momentum of the emitter. Light-matter interaction with a TLS is described by the Jaynes-Cummings Hamiltonian:

$$\hat{\mathcal{H}}_{\mathrm{JC}} = \hbar\omega_{eg}\hat{\sigma}_{eg}\hat{\sigma}_{ge} + \hbar\omega\hat{a}\hat{a}^\dagger + \hbar g(\hat{a}^\dagger\hat{\sigma}_{ge} + \hat{a}\hat{\sigma}_{eg}) \tag{2.6}$$

Here, the first term is the atomic Hamiltonian term while the second term accounts for the field dynamics at frequency ω. The last term is called the *interaction Hamiltonian*. Here, we introduce the coupling strength, g:

$$g = -\sqrt{\frac{\hbar\omega}{\varepsilon_0 V}}\hat{\mathbf{d}}\cdot\mathbf{e} \tag{2.7}$$

The coupling strength depends on the scalar product of the dipole moment operator $\hat{\mathbf{d}}$ and the electric field polarisation. Using Fermi's Golden Rule we can extract a spontaneous decay rate of a TLS in free space [17]:

$$\Gamma_{\mathrm{fs}} = \frac{d^2\omega^3}{3\pi\varepsilon_0\hbar c^3} \tag{2.8}$$

Here, d is defined as $d = \langle e|\,\hat{d}\,|g\rangle$. By time-evolving the Schrödinger Equation of the system in the Interaction picture we are able to find the complex expansion coefficients of the system, $c_{|2,n\rangle}$ and $c_{|1,n+1\rangle}$, representing lower and higher excited state respectively. From these, we can find the probability of finding the emitter in a given state such as:

$$P_{|1,n+1\rangle}(t) = |c_{|1,n+1\rangle}(t)|^2 = \frac{1}{2}(1+\cos(\Omega_n t)) \tag{2.9}$$

Here, $\Omega_n = 2g\sqrt{n+1}$ is the quantised Rabi oscillation. We see that Ω_n depends linearly on the coupling strength. Until now, we have analysed the spontaneous emission of a TLS due to interaction with a

light field. We will now show that by placing the emitter within an optical cavity we can increase the coupling strength and thereby increase the spontaneous decay rate. The schematics of the system is depicted in Fig. 2.1b. The cavity mirrors have a finite reflectivity resulting in a cavity loss rate κ. The interaction Hamiltonian within a leaky cavity can be written as:

$$\hat{\mathcal{H}}_{\text{Int}} = \hbar\lambda(\hat{a}\hat{\sigma}_{eg} + \hat{a}^{\dagger}\hat{\sigma}_{ge}), \tag{2.10}$$

Here, $\lambda = -\frac{d}{\hbar}\sqrt{\frac{\hbar\omega_{eg}}{\varepsilon_0 V}}\sin(\mathbf{k}\cdot\mathbf{z})$. This additionally yields a coupling strength of:

$$g = \sqrt{\frac{\hbar\omega}{\varepsilon_0 V}}\sin(kz) \tag{2.11}$$

We see that the coupling strength now depends on the physical position of the emitter within the cavity, as the position at a modal node would result in no interaction, while a position at a field maximum would result in maximal interaction. We introduce the dissipation term when writing out the master equation for the evolution of the density operator:

$$\frac{d\hat{\rho}}{dt} = -i\hbar[\hat{\mathcal{H}}_{\text{Int}}, \hat{\rho}] \underbrace{-\frac{\kappa}{2}(\hat{a}^{\dagger}\hat{a}\hat{\rho} + \hat{\rho}\hat{a}\hat{a}^{\dagger}) + \kappa\hat{a}\hat{\rho}\hat{a}^{\dagger}}_{\text{Dissipation}} \tag{2.12}$$

The equations $\frac{d\rho_{ij}}{dt}$ are called the Bloch Equations. From these we obtain:

$$\rho_{ij}(t) \approx Ae^{\Lambda_+ t} + Be^{\Lambda_- t} + Ce^{\Lambda_0 t} \tag{2.13}$$

Here, $\Lambda_\pm$ and Λ_0 are eigenvalues of ρ_{ij} and are given by:

$$\Lambda_0 = -\frac{\omega_{eg}}{2Q} \tag{2.14a}$$

$$\Lambda_\pm = -\frac{\omega_{eg}}{2Q}\left[1 + \pm\sqrt{1 - \frac{4\Omega_0^2 Q^2}{\omega_{eg}^2}}\right] \tag{2.14b}$$

Here, Ω_0 is the vacuum Rabi frequency. Looking at $\Lambda_\pm$ we note that the condition $\omega_{eg}/Q < 2\Omega_0$ would result in complex eigenvalues, yielding damped oscillations of the system. This corresponds to a weakly coupled cavity-emitter system. By applying a Taylor approximation, we obtain $\Lambda_+ \approx -\frac{\Omega_0^2 Q}{\omega_0}$. Knowing that $\Omega_0 = 2\lambda$ and $\lambda = dg/\hbar$ at field maximum combined with Eq. 2.11 we obtain:

$$\Lambda_+ \approx -\frac{4d^2 Q}{\hbar\varepsilon_0 V} \tag{2.15}$$

Assuming that the emitter is placed in a field maximum we can write the irreversible rate of decay as:

$$\Gamma_{\text{cav}} = \frac{4d^2 Q}{\hbar\varepsilon_0 V} \tag{2.16}$$

By applying Fermi's Golde Rule we furthermore know that the decay rate also can be written as $\Gamma_{\text{cav}} = \frac{\pi d^2}{\varepsilon_0\hbar^2}\rho_{\text{cav}}(\omega_0)\hbar\omega_0$. Using this knowledge, we can now write:

$$\rho_{\text{cav}}(\omega) = \frac{4Q}{\pi\varepsilon_0 V} \tag{2.17}$$

By comparing the spontaneous decay rate in free space with that within the cavity we obtain the expression for the emission enhancement, also called the Purcell factor:

$$F = \frac{\Gamma_{\text{cav}}}{\Gamma_{\text{fs}}} = \frac{4Q\lambda_0^3}{3\pi\varepsilon_0 V} \tag{2.18}$$

This expression was derived by Purcell in 1946 and is the corner stone of modern cavity quantum electrodynamics [27]. For our work we will write the Purcell factor in terms of the effective wavelength $\lambda_{\text{eff}} = \lambda/n$ and the effective mode volume, V_{eff} [28]:

$$F = \frac{3}{4\pi^2}\left(\frac{\lambda}{n}\right)^3\left(\frac{Q}{V_{\text{eff}}}\right) \tag{2.19}$$

It is clear that a high Q-factor and a minimal effective mode volume maximises the Purcell enhancement. The Q-factor can be optimsed during fabrication. The effective mode volume is minimised when the emitter is placed at the maximal intensity of the mode within the cavity.

The emitter used in the experiments conducted within this work consists of a single indium arsenide (InAs) quantum dot (QD). Let us consider an emitter in a homogeneous material. The spontaneous decay rate Γ can be described by a bulk decay rate, γ_{bulk}, at which the QD emits single photons. A QD will decay with a rate of:

$$\gamma_{\text{bulk}} = \gamma_0 + \gamma', \tag{2.20}$$

which corresponds to the radiative decay and non-radiative decay, respectively [29]. Even though high quantum efficiencies have been reported for QDs [29], [30], overall collection efficiency has been reported at 5% [31]. As discussed, by placing a resonant emitter in a cavity the emission of single photons is enhanced. Furthermore, collection efficiency of single photons is improved, as the resonant photons will couple to the cavity mode.

By coupling the QD to a cavity-system, its overall decay rate is modified according to the Purcell enhancement of the system. The modification to the decay can be described as:

$$\gamma_{\text{tot}} = \gamma_{\text{cav}} + \gamma_{\text{leak}} + \gamma' = F\gamma_0 + \gamma_{\text{leak}} + \gamma' \tag{2.21}$$

From Ref. [32] it has been reported that $\gamma_{\text{leak}} \approx \gamma_0$, which is an approximation that will be used throughout this thesis. We furthermore assume that the non-radiative decay within the cavity is small and approximate $\gamma' \approx 0$, thus allowing us to write:

$$\gamma_{\text{tot}} = (F+1)\gamma_{\text{bulk}} \tag{2.22}$$

As $\gamma_{\text{cav}} = F\gamma_{\text{bulk}}$, it is clear that a large Purcell enhancement enhances the total emission rate into the cavity mode.

A measure of efficiency of the cavity-QD system is the coupling efficiency β [33], which can be expressed as:

$$\beta = \frac{\gamma_{\text{cav}}}{\gamma_{\text{cav}} + \gamma_{\text{leak}}} = \frac{F}{F+1} \tag{2.23}$$

The β-factor is an important figure of merit within photonics, as a β-factor of ≈ 1 indicates high cavity-emitter coupling efficiency [34], which is necessary in order to realise a scalable quantum network. Recent reports have shown β-factors of (0.99 ± 0.01) in a photonic crystal waveguide [35].

As discussed, the cavity-emitter coupling strength will vary depending on cavity-emitter detuning, emitter placement according to the mode and dipole alignment with the mode, as seen by the interaction Hamiltonian. For cavity-QED, the coupling strength g can in fact be expressed in terms of the Purcell factor [36]:

$$g = \frac{\sqrt{F\kappa\gamma_{\text{bulk}}}}{2} \tag{2.24}$$

Within cavity-physics there is talk of two regimes of coupling; *strong coupling* and *weak coupling* [37], [38]. The different regimes of operation distinguish themselves based on the relationship between the linewidth of the cavity, κ, the linewidth of the emitter γ_{tot} and the coupling strength g. Strong coupling is obtained when $2g > \frac{(\kappa+\gamma_{\text{tot}})}{2}$, meaning that the light-matter interaction becomes larger than the combined dipole decay rate and the cavity field decay rate. The weak coupling regime occurs at $g < \gamma_{\text{tot}}, \kappa$ [39].

From the coupling strength it is possible to obtain the cooperativity, C [8]. For our system we obtain:

$$C = \frac{4|g|^2}{\kappa\gamma_{\text{bulk}}} \tag{2.25}$$

The cooperativity is an important parameter and describes the ratio of decay into the cavity modes versus the undesired decay into other modes. The cooperativity can furthermore be used to calculate the success rate of a cavity quantum electrodynamics-based Bell-state analyser [8]:

$$P_{\text{success}} = 1 - 1/C \tag{2.26}$$

A sustainable quantum network requires devices of high cooperativity, meaning that the coupling of the cavity-emitter system should be high for effective operation.

2.1.2 Coherent interaction of an emitter-cavity system

Having outlined the figures of merit of a coupled cavity-emitter system, we now turn to study the interaction model of the system. The theory explained and derived within this section has been published in a recent publication by this author and supervisors of this project. The derivation here will follow that of the publication [40] along with publications with similar systems [36], [41].

Throughout literature several interesting emitter-cavity systems have been successfully characterised, such as $InAs$ QD-embedded micropillars [38] and microdiscs [42] and bottle microresonators coupled to a single atom [19]. While these experiments have shown high Q-factors and strong coupling, similar experiments have not yet[1] been performed in combination with on-chip integration showing coherent single-photon routing. In this project we are working with Whispering Gallery Modes (WGM) in on-chip integrated QD-embedded microdisc resonators coupled to access waveguides as depicted in

[1] To the best of this author's knowledge

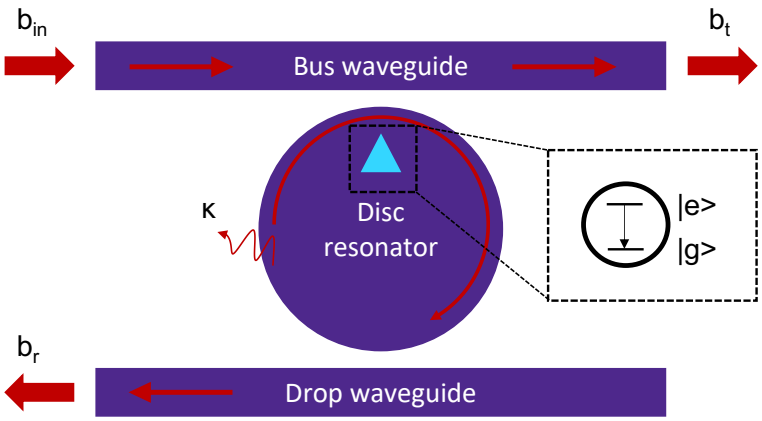

Figure 2.2.: Schematic setup of microdisc resonator coupled to a bus and drop waveguide. An incoming light field, b_{in}, is sent in through the bus waveguide. Assuming critical coupling between waveguide and disc resonator, all resonant light will couple to the resonator while off resonant fields will be transmitted through the bus waveguide and exit as b_{t}. Within the resonator light can be scattered out of the cavity due to a finite Q-factor or be coupled out through either waveguide. The outcoupling from the disc will depend on the coupling between disc and access waveguides. Modes emitted into the drop waveguide are denoted b_{r}.

the schematics of Fig. 2.2. The following theory will outline how emission from a coupled cavity-QD system can be routed between channels within a circuit.

In Fig. 2.2 the field is initially sent through the *bus* waveguide. If on resonance, the field can couple to the disc resonator and couple out of the *drop* waveguide. We expect to observe cavity-emitter behaviour as described in the previous section with transmission T measured through the bus port and with reflection R measured through the drop port.

Having shown the basis of light-matter interaction in the previous section, we now follow the approach of [41]. From this, a theoretical model based on our system depicted in Fig. 2.2 can be derived. The cavity-QD interaction can be described by the rate equations of the system:

$$\dot{s} = -i\Delta\omega s - \frac{\Gamma}{2}\frac{Q}{Q_0}\left[t_0 + \frac{1}{f}\right]s + i\frac{Q}{Q_0}\sqrt{\frac{\Gamma}{2}}(2s_z)b_{\text{in}}t_0 \tag{2.27a}$$

$$\dot{s}_z = -\Gamma\frac{Q}{Q_0}\left[\text{Re}(t_0) + \frac{1}{f}\right]\left(s_z + \frac{1}{2}\right) + \sqrt{\frac{\Gamma}{2}}\frac{Q}{Q_0}[is^* b_{\text{in}}t_0 + c.c.] \tag{2.27b}$$

$$b_{\text{t}} = -\frac{Q}{Q_0}t_0 b_{\text{in}} - i\frac{Q}{Q_0}\sqrt{\frac{\Gamma}{2}}t_0 s \tag{2.27c}$$

$$b_{\text{r}} = \left(1 - \frac{Q}{Q_0}t_0\right)b_{\text{in}} - i\frac{Q}{Q_0}\sqrt{\frac{\Gamma}{2}}t_0 s \tag{2.27d}$$

Here, b_{t} is the outgoing field while b_{in} is the incoming field amplitude. Q is the total quality factor including coupling to leaky modes while Q_0 is the intrinsic quality factor of the cavity. The laser-emitter

detuning of the driving field is given by $\Delta\omega = \omega_{\text{laser}} - \omega_{\text{emitter}}$. Γ is the decay rate of the emitter to the cavity mode, meaning that $\Gamma = \gamma_{\text{cav}}$. The atomic operators $S_z = (|e\rangle\langle e| - |g\rangle\langle g|)/2$ and $S_- = |g\rangle\langle e|$ are considered to have expectation values of $s = \langle S_- \rangle$ and $s_z = \langle S_z \rangle$. The transmission factor t_0 is the response of the bare cavity in the absence of an emitter and is given by:

$$t_0 = \frac{1}{1 + i\frac{\Delta\omega+\delta}{\kappa}\frac{Q}{Q_0}}, \tag{2.28}$$

where κ is the cavity loss rate and thereby the linewidth while δ is the cavity-emitter detuning. Finally, the parameter f describes the ratio of decay rates into cavity modes versus all other decay rates:

$$f = \frac{\Gamma}{\gamma_{\text{leak}} + 2\gamma_{\text{dp}}} \tag{2.29}$$

Here, γ_{leak} is the rate of leaky modes out of the cavity and γ_{dp} is the pure dephasing rate, which we attribute to heat-induced phonon interaction. A steady state solution to s and s_z can be found by setting $\dot{s} = 0$ and $\dot{s}_z = 0$, ultimately resulting in:

$$s = -\frac{\frac{4}{\gamma_{\text{wg}}} i\Omega s_z t_0}{t_0 + \frac{\gamma_{\text{rad}}+2\gamma_{\text{dp}}}{\gamma_{\text{wg}}} + \frac{2i\Delta\omega}{\gamma_{\text{wg}}}} \tag{2.30a}$$

$$s_z = -\frac{1}{2}\left(\frac{1}{1 + \frac{|b_{\text{in}}|^2}{P_{\text{c}}}}\right) \tag{2.30b}$$

In order to reach this steady state solution we have used $Q = Q_0$ and $f = \frac{\gamma_{\text{wg}}}{\gamma_{\text{leak}}} + \gamma_{\text{dp}}$. P_{c} is the critical power required to reach $s_z = -\frac{1}{4}$ and scales with the photon flux.

$$P_{\text{c}} = \frac{\Gamma}{4}\left[\left(1 + \frac{1}{f}\right)^2 + \left(\frac{Q}{Q_0}\frac{\Delta\omega+\delta}{\kappa f}\right)^2 - \frac{4\Delta\omega}{\Gamma}\frac{\Delta\omega+\delta}{\kappa} + \left(\frac{Q_0}{Q}\frac{2\Delta\omega}{\Gamma}\right)^2 + \left(\frac{2\Delta\omega}{\Gamma}\frac{\Delta\omega+\delta}{\kappa}\right)^2\right] \tag{2.31}$$

We can write the critical Rabi frequency as:

$$\Omega_{\text{c}}^2 = \frac{\gamma_{\text{wg}} P_{\text{c}}}{2} \tag{2.32}$$

The critical photon number thus becomes:

$$\begin{aligned} n_{\text{c}} &= 2\frac{\Omega_{\text{c}}^2}{\gamma_{\text{wg}}^2} = \frac{P_{\text{c}}}{\gamma_{\text{wg}}} \\ &= \frac{\Gamma}{4\gamma_{\text{wg}}}\left[\left(1 + \frac{1}{f}\right)^2 + \left(\frac{Q}{Q_0}\frac{\Delta\omega+\delta}{\kappa f}\right)^2 - \frac{4\Delta\omega}{\Gamma}\frac{\Delta\omega+\delta}{\kappa} + \left(\frac{Q_0}{Q}\frac{2\Delta\omega}{\Gamma}\right)^2 + \left(\frac{2\Delta\omega}{\Gamma}\frac{\Delta\omega+\delta}{\kappa}\right)^2\right] \end{aligned} \tag{2.33}$$

The atomic population then becomes:

$$s = i\frac{Q}{Q_0}\sqrt{\frac{\Gamma}{2}} b_{\text{in}} t_0 \frac{1}{1+S}\frac{1}{i\Delta\omega + \frac{Q}{Q_0}\frac{\Gamma}{2}\left(t_0 + \frac{1}{f}\right)}, \tag{2.34}$$

where $S = \alpha\frac{|b_{\text{in}}|^2}{P_{\text{c}}}$ is the saturation parameter containing the coupling efficiency α that relates the amount of incoming light to the amount that reaches the cavity, meaning that an ideal lossless system will have $\alpha = 1$. From this we can express the saturation parameter as:

$$S = \alpha\frac{n_{\text{in}}}{n_{\text{c}}}, \tag{2.35}$$

where $n_{\mathrm{in}} = |n_{\mathrm{in}}|^2/\gamma_{\mathrm{tot}}$ is the incident number of photons per lifetime (proportional to the input power) and $n_{\mathrm{c}} = P_{\mathrm{c}}/\gamma_{\mathrm{tot}}$ is the critical number of photons per lifetime, where γ_{tot} is the total decay rate of the emitter. Throughout this thesis we are working with leaky cavities where the emitter couples to leaky modes with a rate of γ_{leak} while also experiencing pure dephasing at the rate γ_{dp}. Assuming that coupling of light to the cavity only occurs via the waveguides, a transmission and reflection coefficient can be written as:

$$t_{\mathrm{drop}} = \frac{b_{\mathrm{t}}}{b_{\mathrm{in}}} = \frac{Q}{Q_0} t_0 \left[-1 + \frac{f}{(1+S)\left(f + \left(1 + \frac{2i\Delta\omega}{\gamma_{\mathrm{leak}}+2\gamma_{\mathrm{dp}}}\frac{Q_0}{Q}\right)\right)\left(1 + i\frac{\Delta\omega+\delta}{\kappa}\frac{Q}{Q_0}\right)} \right] \tag{2.36a}$$

$$t_{\mathrm{bus}} = 1 + t_{\mathrm{drop}} \tag{2.36b}$$

$$T_{\mathrm{drop}} = |t_{\mathrm{drop}}|^2 \tag{2.36c}$$

$$T_{\mathrm{bus}} = |t_{\mathrm{bus}}|^2 \tag{2.36d}$$

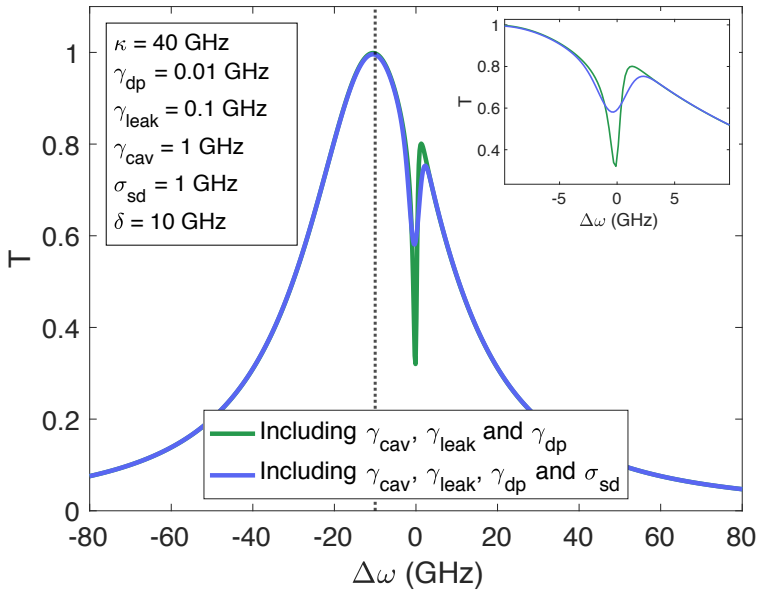

Figure 2.3.: Theoretical transmission T through disc resonator coupled to bus and drop waveguide using realistic values of cavity and emitter linewidths. Green: Including pure dephasing, γ_{dp}, as in Eq. 2.36a. Blue: Including pure dephasing, γ_{dp} and spectral diffusion σ_{sd} , as in Eq. 2.38. Inset shows zoom-in of transmission dip.

Assuming no further decoherence mechanisms, Eq. (2.36)a-b would fully describe the transmittive and reflective properties of a bus/drop disc resonator setup, and an example is depicted by the green line in Fig. 2.3. Here, we see that the coherent emitter interference creates a dip in transmission (in drop port), which we will term the QD-extinction. The depth of the dip is determined by the emission into bulk modes as well as the decoherence mechanisms and effectively determines the routing efficiency of the system. Within this work, we encounter charge noise within the emitters resulting in spectral diffusion. Spectral diffusion is a time-dependent evolution of the expectation value of the emitter

resonance and can be accounted for by convoluting the emitter dependent elements of Eq. 2.36 with a Gaussian distribution with a variance corresponding to the spectral width of the spectral diffusion, σ_{sd}. This will create a broadening of the emission linewidth which can be described by a Gaussian probability distribution [43]:

$$P(\sigma_{\mathrm{sd}}) = \frac{1}{\sqrt{2\pi}\sigma_{\mathrm{sd}}}\exp\left(-\frac{1}{2}\left(\frac{\Delta\omega-\delta}{\sigma_{\mathrm{sd}}}\right)^2\right) \tag{2.37}$$

For our systems, the cavity linewidths are expected to be much larger than the rate of the spectral diffusion while comparable to the linewidth of the enhanced emission rate. From this it follows that a spectral diffusion convolution including the entire cavity-emitter system does not affect the cavity linewidth but only causes broadening effects to the emitter, as is explained in Appendix A. Including the spectral diffusion, the final transmission of light through the bus/drop disc resonator will adhere to the following lineshape:

$$T_{\mathrm{drop}} = \left|\left(t_0\left[-1+\frac{f}{(1+S)\left(f+\left(1+\frac{2i\Delta\omega}{\gamma_{\mathrm{leak}}+2\gamma_{\mathrm{dp}}}\right)\right)\left(1+i\frac{\Delta\omega+\delta}{\kappa}\right)}\right]\right)\right|^2 * P(\sigma_{\mathrm{sd}}) \tag{2.38}$$

This is depicted by the blue line in Fig. 2.3. Here, we see that the depth of the transmission dip has been reduced by introducing spectral diffusion to the system. From the inset we see that spectral diffusion not only alters the transmission depth but also broadens the total linewidth of the emitter. As the cavity and access waveguide are not necessarily optimally coupled we furthermore introduce a normalisation factor, χ, accounting for the unnormalised count rate, which will determine the cavity transmission extinction in the bus port:

$$T_{\mathrm{bus}} = \chi|t_{\mathrm{bus}}|^2 * P(\sigma_{\mathrm{sd}}) \tag{2.39}$$

In conclusion, based on Eq.(2.38) in combination with Eqs. (2.36) we now have a complete theoretical basis for the transmission through a coupled cavity-emitter system.

2.1.3 Coupled mode theory

The coupling of the incoming resonant mode b_{in} from the waveguide to the disc has so far been assumed ideal, meaning that 100% of the resonant light will be switched from the bus waveguide to the drop waveguide. In reality, this depends on the coupling between the disc and waveguide [44]. This coupling

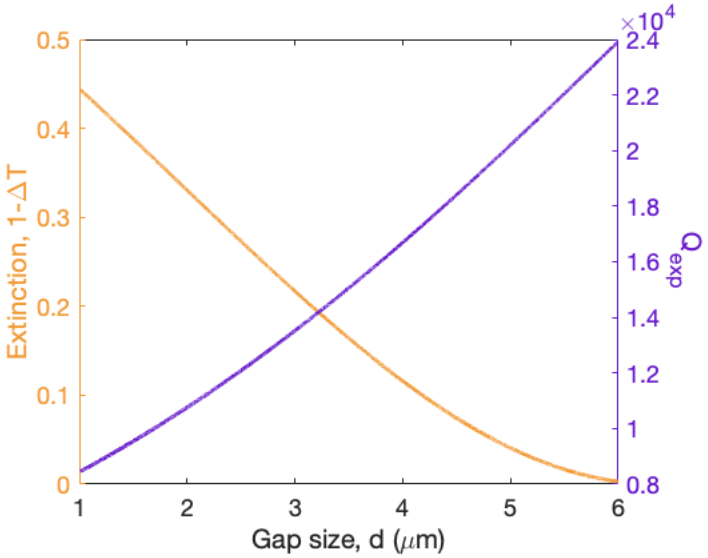

Figure 2.4.: Yellow: Theoretical transmission from Eq. (2.40a). Blue: Expected Q-factor from Eq. (2.40b) depending on gap size between access waveguides and disc resonator.

will be proximity dependent, and according to the formalism presented in [45] the transmission depth ΔT can be expressed as:

$$\Delta T = 1 - \left[T_{cc} + (1 - T_{cc})\left(\frac{1-\kappa_\mathrm{d}}{1+\kappa_\mathrm{d}}\right)^2\right] \tag{2.40a}$$

$$\frac{1}{Q_{exp}} = \frac{1}{Q_\mathrm{int}}(1+\kappa_\mathrm{d}) \tag{2.40b}$$

$$\kappa_\mathrm{d} = \kappa_{\mathrm{d}0}\exp(-\xi d) \tag{2.40c}$$

Here, T_{cc} is the transmission at critical coupling, κ_d is the coupling rate between cavity and access waveguides. Q_int is the intrinsic Q-factor of the disc resonator in absence of the waveguides while Q_{exp} is the experimental Q-factor. Finally, ξ is the characteristic length constant while d is the gap size between disc and access waveguides. By altering the distance of the access waveguides it is possible to vary the coupling of light from waveguide to disc, where a bigger gap results in smaller transmission depth. From Eq. (2.40b) we see that minimising the gap would result in over-coupling, thus lowering the Q-factor. Effects of the gap size on extinction and Q-factor are depicted in Fig. 2.4. Here, we see that as the extinction tends towards 0, the expected Q-factor increases. Ideally, we are interested in large transmission depth and high Q-factors.

2.2 Numerical Simulations

Numerical finite-element simulations are used in order to estimate parameters of importance, such as eigenfrequencies, the Q-factors and the mode volumes for the modes of the disc resonators. All numerical simulations within this work are based on two-dimensional models as depicted in Fig. 2.5.

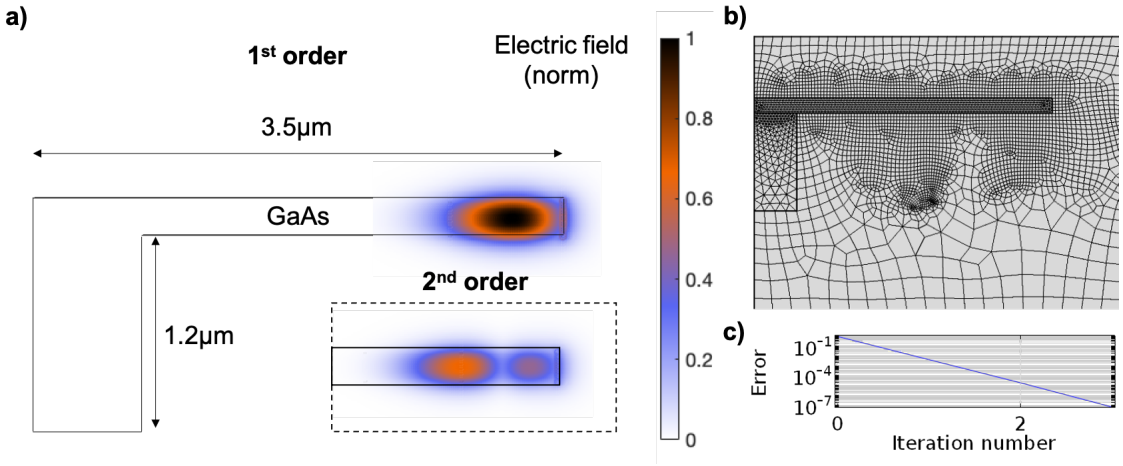

Figure 2.5.: Finite element simulation of microdisc resonator from COMSOL Multiphysics 5.1. a) The fundamental mode (1^{st} order) is found at 323.9 THz at an azimuthal modal order of $m = 65$ and a mode volume of $V_{\text{eff}}^1 = 18(\lambda/n)^3$ while the 2^{nd} order radial mode is found at 326.9 THz at an azimuthal modal order of $m = 60$ and with a mode volume of $V_{\text{eff}}^2 = 22(\lambda/n)^3$. b) Meshing of the two-dimensional model. c) Convergence plot showing only 3 iterations nedded in order to reach error $< 10^{-7}$.

2.2.1 Meshing and convergence

A two-dimensional geometry representing the disc structures discussed in this thesis was defined and meshed in COMSOL Multiphysics 5.1. Using the *Electromagnetic Waves, Frequency Domain* along with rotational symmetry, eigenfrequencies in the disc in the $910 - 940$ nm range were simulated to first and higher order modes of the structure, which can be seen as a cross section of the disc in Fig. 2.5. In order to obtain a sufficiently small convergence error in the simulations, the geometry was meshed to a maximum element size of 36 nm (corresponding to $\frac{1}{5}$ of the height of the disc), while the pedestal and the surrounding air was meshed to a maximum element size of 230 nm (corresponding to $\frac{1}{4}$ of the central wavelength within the simulation). Finally, a perfectly matched layer (PML) enclosing the geometry and air was added as the outer boundary of the simulated setup. A refractive index of $n_{\text{GaAs}} = 3.46$ is attributed the disc while the pedestal, air and PML geometries were treated as air ($n_{\text{air}} \approx 1$). In reality, the pedestal consists of *AlGaAs* which has a higher refractive index than air. Since the disc modes are highly spatially separated from the pedestal this can be neglected. This procedure results in a convergence error $< 10^{-7}$.

2.2.2 Modes and losses

From Fig. 2.5 we see that the the modes propagate along the perimeter of the disc and expand radially inwards on the disc for higher orders. The fundamental mode is found at 323.9 THz (with azimuthal order $m = 65$) while the second order mode is found at 326.9 THz (with azimuthal order $m = 60$). Assuming a lossless structure, theoretical Q-factors are calculated to be in the order of $Q_{\text{theory}} = 10^{13}$, only limited by the computational accuracy. A figure of merit for these devices is the intrinsic Q-factor which is limited by the total loss of optical mode. By applying an imaginary part of the refractive index of *GaAs*, losses can be simulated, thus lowering the calculated Q-factor of the disc.

In practise, these losses can be encountered as absorption into the disc material. Additionally, the curvature of a micro resonator can lead to bending losses which according to Ref. [46] become significant at radii smaller than 2 μm. For greater radii, a primary cause of loss can be surface roughness on the disc, usually amounting to a nanoscale surface variation [21], [23], [24], [47] resulting in scattering loss in the order of $\approx 10 - 100$ dB/cm [46]. The material roughness can occur on the vertical surface of the material but can also appear on the lateral edges of the disc as a result of chemical and mechanical etching, as described in Sec. 3.2. From Scanning Electron Microscopy (SEM) images of the fabricated discs (see Chp. 3) it is *not* possible to see any surface variation, meaning that a present surface roughness must be smaller than $\frac{1}{10}$ of the smallest visible features on the images, the smallest feature being the gap at around $d = 50$ nm. The surface variation must thus be smaller than or in the order of ≈ 5 nm, which is in accordance with what has previously been reported for $GaAs$ [24]. The effective wavelength within the disc resonators amounts to $\lambda_{\text{eff}} = \frac{\lambda}{n}$, where n is the refractive index of the disc material. For near-infrared light, it is clear that the effective wavelength is much larger than the surface roughness, which ultimately leads to high expected Q-factors.

2.2.3 Mode volume of whispering gallery modes

The mode volume is found following the approach presented in [48] but adapted for a linear dipole. From the COMSOL simulations it is possible to calculate the full 3D mode volume:

$$V = \frac{\int \left[\mathbf{E} \cdot \frac{\partial(\omega\epsilon)}{\partial\omega}\mathbf{E} - \mathbf{H} \cdot \frac{\partial(\omega\mu)}{\partial\omega}\mathbf{H}\right] d^3\mathbf{r}}{2\varepsilon_0 n^2 \left[\mathbf{E}(\mathbf{r_0}) \cdot \mathbf{u}\right]^2}, \tag{2.41}$$

where E is the electric field while H is the magnetic field of the mode. The factor n is the refractive index of the disc material. The permittivity of the structure is defined af $\epsilon = \varepsilon_0\epsilon_r$ and the permeability of the structure is defined as $\mu = \mu_0\mu_r$. The relative permittivity and permeability (ϵ_r and μ_r) are assumed to be 1 everywhere in the structure. Furthermore we assume no dispersion with our $GaAs$-structures such that:

$$\frac{\partial(\omega\epsilon)}{\partial\omega} \approx \epsilon \tag{2.42a}$$

$$\frac{\partial(\omega\mu)}{\partial\omega} \approx \mu \tag{2.42b}$$

The modes found within the COMSOL simulations of the disc resonators have three spatial components each and can be written as $\mathbf{E} = (E_r, E_\phi, E_z)$ and $\mathbf{H} = (H_r, H_\phi, H_z)$. Using the knowledge of how the counter propagating modes are related [48] we can write:

$$\left[\mathbf{E} \cdot \frac{\partial(\omega\epsilon)}{\partial\omega}\mathbf{E} - \mathbf{H} \cdot \frac{\partial(\omega\mu)}{\partial\omega}\right] d^3\mathbf{r} = \pi \int\int r dr dz \left[\epsilon(-E_r^2 - E_z^2 + E_\phi^2) - \mu(H_r^2 + H_z^2 - H_\phi^2)\right] \tag{2.43}$$

Furthermore, by taking the mode volume when the dipole is placed in the field maximum, we obtain a minimum mode volume for a lossy structure in cylindrical coordinates:

$$V = \frac{\pi \int\int dr dz \cdot r \cdot [\epsilon(-E_r^2 - E_z^2 + E_\phi^2) - \mu(H_r^2 + H_z^2 - H_\phi^2)]}{2\epsilon_0 n^2 [(\max(E_r)]^2}, \tag{2.44}$$

For a disc resonator with a radius of $r = 3.5\ \mu$m we obtain a minimal effective mode volume of $V_{\text{eff}}^1 \approx 18(\lambda/n)^3$ for the fundamental mode and a mode volume of $V_{\text{eff}}^2 \approx 22(\lambda/n)^3$ for the second order mode. The mode volumes calculated here both assume that the emitter is placed at the field maximum. In the case that it is not, the emitter would experience a higher effective mode volume [49].

In conclusion, from numerical finite-element simulations we are able to estimate the mode confinement within the suspended disc resonators, and we distinguish between fundamental and higher order radial modes. Theoretical Q-factors of the modes are calculated to be in the order of $> 10^{13}$. The expected Q-factor is, however, smaller as sources of loss such as absorption, bending losses and surface roughness are anticipated. The fundamental mode is calculated to have a mode volume of $V_{\text{eff}}^1 = 18(\lambda/n)^3$ while the 2^{nd} order radial mode is calculated to have a mode volume of $V_{\text{eff}}^1 = 22(\lambda/n)^3$, when the linear dipole is located in the field maximum. The location of the single-photon emitter within the resonator affects the effective mode volume.

2.3 Quantum dots as single photon emitters

III-V semiconductors are known to be a remarkable platform for quantum circuits as they allow for planar circuit technology. Well-known techniques and recipes have proven to be highly successful in the implementation of efficient and reproducible nanoscale quantum devices, such as on-chip photon detectors [50] and single-photon filters [51]. Throughout this work we use undoped $GaAs$ wafers with and without embedded $InAs$ QDs as depicted in Fig. 2.6. The wafers are grown by R. Schott at the Bochum University, and their methods for the wafer growth can be found in [52].

We assume a QD to be a TLS with ground state $|g\rangle$ and excited state $|e\rangle$. The crystalline structure of $GaAS$ will create a periodic potential given by the Bloch wave functions [53]:

$$\psi_{\mathbf{k}}(\mathbf{r}) = u_{\mathbf{k}}(\mathbf{r})e^{-i\mathbf{k}\cdot\mathbf{r}} \tag{2.45}$$

Here, $\mathbf{k}$ is the wave vector while $\mathbf{r}$ is the position parameter. The heterostructure of $GaAs$-$InAs$-$GaAs$ can within solid-state physics be represented by the evelope function formalism and treated as a slowly-varying perturbation of the lattice potential. Subsequently, the electron wave function is approximated by a Bloch-function such that $\psi_n(\mathbf{r}) \approx F_n(\mathbf{r})u_{n0}(\mathbf{r})$, where n here denoted the band index, being $n = c, v$ for conduction and valence band, respectively, and $F_n(\mathbf{r})$ is a slowly varying envelope function. From this, band structures of a QD can be calculated. The light and heave hole (hh) band will differ in their effective masses, thus creating different curvatures in the bands. Looking at selection rules and likelihood of transitions [34], the relevant transitions within a QD can be written as:

$$\Psi_e(\mathbf{r}) = \langle \mathbf{r}|e\rangle = F_e u_{e0}(\mathbf{r}) \tag{2.46a}$$

$$\Psi_g(\mathbf{r}) = \langle r|g\rangle = F_{hh}(\mathbf{r})u_{hh0}(\mathbf{r}) \tag{2.46b}$$

The use of quantum dots as single photon emitters has proven to be compatible with on-chip integration of quantum circuits, as demonstrated in [13], [54]. The indium arsenide ($InAs$) QDs used within the

Quantum Photonics group have been shown to emit single photons at high purity while also maintaining a high indistinguishability [13].

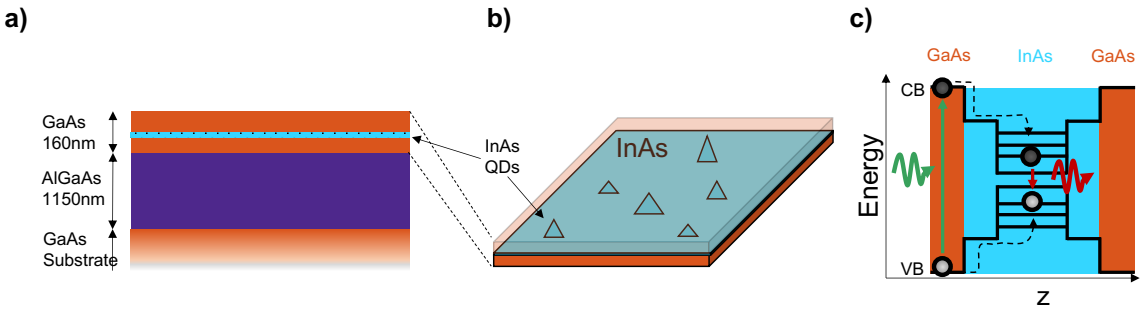

Figure 2.6.: Working principle of GaAs embedded InAs quantum dots as single photon sources. a) GaAs wafer with embedded InAs QDs and a sacrificial layer of AlGaAs. b) Zoom in of QD embedded area of top GaAs layer. QDs are randomly grown as an effect of strain thus acquiring various size. c) Schematic energy band diagram of QD. A hole in the valence band (VB) is excited to the conduction band (CB) using a laser emitting at $\approx 820nm$. The electron is consequently trapped in the QD potential well. Finally, the electron-hole pair recombines and emits a higher wavelength single photon.

The QDs used here are fabricated using epixtaxial growth where a semiconductor heterostructure consisting of $GaAs$-$InAs$-$GaAs$ is grown layer by layer. The schematics of the wafers used in this work is depiced in Fig. 2.6a. The wafer consists primarily of a $GaAs$ substrate with a 1150 nm thick sacrificial layer of $AlGaAs$ which can be etched away in order to suspend structures designed in the top $GaAs$ layer. Within the top layer of the $GaAs$ a thin layer of $InAs$ is grown using molecular-beam epitaxy. Within the $InAs$ layer the QDs self-assemble as small pyramids of $InAs$ islands due to strain induced by the lattice discrepancy between $GaAs$ and $InAs$. The length scales of the QDs range from 10 nm to 70 nm, effectively creating a zero-dimensional system with discrete energy, thereby being a TLS at low temperatures [34]. The self-assembly is a random process, resulting in varying size and placement of the QDs throughout the wafer, as is depicted in Fig. 2.6b. As discussed in the previous section, the location of the single-photon emitter in relation to the cavity mode determines the effective mode volume. The random distribution of the QDs within the wafer can therefore prove a challenge for this project. However, having a high density of QDs improves the probability of finding a well located and resonant QD within a resonator. The size of the QD effectively determines the resonance energy of the TLS within the QD. A schematic of the band diagram that describes the QD is depicted in Fig. 2.6c.

Precise spectral tuning of the QD is required in order to match the cavity resonance to that of the QD. Various schemes can be applied to spectrally tune QDs [55]. Examples such as electrical tuning [13], [43] and strain tuning [56] have proven effective. However, within this work we are constrained to apply temperature tuning [42], [57], as we opted for non-electrically-gated structures. The QD behaves as a TLS at cryogenic temperatures at a temperature range from $< 4\ \mathrm{K} - 60\ \mathrm{K}$ [34]. The exciton energy will red-shift when temperature increases within the working range [34]. The QDs used within this work on average emit light at ≈ 320 THz.

In conclusion, the $InAs$ QDs used throughout this work are randomly grown on a $GaAs$ substrate, resulting in an indeterminate location and bandgap of the single-photon emitter. The QDs have, however, shown single-photon emission of high indistinguishability and purity at cryogenic temperatures.

3 Fabrication of whispering gallery mode cavities

In this chapter we will outline standard fabrication methods used when fabricating planar fully-suspended nanoscale structures in $GaAs$, an example being the disc resonators principle to this study. The manufacturing of these nanoscale devices has been extensively studied and refined within recent years [51], [58], [59], while novel methods and protocols are still being investigated and have yet to be optimised. A bottleneck of the fabrication of suspended integrated circuits is the wire-intersections on-chip. This chapter will furthermore include an optimisation of the development of epoxy cladding to serve as bridges for metal wire intersections within an integrated circuit.

3.1 Electron beam lithography

The design of micro- and nanoscale devices requires extremely high-precision fabrication tools. Details at the nanometer scale can be obtained using Electron Beam Lithography (EBL). The working principle of EBL is to pattern an organic photo resist coated on a substrate. The energy of the E-beam will alter the solubility of the polymer chains in the photo resist, allowing for a removal of the positive-tone resist in the exposed areas. This creates holes in the resist resembling the designed patterns.

The EBL-system uses a beam of electrons manipulated via an aperture, a magnetic condenser lens and a set of electromagnetic deflectors that control the target of the beam on the chip. The current of the beam is adjustable and the exposure dose is usually in the order of $(10 - 100)\ \mu\mathrm{C/cm}^2$.

3.1.1 Proximity effects

Effects involving interactions between the electron beam, the resist and the substrate during EBL can lead to a broadening of the developed pattern, as some unexposed resist receives a non-zero dose. These effects are called proximity effects and primarily consist of two major effects: forward scattering and back scattering [60], which are both depicted in Fig. 3.1.

Forward scattering occurs as the electron beam widens as is propagates through the resist due to electron-electron interactions, thus exposing a broader pattern than initially designed. Choice of material and thickness is therefore non-trivial within EBL. The majority of electrons will pass through the resist and interact with the substrate. Here, electrons can be scattered back and cause further exposure of non-patterned areas of resist. Proximity effects can be taken into account and corrected for using specialised proximity effect software. Throughout this work EBL designs have been corrected

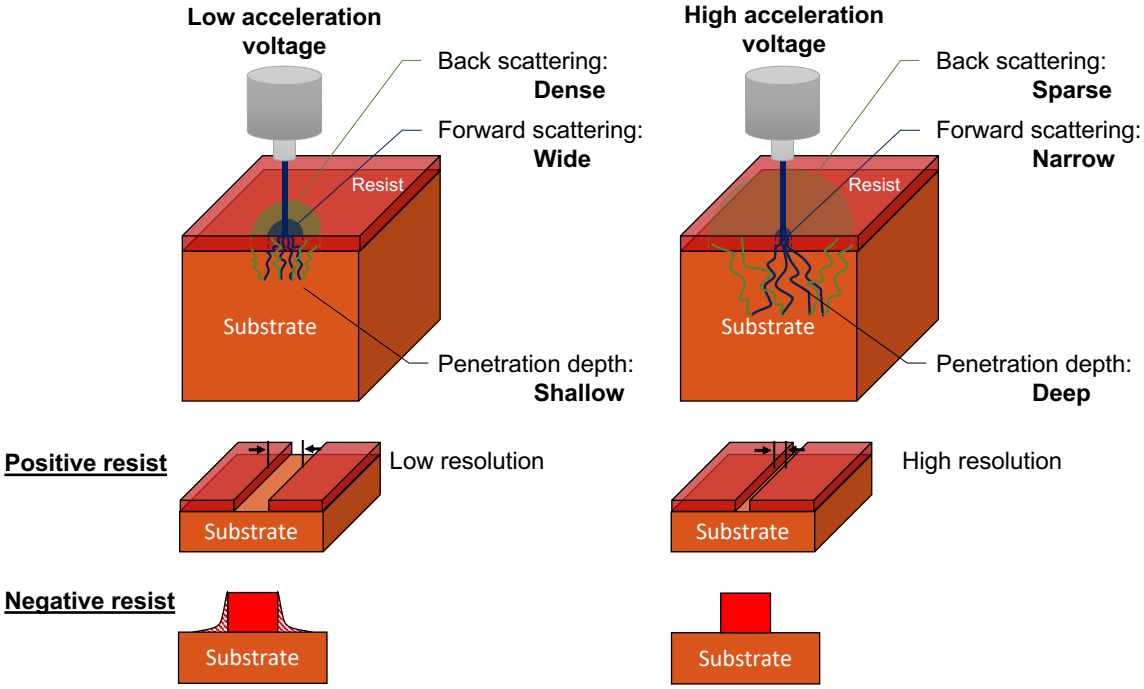

Figure 3.1.: Working principle of Electron Beam Lithography. The electron beam (blue) is exposed to an area of the resist. Depending on the settings of the E-beam acceleration voltage, an additional area outside the E-beam is effectively exposed, due to back scattering (green) and due to the beam dispersing within the resist, called forward scattering. Acceleration voltage controls resolution of the pattern for positive resist, while it determines the amount of excess exposure in negative resist.

using BeamFox Proximity, which fractures the desired patterns into polygons and corrects the dose and dwell time of the E-beam.

3.2 Nanoscale quantum devices

The quantum devices fabricated within this work have length scales in the order of $\approx 10\ \mu$m, while certain features of the devices will be in the order of nanometers. The thickness of the devices is 160 nm, effectively confining the coupled light to two dimensions. Wafers are prepared as 5 mm $\times$ 5 mm or 10 mm $\times$ 10 mm chips allowing several hundreds of devices on one chip. The design of the device and the entire chip is called a *mask*.

Routine fabrication steps are outlined in Fig. 3.2. Positive-tone photo resist, in our case either CSAR or ZEP520, is used when patterns outlining or partaking in the design are to be fabricated as seen in Fig. 3.2a. During the EBL-process the pattern will be exposed to a current, dose and dwell time of the E-beam. During exposure the molecules in the positive photo resist will undergo altercations. After exposure, a development of the pattern, typically in n-Amylacetate, will remove the exposed parts of the resist, as depicted in Fig. 3.2b-c. After development, several processes are available. Metalisation will usually be the first element fabricated on a chip, as gold cross markers enable high-precision alignment for later E-beam exposures. During metalisation metals are evaporated from a crucible onto the chip

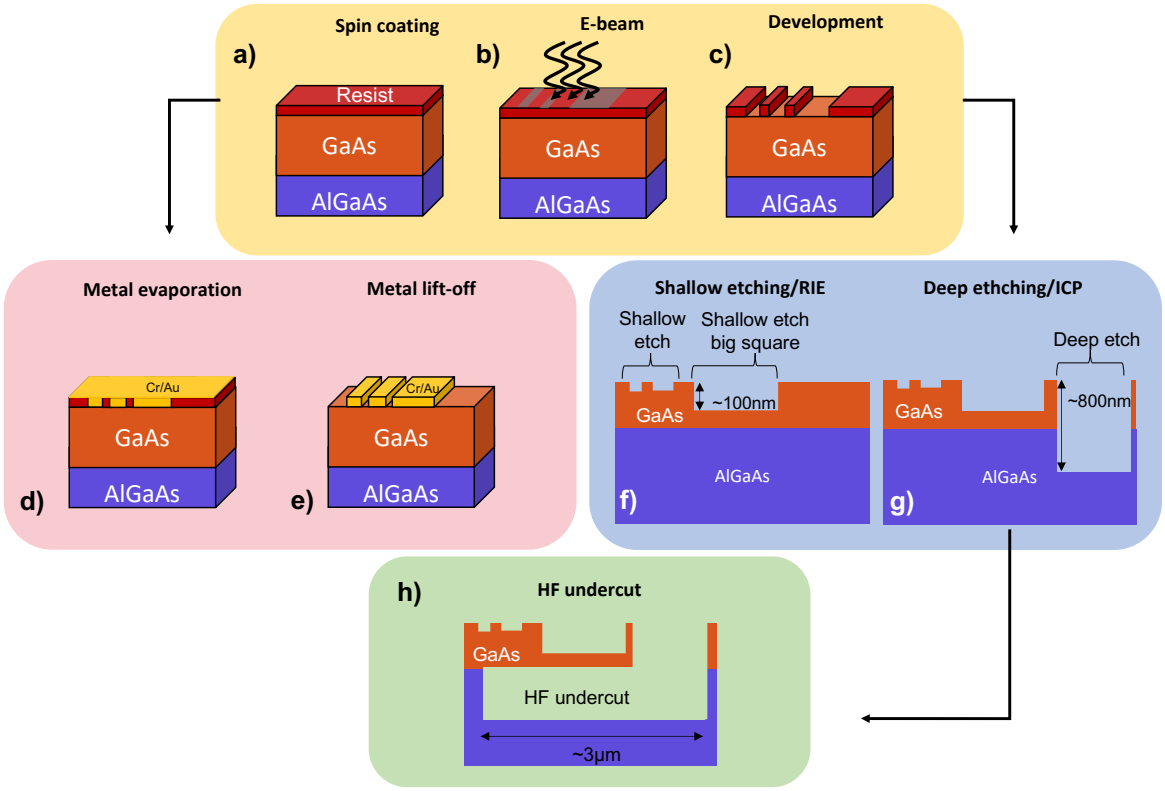

Figure 3.2.: Fabrication of nanoscale *GaAs* devices. a) Spin-coating of positive resist to a final thickness of ≈ 550 nm. b) E-beam exposure of pattern design. c) Development of exposed pattern in n-amylacetate. After development different processes can be performed (following either top black arrow). d)-e) Metal evaporation and resist lift of. f) Shallow etching in GaAs using Reactive Ion Etching (RIE). g) Deep trenches etched using Inductively Coupled Plasma (ICP) RIE. These trenches reach the AlGaAs layer which reacts with hydroflouric acid and allows for an underetching as seen in h), resulting in suspended *GaAs* structures.

with nanometer precision in thickness. By lifting off the remainder of the resist and the excess metal, the chip will have a finished layer of metal patterns as depicted in Fig. 3.2d-e.

By repeating the initial steps indicated by Fig. 3.2a-c, additional layers such as shallow etching and deep etching can be fabricated, as depicted in Fig. 3.2f-g. Shallow patterns are ecthed using Reactive Ion Etching (RIE), which is a dry etching using chemically reactive plasma to mechanically remove the parts of the wafer that are not covered by resist. The depth of the shallow etching is manually controlled by measuring photoreflectometric data using an end-point detector. Using a reflectance simulation, we aim for a large pattern etch depth of ≈ 100 nm which will result in an etch depth of ≈ 50 nm for small patterns. The shallow etching is used for fabricating shallow etch gratings (SEG), depicted in Fig. 3.3c, with which we are able to in- and out-couple light from the planar devices. Further material about the SEGs can be found in [58].

Deep etching patterns are fabricated using Inductively Coupled Plasma (ICP) RIE. The ICP-RIE process is rapid and produces trenches at a depth of around ≈ 800 nm. The depth of the ICP-RIE process reaches the *AlGaAs* sacrificial layer. Consequently, by immersing the chip in hydroflouric acid (HF), the acid will react with the *AlGaAs* layer and dissolve an amount of the sacrificial layer according

to the time the chip is immersed. For a 50 s immersion the undercut will have a size of approximately 3 μm as depicted in Fig. 3.2g. The undercut is a key element in the fabrication of integrated nanoscale devices, as it allows for partially and also fully suspended structures. The suspension of, for example, a disc resonator is paramount, as the guided mode will not experience losses due to a substrate. This enables high Q-factors of the devices.

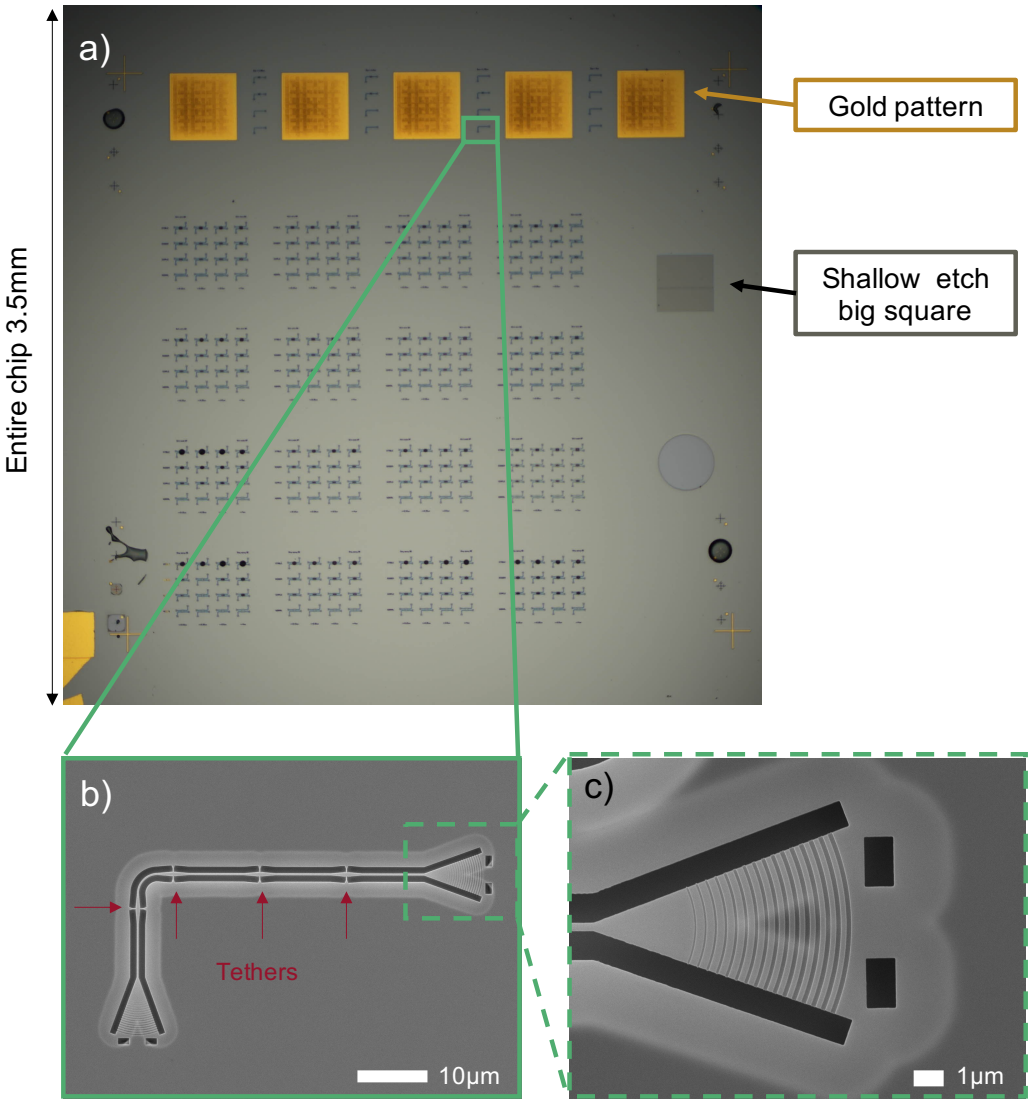

Figure 3.3.: Images after completed fabrication of chip. a) Microscope image of full chip. Yellow patterns are gold. b) SEM image of a nanobeam waveguide with two grating couplers. c) Zoom in on grating coupler. Dark grey pattern is deep etch while the fringes making up the coupler are shallow etched. The undercut is visible as a lightening of the material surrounding the deep trenches.

A standard undoped chip will be fabricated using three E-beam exposures (for metal deposition, shallow etch and deep etch) followed by an HF undercut. The full recipe used within this work can be found in Appendix B. An example of a finished chip is depicted in the microscope image in Fig. 3.3a. The full mask of the chip contains suspended micro disc resonators and simple nanobeam waveguides as depicted using Scanning Electron Microscopy (SEM) imaging in Fig. 3.3b. Here, we see four tethers connecting the device to the remainder of the wafer as to uphold the structure. Tethers should be placed approximately every 10μm to avoid the collapse of waveguides. Zooming in on the grating

coupler in Fig. 3.3c we see the deep etch trenches as the dark grey pattern, while the shallow etch makes up the fringes in the centre of the deep trenches. The undercut is visible as a lightening of the grey material surrounding the deep trenches.

3.3 Metal wires across epoxy cladded nanoscale devices

The on-chip fabrication of planar fully-suspended *GaAs* nanophotonic devices is paving the way for photonic integrated quantum information processing. By using doped p-i-n wafers and adding electrical contacts to the devices, it is possible to highly reduce charge noise within the quantum systems. Furthermore, this allows for a resonance tuning of the exciton state of the QD [34]. Many quantum devices, such as single photon sources [13] and filters [51], are therefore gated via metal wires on the chip. Electrically contacting multiple devices on-chip in a scalable fashion is a non-trivial process that puts restraints on chip design when avoiding short circuits. This adds additional design and fabricational steps in order to electrically isolate groups of devices. With these electrically separated groups of devices follows both limitations of the design as well as a non-zero amount of parasitic capacitance through the p-i-n junction [61]. In order to achieve a substantial scalability of on-chip devices within a quantum circuit it would be advantageous to be able to realise cross-device wiring and wire intersections [15] as depicted in Fig. 3.4.

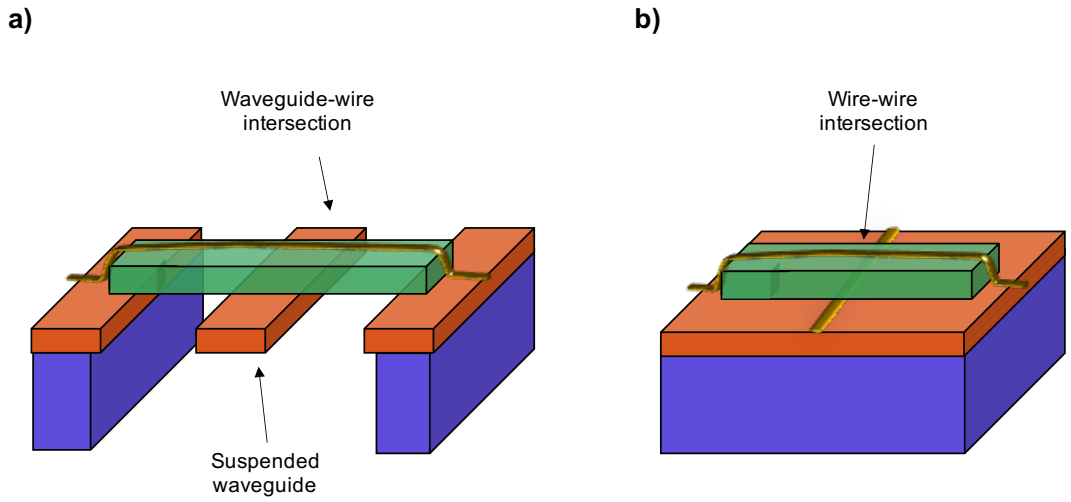

Figure 3.4.: Conceptual metal bridges. a) Metal wire (gold) on epoxy cladding (green) crossing a suspended waveguide (orange). b) Metal wire on epoxy cladding crossing metal wire.

The QDs embedded in the microdiscs within this thesis are being tuned via temperature control, as briefly discussed in Sec. 2.3. In order to electrically tune the band structure of the QDs in discs, we would need to be able to lead a metal wire onto individual discs, in order to electrically gate the p-i-n structure. Crossing metal wires onto individual structures imposes two challenges, one being crossing metal over trenches. Another challenge occurs as metal wires have high absorption and will affect the optical mode if the proximity is not sufficiently large to minimise absorption losses. By using epoxy claddings across both device as well as trenches, as depicted in Fig. 3.5a, we introduce a solution to gating individual nanoscale devices.

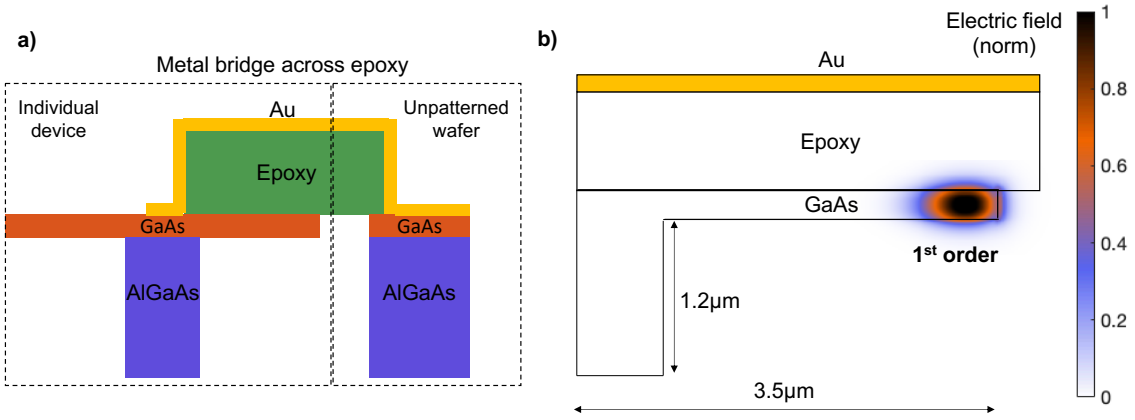

Figure 3.5.: Epoxy cladded disc resonators. a) Cross section schematic of the conceptual epoxy claddings across trenches and devices along with the metal bridge. b) Simulation of optical mode in disc resonators with $1\mu m$ epoxy cladding with a refractive index of 1.58 along with $100nm$ gold on top. The mode is normalised to the same value as the mode depicted in Fig. 2.5.

3.3.1 Optimising fabricational procedure

Within this work we have investigated the possibility of fabricating bridges of polymer epoxy on top of disc resonators over which metal wires can be deposited. The epoxy polymer is optically transparent[1] and has a low refractive index of ≈ 1.45 [62], meaning that an electromagnetic mode encountering epoxy cladding should theoretically not obtain a significant amount of loss. The thickness of the epoxy (≈ 1.15 μm) would ensure that an insignificant amount of the electromagnetic waves propagating within the quantum devices is absorbed into the metallic wires, while the refractive index difference between $GaAs$ and that of the epoxy would still be sufficient in order to confine the light to the $GaAs$. By doing a finite element simulation in COMSOL on the disc resonator, now including an epoxy cladding and a Au-wire on top, as is depicted in Fig. 3.5b, we can simulate the propagating mode within the resonator. Here, the mode is normalised to the same factor as the mode in Fig. 2.5, where no metal or epoxy is present. The magnitude of the mode is insignificantly affected by the epoxy cladding and the metal wire. Fabricating the epoxy-metal bridges on top of nanoscale devices would require the fabrication steps as explained in the previous section, and the additional steps to include the epoxy bridges and the crossing metal wires, which is depicted in Fig. 3.6. In the green box we see that the devices themselves are fabricated using essentially the same procedure as described in the previous section, except that deep trenches are here etched with RIE to a target depth of ≈ 200 nm. This change is due to the uncertainty about how these trenches will affect the epoxy when spun on top and thus to avoid large irregularities on the epoxy surface. The checkered pattern in Fig. 3.6e indicates this uncertainty.

The proximity effects of using negative resist are depicted in Fig. 3.1. Here we see that the scattering effects result in extra *wings* of resist. Furthermore, using the negative tone resist EpoCore2 to make the epoxy claddings will add extra fabricational steps. After spin coating the resist onto the chip, a pre-baking on a hotplate is necessary in order to remove the solvent of the EpoCore2 solution in preparation for the E-beam. Furthermore, immediately after E-beam exposure a post-baking on a hotplate is necessary in order to cross-link the resist and the substrate. Finally, following the development of the

[1] According to the manufactor: https://www.microresist.de/en/produkt/epocore-epoclad-series/

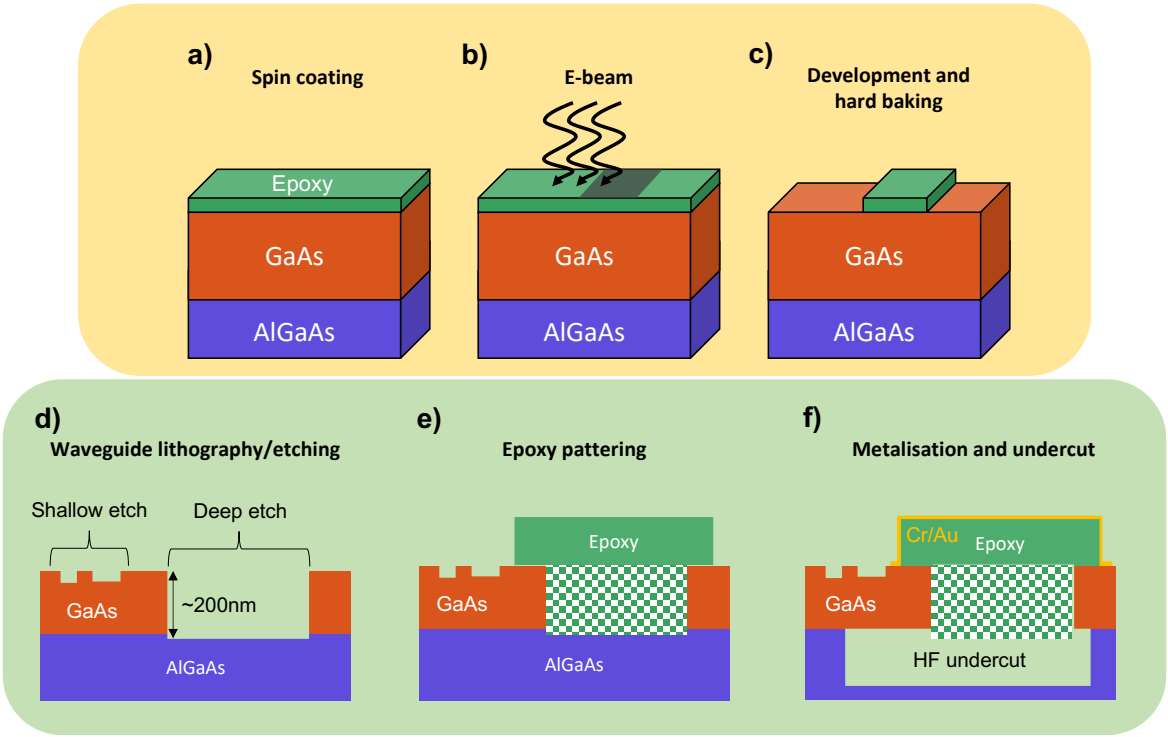

Figure 3.6.: Main processes of fabrication of devices with epoxy cladding. a)-c): Epoxy structures on plain wafer. a) Negative photo resist of polymer epoxy is spin coated to a thickness of $\approx 1.15\mu m$. b) Electron beam lithography patterning. c) The unexposed negative photo resist is removed during development such that only the exposed pattern remains. d)-f): Epoxy structure on top of fabricated devices. d) Nanoscale devices are fabricated following essentially the same steps as depicted in Fig. 3.2 except the deep etch which is in this case also made with RIE to a target depth around 200nm. e) Epoxy structures are patterned across the devices. f) The chip with the epoxy structures is spin coated and $100nm$ Cr/Au metal patterns are written and evaporated onto the chip and finally underetched.

epoxy claddings, a hard-baking process takes place in order to permanently adhere the structures to the substrate. Baking details are summarised in Tab. 3.1.

3.3.2 Determining thickness of crossing metal wires

In order to successfully cross a metal wire over an epoxy bridge we need to spin coat a sufficiently thick layer of resist across the epoxy structures. It was undetermined how the distribution of resist around the 1.15 μm tall epoxy structures edges would develop. The thickness of the resist is especially crucial at this step, since the developed resist trenches will be the form that shapes the metal deposition. Normally, using either ZEP520 or CSAR photo resist on a flat substrate surface we obtain a thickness of $\approx$ 550 nm after which we deposit 10 nm Cr and 170 nm Au.

As a first, we designed a chip with strips of epoxy as depicted in Fig. 3.7a. After fabricating only the strips of epoxy and spin coating them with resist, we cleaved the chip in two along the path of the metal pattern in order to investigate the spread of the resist across the claddings through SEM imaging. Since both epoxy and photo resist is organic material, and since high electrical conductivity stabilises

the electron microscopy, the cross section of the chip is sputtered with gold after which we can image the cross section using SEM. A cross section image is depicted in Fig. 3.7b. The epoxy structure has been false coloured green. Here, we notice that the edges of the epoxy structure has lifted off from the substrate. Zooming in on the corner of the epoxy structure, where the layer of resist is expected to be thinnest, we measure a thickness of around 270 nm. This is sufficient for a metal deposition of around 100 nm.

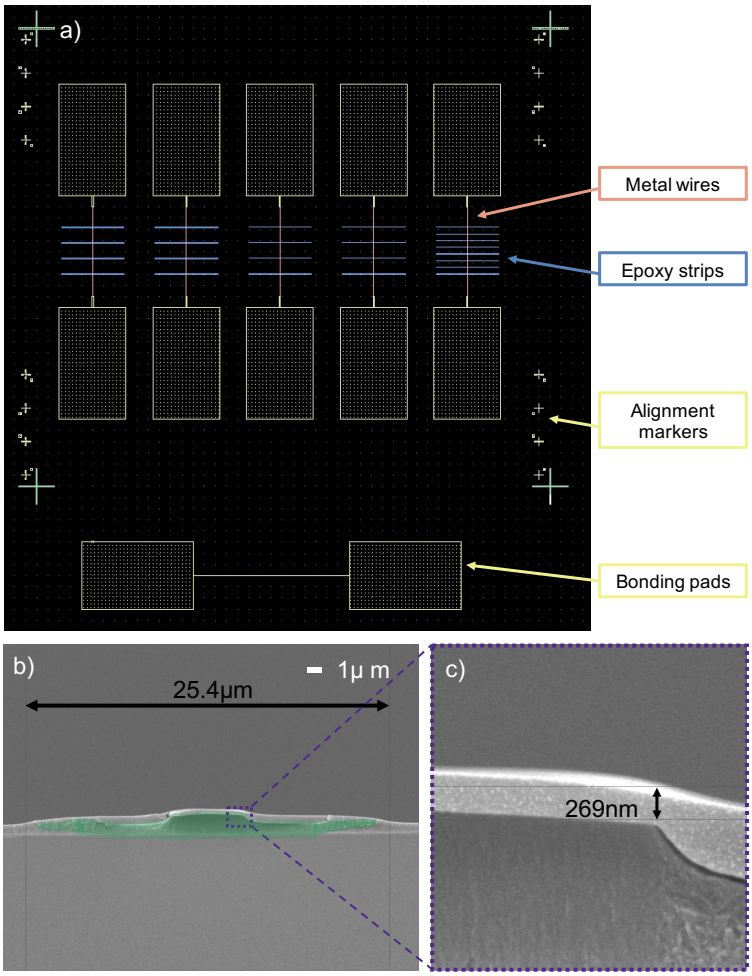

Figure 3.7.: a) Mask design of Epoxy-Bridge chip showing 12 paired up bonding pads (yellow) connected by metal wires of which 5 metal wires are crossing varies amounts and sizes of epoxy strips. b) SEM image of cross section of chip with 5 μm wide patterned epoxy strips (green) and with gold spattered CSAR resist (lightest grey). c) The thinnest area of the resist is at the edge of the epoxy structure and is measured to be $\approx$ 270 nm thick.

3.3.3 Electron beam preparation

Fabricating the entirety of the mask design depicted in Fig. 3.7a successfully would result in 6 pairs of connected bonding pads and the ability to conduct a current through all of them. However, during the initial tests of epoxy cladding, the adhesive substance OmniCoat was used as a bonding layer between the substrate and the epoxy structures. The usage of OmniCoat did, however, not result in an adhesive

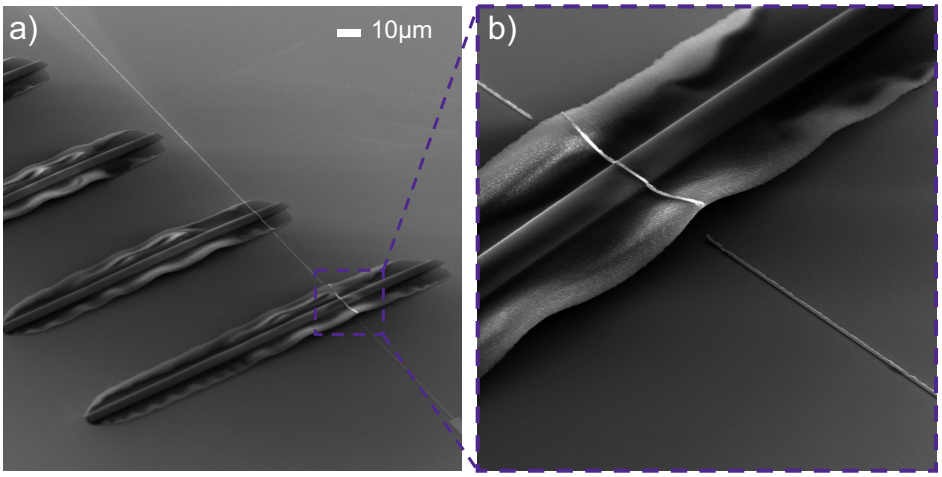

Figure 3.8.: a) SEM images of the finished Epoxy-Bridge chip showing the remainder of the 5 μm wide epoxy strips along with the Cr/Au metal wire. b) Zoom in on the edge of the epoxy strip which is seen to have lifted off the chip thereby disrupting the crossing wire.

promoter, but rather as a lift-off for the epoxy structures, resulting in vanished and floating elements of epoxy as depicted in Fig. 3.8. The reason behind this is likely to be connected to the optimisation of the coating in relation to spin and post-baking. Zooming in on the metal crossing in Fig. 3.8b we see that the metal has been deposited according to the design, but that the lift-off of the epoxy breaks the wire, resulting in no connectivity across the epoxy structures. The coating with OmniCoat has been retracted from the recipe, and the following tests have all been fabricated without it.

Even though early tests did not confirm connectivity through metal wires crossing epoxy structures, important points were to be learned from these tests. The large strips of epoxy that survived from the design in Fig. 3.7a had a nominal width of $w = 5$ μm. The measured width of the final epoxy structures, however, was $w_{\mathrm{SEM}} = 25.4$ μm, as depicted in Fig. 3.7b. This indicates either melting or proximity effects from the E-beam during exposure. The excess of the epoxy structures will be referred to as *wings*. The initial settings of the E-beam are described in Tab. 3.1 and proximity corrected using BeamFox Proximity as described in section 3.1.1.

Fabrication of epoxy claddings		
EBL settings for epoxy exposure		
Current	**Area dose**	**Dwell time**
100 pA	9 μC/cm^2	0.0144 μs
Baking procedure		
Pre-bake	**Post-bake**	**Hard bake**
(50/90)°C for (2/2) min	(50/85)°C for (2/3) min	(90/130)°C for (2/20) min

Table 3.1.: Key factors in fabrication of epoxy claddings. E-beam settings at a low area dose combined with a rigorous baking procedure results in successful fabrication of epoxy claddings.

By designing a mask similar to Fig. 3.7a, though this time including epoxy donuts, a dose test was performed in order to understand at which dosages the epoxy structures were ideally exposed. Using the settings of Tab. 3.1, $D = k \cdot 9$ μC/cm^2, but altering the dose coefficient ranging from $k = 0.5$ to

$k = 1.2$, strips and donuts of epoxy were fabricating as depicted in Fig. 3.9. Here, we primarily see that the wide epoxy strips (nominally 2 μm in width) obtain wings of epoxy, and that a higher dose causes larger wings. Initial speculations concerned the necessity of wings since vertical side walls of epoxy would render it difficult to spin coat a sufficiently thick layer of resist for EBL and would pose challenges for the metal deposition.

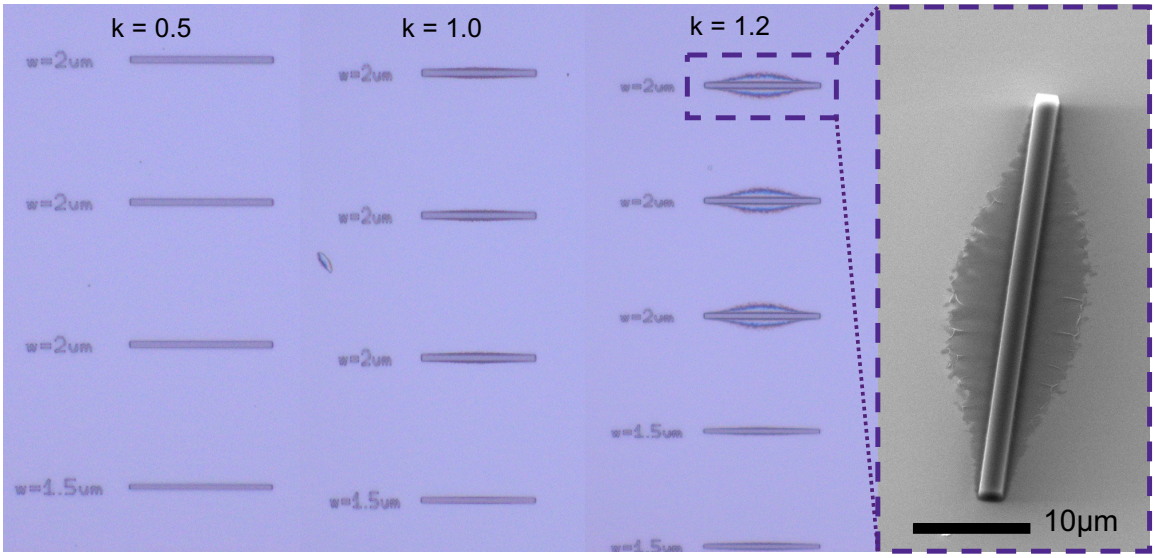

Figure 3.9.: Microscope images of epoxy strips patterned at varying doses, $D = k \cdot 9\ \mu\text{C/cm}^2$, along with a zoom in SEM image of a 2 μm wide epoxy strip at dose coefficient $k = 1.2$. The higher dose, the larger wings the epoxy structures obtain.

Fabrication of all structures was successful at every dose. The amount of wing, however, additionally varies with the shape of the fabricated epoxy structure, as indicated in Fig. 3.10b-c. Here, both structures are fabricated at dose coefficient $k = 1.2$ to a nominal width of $w = 1.5$ μm. The straight epoxy strip obtains a final wing size of ≈ 1 μm to each side, while the wings of the donut are barely visible. The difference in wing size can be due to a difference in fracturing within the BeamFox Proximity software, the difference being depicted in Fig. 3.10a. Here, it is visible that the center part of the straight strip receives much higher dose than any area of the donut. It is expected that the difference in dwell time and thereby wing size can be resolved by a more effective usage of the software, but for the further work within this thesis we have chosen to simply avoid straight strips of epoxy.

From Fig. 3.10b-c we furthermore see that the crossing of the metal wires was indeed successful both with and without large wings of epoxy. The metal is seen to clearly cross both the straight strip and also the donut without any discontinuity. A dose coefficient of $k = 1.0$ was chosen for fabrication of further epoxy bridges. Since wings do not seem to enhance the quality of the metal crossings, it is debatable whether a smaller dose coefficient should have been chosen in order to fully avoid wings. However, since the donut shapes do not seem to be overexposed, the precision of the dose coefficient is not of great importance.

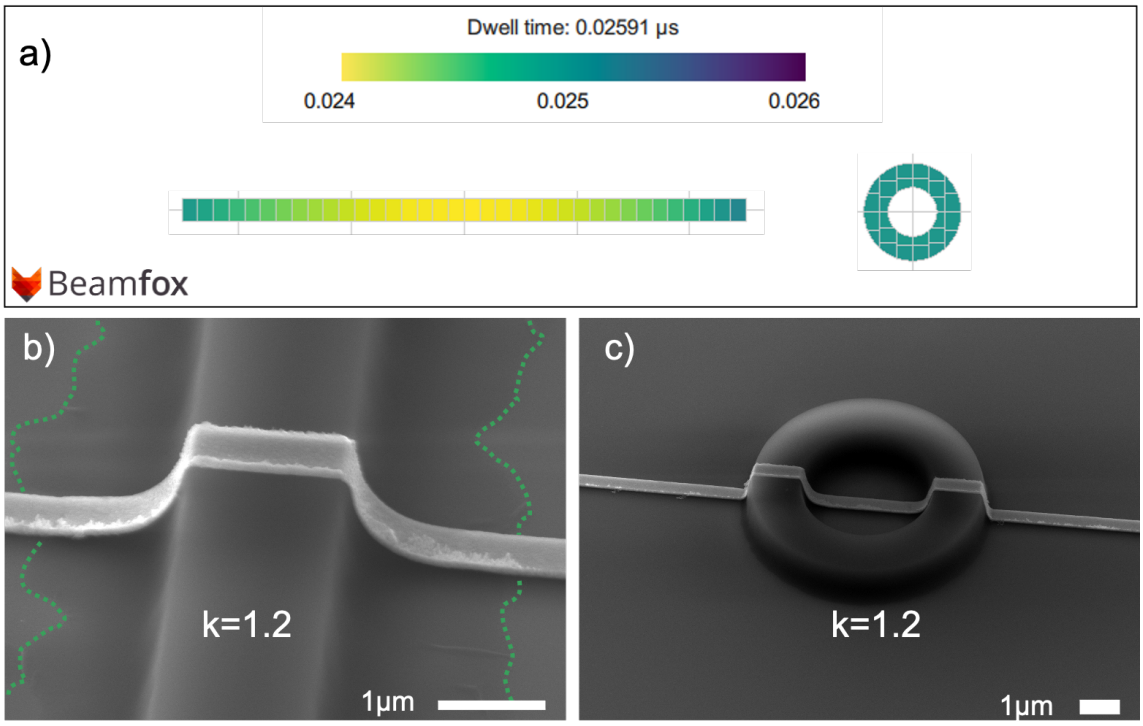

Figure 3.10.: Epoxy structures with nominal width of $w = 1.5$ μm with exposure dose coefficient of $k = 1.2$. a) Fracturing and dose correction via altered dwell time of the E-beam made in BeamFox Proximity for a straight strip and a donut both with width 1.5 μm. In the straight strip in b) the resulting epoxy wing is marked with a green curve while in the donut structure in c) the resulting wings are negligible.

3.3.4 Using Reactive Ion Etching for deep trenches

Having determined a dose coefficient for the EBL exposure of epoxy cladding and having shown reproducible metal crossing across the epoxy bridges, a full chip containing nanoscale devices was fabricated. An example of one of the devices is depicted in Fig. 3.11b, where a disc resonator with four coupler gratings and epoxy cladding on top of the disc is connected to two metal wires crossing the bridges. The epoxy cladding is crossing a deeply etched trench as the bridge is intended to connect the metal wire on the wafer with the metal pads on the disc. As described in Fig. 3.6 the deep trenches are etched before the epoxy is spun onto the chip. It is uncertain how the epoxy is affected by the deep trenches. For standard nanoscale devices, deep trenches are normally fabricated using ICP-RIE ethcing, but since this rapid etching creates ≈ 800 nm deep trenches, RIE etching was used in order to make shallower trenches. The endpoint detection reflectometry used during RIE etching becomes slightly more complicated when punching through the $GaAs$ membrane, as the pattern of reflection alters when the beam reaches the $AlGaAs$ layer as depicted in Fig. 3.11a. The alteration of reflectance allows us to estimate when the RIE has etched down to $AlGaAs$, but it is uncertain how long etch time is needed at this layer in order for smaller patterns to have reached this layer too. As seen in Fig. 3.11a we attempt two different RIE etch times after the assumed $GaAs$ punch-through. From Fig. 3.11b-d we see that an RIE time of $t_{\text{deep1}} = 241$ s was not sufficient to punch through the membrane at small design features. This is visible from a grey gradient where the device should have been fully trenched. Furthermore, fabrication mistakes involving the metal deposition were made for this chip, resulting in disconnected

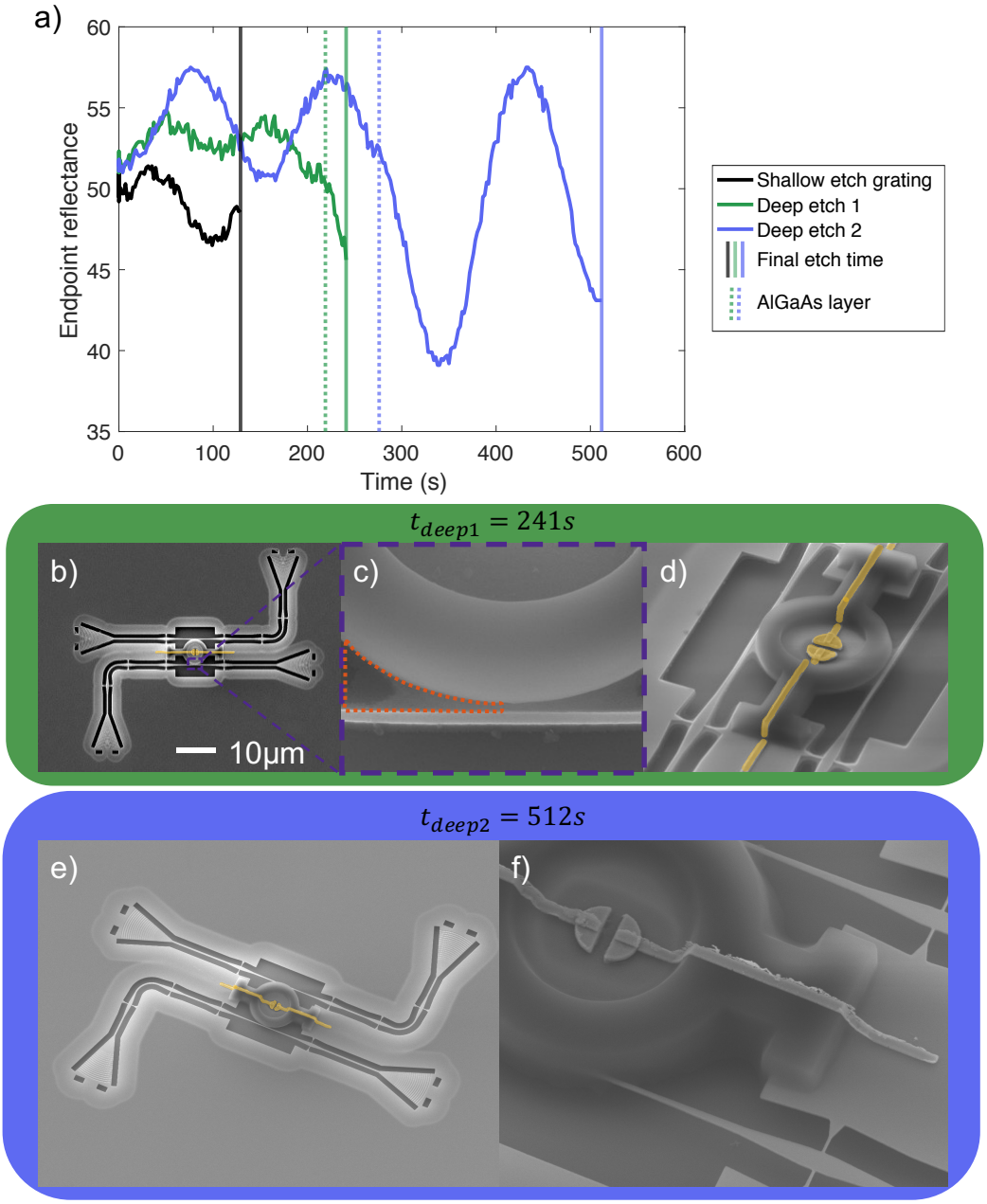

Figure 3.11.: a) Endpoint reflectance measured during Reactive Ion Etching process. Shallow etching for gratings which is here manually stopped after 129 s (black). Continued etching reaches the *AlGaAs* layer indicated by dotted lines where this approximately occurs at $t_{deep1} = 241$ s (green) and $t_{deep2} = 512$ s (blue). b)-f) SEM images of full Epoxy-Disc device. a)-c) Deep etching time of $t_{\mathrm{deep1}} = 241$ s. d)-e) Deep etching time of $t_{\mathrm{deep2}} = 512$ s. a) Disc resonator with epoxy donut, gold (Cr/Au) pads and wires. b) Zoom in on small features of the deep etch. A grey gradient is visible indicating that the *GaAs* is not fully etched away at small features. c) Noncontinuous metal crossings are visible due to fabrication error. d) Continuous metal crossing in an exemplary device. e) Zoom in on small features where no grey gradient is visible, indicating a fully etched *GaAs* membrane.

metal crossings. However, looking at Fig. 3.11d-e we see that $t_{\mathrm{deep2}} = 512$ s is in fact sufficient to create fully punched through deep etches, and that the metal crossing are successfully fabricated too.

It is yet to be determined whether the deep RIE etching leads to a higher loss rate than the rapid RIE-ICP etching, and whether this shallower deep etch is even necessary. It is possible that the surface tension of the epoxy is sufficiently high to not be affected my trenches in the order of micro meters. Both issues can be further investigated by looking at SEM and Atomic Force Microscope (AFM) images of cross sections of epoxy cladded structures.

In conclusion, we find that high dose coefficients create large wings of epoxy, and that continuous metal wires can be fabricated across epoxy claddings of thickness 1.15 μm at low dose coefficients as well as at high dose coefficients. By finding an appropriate E-beam dose coefficient and RIE time for deeper trenches, on-chip suspended nanoscale quantum devices were fabricated with epoxy cladding and connected metal wire depositions.

4 Optical characterisation of disc resonators

Following successful fabrication of the disc resonators, the respective chips are to be optically characterised. Throughout this chapter we will describe the optical setup used for the experiments conducted within this work. We will furthermore be giving an overview of the device specific size parameters and the quality factors of the disc resonators.

4.1 Experimental setup

All optical characterisation of the disc resonators and their embedded QDs was performed using the setup depicted in Fig. 4.1a.

The QDs used throughout this work can be excited using a range of different methods, one of which is called *above band excitation* and is schematically outlined in Fig. 4.1e. By exciting electrons from the valence band to the conduction band outside the potential well using a high-energy laser, holes are created in the valence band. Electrons and holes will ballistically travel within the material and are able to relax into the potential well of the QD. After a period corresponding to the lifetime of the QD, the electron-hole pair will recombine and the QD will emit a single photon with a lower energy than the original excitation energy. Advantages of this excitation scheme include the ability to filter away the high-energy laser light from the out-coupled light using a low-pass filter, such that all emission will come from the QDs. Furthermore, this method provides an efficient way of measuring the frequencies of the QDs within the structure, since the ballistic range of the above-band excitation is in the order of $\approx 10\ \mu$m, thus allowing the emission of a very big area of QDs simultaneously.

The Tsunami laser is a high energy pulsed laser. By tuning the laser to ≈ 820 nm and exciting directly on top of the disc, as depicted in Fig. 4.1c, QDs will be excited above band. QDs resonant with the cavity modes will emit into cavity mode, thus allowing coupling out into the access waveguides, enabling the single photons to be collected at either port. The out-coupled QD emission is sent to a spectrometer and will effectively show the cavity modes. It is also possible to further analyse one single frequency as the out-coupled QD emission can be sent through the grating, in order to spectrally filter the selected frequency, and into a single photon detector for lifetime measurements as depicted in Fig. 4.1a. When encountering a photon, the single-photon detector sends an electrical signal to the PicoHarp, which resolves the photons in the time-domain. The arrival times of the single photons are recorded relative to a synchronisation pulse emitted by the Tsunami laser. The signal-to-noise ratio of a lifetime measurement depends directly on the integration time of the experiment, such that a long integration time yields a higher signal-to-noise ratio.

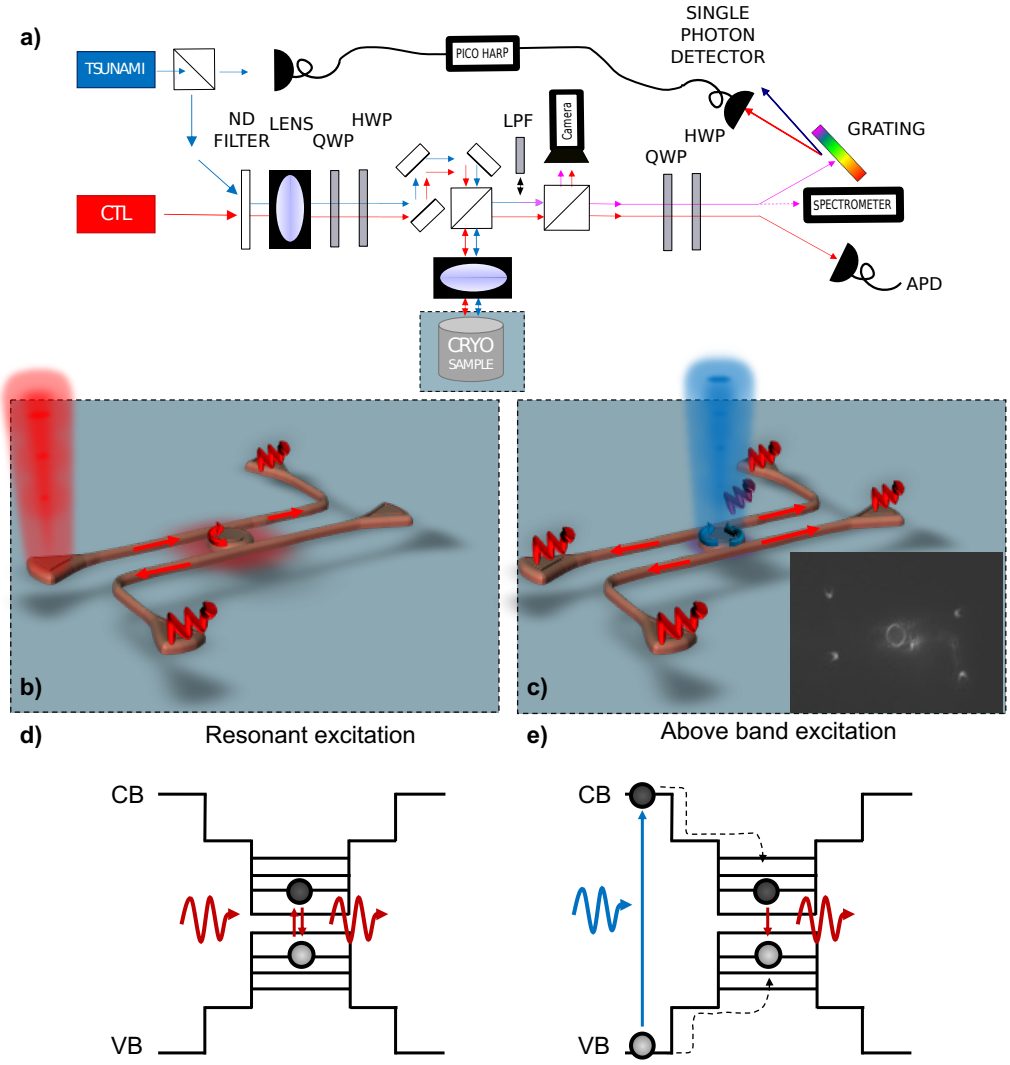

Figure 4.1.: a) Setup of optical experiments. Two lasers are used in these experiments. Tsunami (blue) for above-band pulsed laser excitation and the CTL (red) as a tuneable continous wave (CW) laser. One excitation and collection path is used for both lasers and consists of optical densities (ND filters), polarisation control in the form of $\lambda/4$ and $\lambda/2$-plates (QWP/HWP) and beam splitters. Light is sent from the excitation path into a Montana tabletop cryostat in which the sample is mounted. The incoming beam is seen on (b-c). b) The CTL is coupled into the disc resonator via excitation port and access waveguides. The CTL output is sent to a single photon detector (APD). c) The Tsunami laser is focused onto the disc on which it will generate QD emission. While the output Tsunami laser is filtered out by a low-pass filter (LPF), the QD emission is either sent to the spectrometer, or to the lifetime setup. During lifetime measurements the Tsunami laser is sent through a beam splitter before entering the excitation path. A control pulse is sent to a detector and into a time-correlated single photon counting system (PicpHarp), while the other pulse follows the excitation path into the cryostat. The QD emission is sent through a grating with a narrow bandwidth of $\approx 0.2nm$ and finally into the PicoHarp. The inset of c) shows the camera image of the above band-excited structure after passing through a low-pass filter. Schematics of resonant and above band excitation is shown in d) and e), respectively.

Another method of QD excitation is called *resonant excitation*. Here, an exciton-resonant mode within physical proximity to the QD will excite an electron already sitting in the QD potential well, as schematically outlined in Fig. 4.1d. Resonant excitation is highly interesting as it allows for coherent manipulation of the excitonic state of the QD without creating further carriers or phonons, which is the case when using above band excitation [34]. Resonance fluorescence (RF) can be used to create pure and indistinguishable single photons, and is therefore highly relevant within the area of quantum information experiments.

For RF measurements, we use the Toptica CTL laser which is a tunable continuous wave (CW) laser with very high tuning resolution. The CTL can be locked at a specified wavelength. By coupling the CTL in through the excitation port and collecting at either bus or drop port, as depicted in Fig. 4.1b, the out coupled light can be sent to an Avalanche Photodiode (APD). Here, the counts at each frequency will be measured. By setting up a large frequency scan of high spectral resolution, the cavity response can be measured to high a precision.

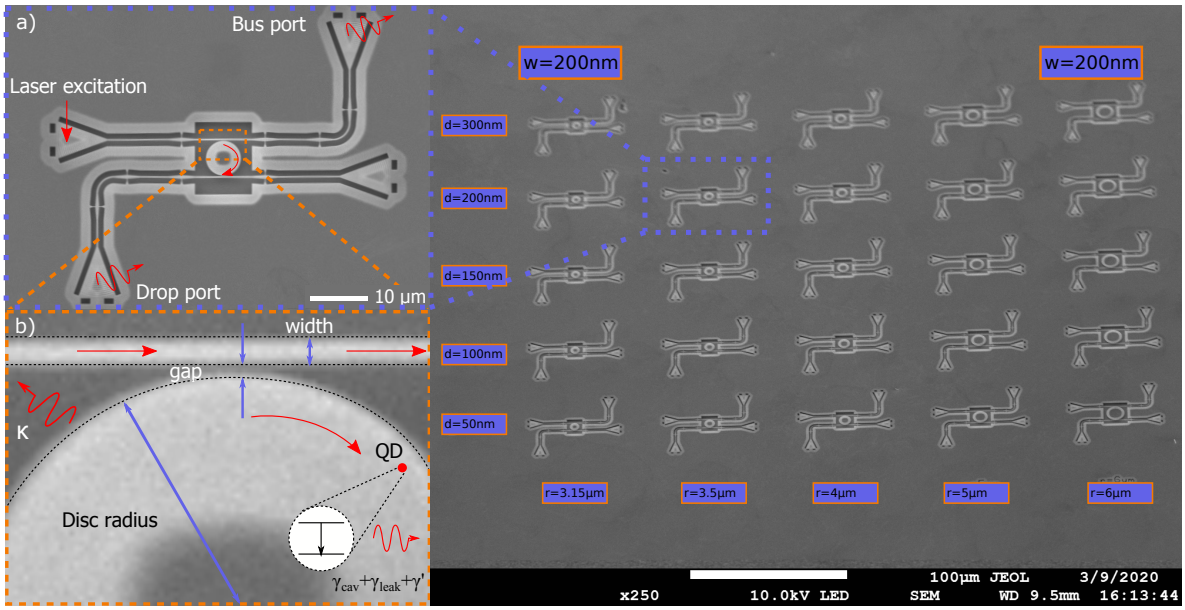

Figure 4.2.: a) Full disc resonator device with indicated excitation, bus and drop port. b) Zoom in on tapered waveguide and disc. In the case of the QD embedded devices, QDs will be present in the disc as schematically shown. c) Parameter space of a chip showing 1 out of 16 quadrants of devices on one 5 mm × 5 mm chip. Here d is gap size and w is waveguide tapering width while r is disc radius.

The disc resonators discussed in this chapter are fabricated using the methods described in Sec. 3.2. An example of a finished fabricated *GaAs* disc resonator is depicted in an SEM image in Fig. 4.2a. Here we see the circular disc along with waveguides just as described in Sec. 2.1.2. The dark grey area in the center of the disc is a pillar of *AlGaAs*. The waveguides are connected to in/out coupling gratings at each end. By choosing one of the coupler gratings as excitation port, we determine what will be referred to as *bus port* and *drop port* as marked on the figure. The nanobeam waveguides within this work have a width of $w = 300$ nm. In order to evanescently couple the optical mode from the waveguide to the disc resonator, the width of the waveguide is tapered to push the mode out of the waveguide in the region of the disc. The tapering width is varied within the initial experiments in order to determine the optimal width. The coupling from waveguide to resonator furthermore depends on

the distance, which we refer to as the *gap*. A zoom in of waveguide and resonator is depicted in Fig. 4.2b. A full matrix containing a parameter space varying both disc radius and gap size is depicted in Fig. 4.2c. The full chip contains 16 matrices with 4 different tapering widths. Each unique structure has 4 copies on the chip.

Within this work, three chips containing nanoscale devices such as disc resonators and nanobeam waveguides were fabricated and further optically characterised. An initial chip without embedded emitters was fabricated in order to show cavity response from these newly designed devices as well as to refine the parameter space, thus optimising tapering width, gap size and disc radius. A second chip was thereafter fabricated, now including embedded $InAs$ QDs. The purpose of the chip was to characterise how disc cavities affect the single photon emitters. A third chip was finally fabricated with a the goal of showing that it is possible to fabricate epoxy claddings on top of quantum devices without reducing the device functionality, and that metal wires can be crossed on top of the epoxy claddings and led to the center of the disc resonators without significantly affecting the cavity. Finally, using various amounts of epoxy allows us to estimate the magnitude of loss in the optical modes due to the epoxy cladding. The purpose of each chip is summarised in Tab. 4.1.

Optically characterised chips		
Design name	**Feature**	**Purpose**
First Mask	Plain disc resonators	Observing cavity response and refining parameter space.
Second Mask	Embedded w. $InAs$ QDs	Observing cavity response and refining parameter space.
Epoxy Mask	Epoxy claddings	Proof of concept. Estimating optical losses due to epoxy cladding.

Table 4.1.: Overview of designed and fabricated chips that were optically characterised within this work along with a brief summary of their purpose

4.2 Statistical analysis of four port disc resonators

While the ultimate objective of this work is to characterise the cavity-emitter coupling effects within the disc resonators, the characterisation of the disc resonators themselves is relevant. A thorough characterisation of the bare cavities is beneficial in order to estimate Q-factors of the devices and thereby estimate obtainable Purcell enhancement within the resonators.

The analysis throughout this chapter will be based on the data from the Second Mask sample. An analysis of the Epoxy Mask will follow in Ch. 6 while a brief summary of the First Mask analysis can be found in Appendix C. The data presented in this chapter and the next has been published in a recent publication by author and supervisors of this project [40]. Figures of this thesis show high resemblance to those of the publication.

Using the CTL and coupling into the disc resonator through the excitation port as described in Sec. 4.1, a broad spectrum frequency scan can be measured in bus port and in drop port as exemplified in Fig. 4.3a, where we used a device with disc radius $r = 3.5$ μm, gap size $d = 100$ nm and waveguide tapering width $w = 220$ nm. Here, we see a non-trivial background in the bus port due to in-coupling variation throughout the spectrum. From Fig. 4.3a it is clear that there is a high correlation between dips measured at bus port and peaks measured at drop port, confirming that the device does in fact behave as expected. By analysing the spectral distribution of the cavity modes and comparing it to the theoretical FSR of the resonator geometry, the cavity modes are separated into radial orders as marked on the figure. According to Eq. (2.1), the fundamental mode will have the smallest FSR, as the higher order radial modes will have a shorter path length within the cavity. Two second order modes have been marked with a red and an orange box. Their fits to the Lorentzian lineshape of Eq. (2.2) along with the fitted Q-factor following Eq. (2.3) are depicted in Fig. 4.3b-c. Similar fits are made on all cavity modes.

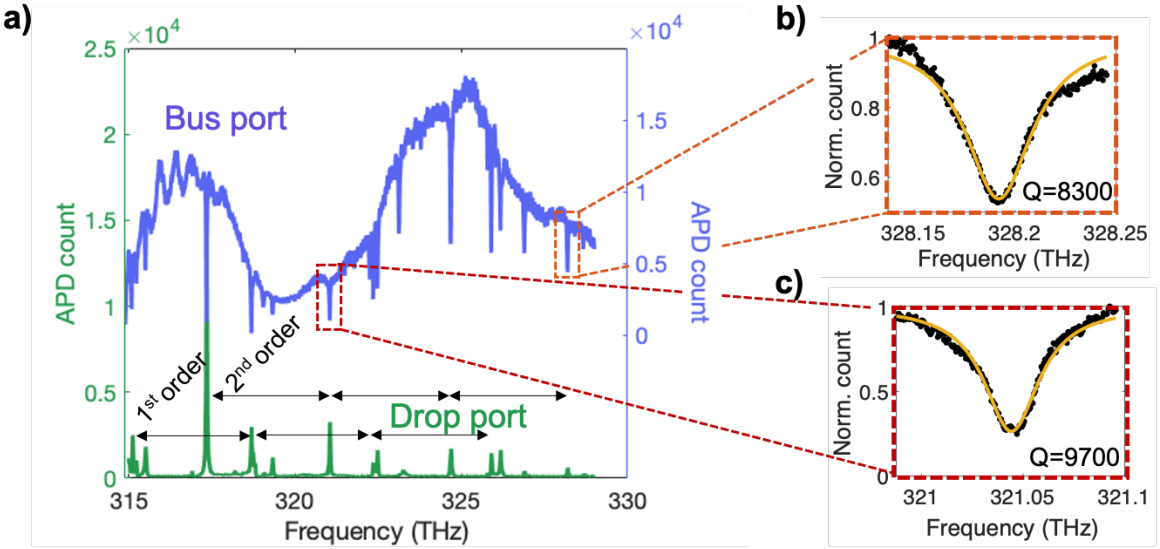

Figure 4.3.: Disc resonator with radius $r = 3.5$ μm, gap size $d = 100$ nm and waveguide tapering width $w = 220$ nm. a) Laser collection from bus port (blue) and drop port (green). Bus port data as well as drop port data is from resonant transmission through excitation port with CTL. b)-c) Zoom-in on normalised cavity modes fitted to a Lorentzian lineshape (yellow).

Frequency scans measured at bus and drop port have been made on several disc resonator devices with a range of parameters. All frequency spectra have been analysed in the same manner as seen from Fig. 4.3. The distribution of cavity Q-factors is depicted in Fig. 4.4. Here, all devices taken into account have a waveguide tapering width of $w = 220$ nm. The average Q-factor of the cavity modes across all disc radii is $\bar{Q} = 9400$, while the maximal Q-factor is > 27000. In Fig. 4.4b we see that there is no significant difference in the Q-factors between 1^{st} and 2^{nd} order radial modes. The Q-factors presented within this work are comparable to similar $GaAs$ micro resonators, such as the WGM microdisc resonators presented in Refs. [23]–[26]. Here, they obtain Q-factors > 12000 for $InAs$-QD embedded $GaAs$ microdisc resonators.

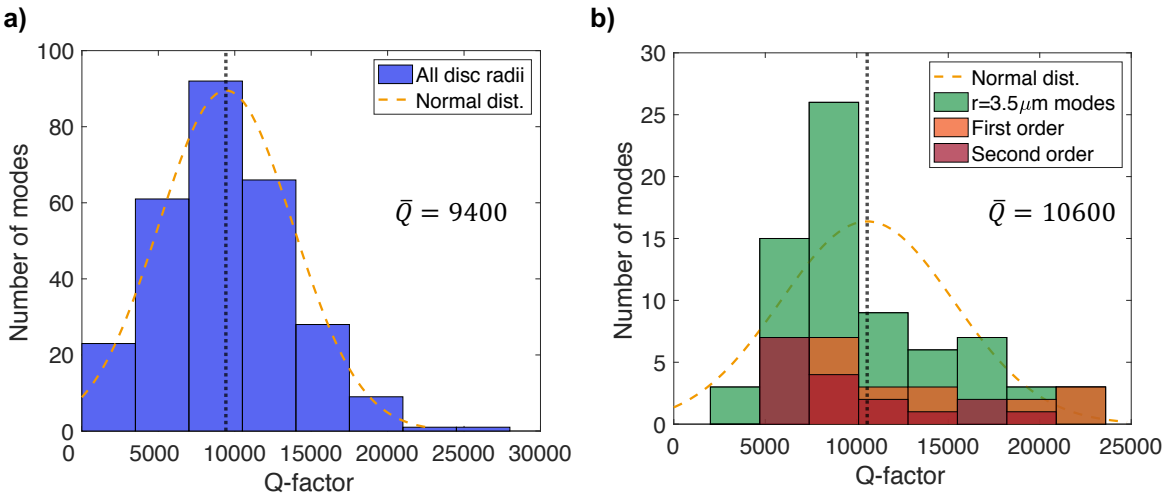

Figure 4.4.: Distribution of Q-factors from a wide range of disc resonators. a) Distribution of Q-factors from modes fitted to Eq. (2.2) in disc resonators with tapering width $w = 220$ nm, all gap sizes and all radii. b) Only for radius $r = 3.5$ μm. Modes have been separated into fundamental and 2^{nd} order modes by looking at their respective FSR.

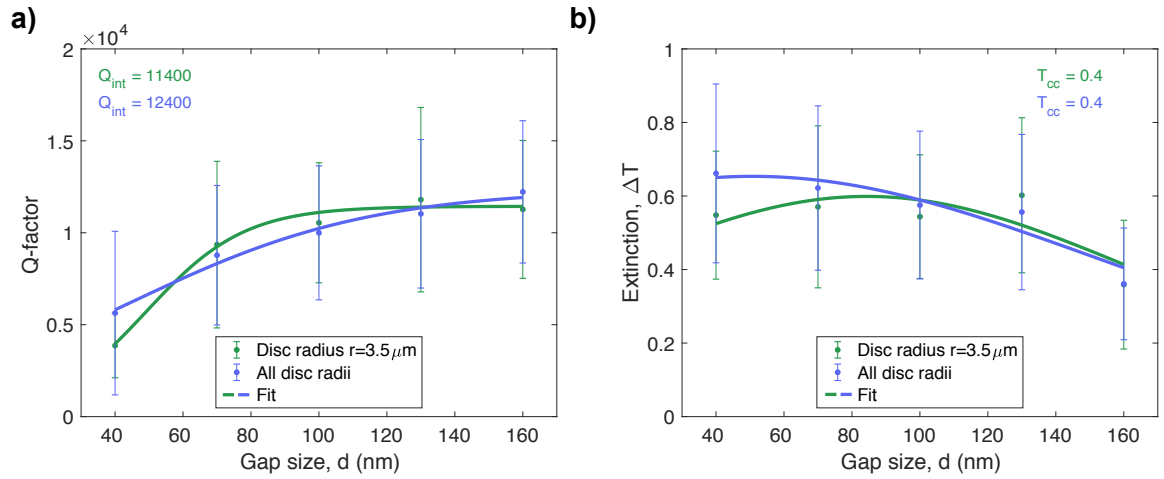

Figure 4.5.: Effects of gap size in disc resonators from Second Mask with waveguide tapering width of $w = 220$ nm. a) Average Q-factor from multiple devices at given gap size both for all disc radii (blue) and for a selected size of $r = 3.5$ μm (green). Data is fitted to Eq. (2.40b). From the fit parameters we see an average intrinsic Q-factor at around ≈ 12000. b) Average extinction, ΔT, from multiple devices at given gap size both for all disc radii (blue) and for a selected size of $r = 3.5$ μm (green). Data is fitted to Eq. (2.40a). From the fit the transmission at critical coupling, T_{cc}, is extracted.

Looking at Eq. (2.19) and by using the numerically estimated effective mode volume of a fundamental mode within the disc resonators, $V = 18(\lambda/n)^3$, along with our average Q-factor, we calculate a theoretical average Purcell enhancement of $F_{\text{theory,avg}} \approx 40$. This value is an *upper* limit of the Purcell enhancement, given our measured Q-factors. In reality, we expect lower Purcell enhancement as the QD dipole will not necessarily be ideally aligned within the polarisation of the mode.

In Fig. 4.5a we see the correlation between Q-factor and gap size, which is theoretically described by Eq. (2.40b), while Fig. 4.5b depicts the relation between extinction, ΔT, and gap size, which is theoretically described by Eq. (2.40a). All cavity modes at a given gap size are averaged to form one data point with the standard deviation as error. The green curves only take devices of radius $r = 3.5$ μm into account while the blue curves include all disc radii in the data set. There is a visible correlation between gap size and Q-factor, and it is clear that larger gap size results in higher Q-factors. Both the green and the blue curve of Fig. 4.5a fit to an intrinsic Q-factor of ≈ 12000. There is also a clear correlation between extinction and gap size. With a large gap size follows low extinction. Regarding both Q-factors and extinction there seems to be no significant difference between only $r = 3.5$ μm and all disc radii combined.

In conclusion, by scanning a broad frequency spectrum through the excitation port of the disc devices, we are able to observe high-Q cavity behaviour at bus and drop port throughout a range of varying disc designs. By investigating a range of gap sizes, disc radii and waveguide tapering widths, we obtain a further comprehension on the parameter space. No exact parameters are conclusively determined to be significantly better than others. The choice of gap size becomes a trade-off between high Q-factor and high extinction, while the disc radius does not show an impact on neither Q-factors nor extinction within our parameter space.

5 Coupling a quantum dot to a disc resonator

We now turn to the characterisation of the QDs embedded within the disc resonators. The objective is to characterise how the resonators alter the light-matter interaction between an incoming laser field and a QD. In this chapter we will first present methods to establish cavity-emitter coupling along with a statistical analysis of emitter decay rates within the sample. The chapter continues with the study of a distinguished cavity-emitter system. Here, we extract the coupling strength and routing efficiency of the cavity-emitter system. The chapter is concluded with future experimental implementations to ultimately improve the routing efficiency of the system.

5.1 Verifying quantum dots coupled to disc resonators

A coherent QD interaction within the cavity is visible as a transmission dip in the drop port as described by Eq. (2.38). Since the disc resonators have multiple radial modes a dip in transmission could, however, also be introduced by two cavity modes within close spectral vicinity. In this section, we explain the requirements that must be met in order for us to validate a transmission dip as coherent QD interference.

Using the high-energy Tsunami laser at a wavelength of ≈ 820 nm we excite QDs above band. In order to gauge the inhomogeneous broadening of the QD spectrum, we direct the beam to a coupler grating connected to a straight nanobeam waveguide in-coupler grating. Emission is collected at the other grating out-coupler, and sent to a spectrometer, as was discussed in the previous chapter. Additionally, we can align the grating to a QD-resonance and send the collection through the lifetime setup, thus measuring the lifetime of a bulk QD. Having done this for multiple QDs and by averaging their measured bulk decay rates, we estimate the average bulk decay of the QDs embedded in this wafer to be $\gamma_{\text{bulk}} = (0.10 \pm 0.07)$ GHz.

By aligning the Tsunami laser onto a disc and collecting at any device port, we are able to measure all cavity-resonant QD-emission. Only emission resonant with the cavity will emit into the cavity modes and be able to couple out of the disc and into the access waveguides. When doing the large frequency scans depicted in Fig. 4.3a we were able to observe transmission dips (in drop port) and peaks (in bus port) within the cavity mode. Examples of transmission dips are shown in Fig. 5.1b-c. In order to confirm that these are in fact QDs coupled to the respective cavity modes, we perform several measurements. Examples of all measurements are given in the following section:

- **Temperature tuning:** An increase in temperature redshifts the QD resonance. An increase in temperature can furthermore alter the strain of the disc resonators, thus altering the cavity resonances, but this occurs on a significantly smaller order than the redshift of the QD [34].

- **Power saturation:** As the QD has a finite decay rate, pumping it resonantly at high power will saturate the TLS, thus quenching the single photon emission. An increase of transmitted power therefore eliminates the QD-dip from transmission. The saturation parameter S of Eq. (2.38) thereby affects the depth of the QD-dip.

- **Lifetime measurement:** A QD on resonance with the cavity mode will have the maximal Purcell enhancement, and by altering the temperature we detune the QD from the cavity. By exciting a QD above band and measuring its temperature dependent lifetime, we can be certain that we in fact have a coupled cavity-QD system.

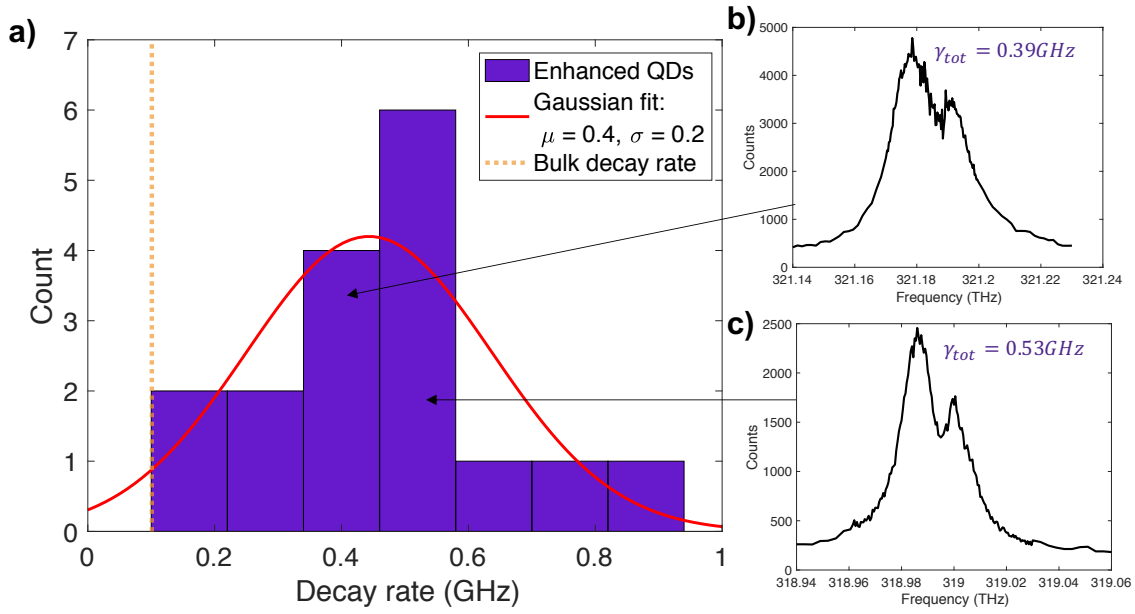

Figure 5.1.: a) Histogram of maximally enhanced decay rate of coherent QDs in disc resonators, together with a Gaussian fit to the histogram. Average decay rate of enhanced QDs is $\gamma_{\mathrm{tot,mean}} = 0.4$ GHz, while the average bulk decay rate is measured to be $\gamma_{\mathrm{bulk}} = (0.10 \pm 0.07)$ GHz. Resonant transmission measured in drop port in two different devices: b) $r = 4$ μm, $d = 130$ nm, $w = 220$ nm, $T = 13$ K and c) $r = 3.15$ μm, $d = 130$ nm, $w = 220$ nm, $T = 13$ K, in which a coherent QD dip is visible.

By performing these measurements, we can ensure that a given data set is in fact that of a coupled cavity-QD system. Doing a less rigorous investigation and omitting the saturation measurements, however, still indicates a coupled cavity-QD system. This routine has been applied to cavity-QD systems on our chip. The measured enhanced decay rates are depicted in Fig. 5.1a, where we see that all measured enhanced QDs have a decay rate larger than that of the average bulk decay rate. The average optimally enhanced decay rate is $\gamma_{\mathrm{tot,avg}} = (0.4 \pm 0.2)$ GHz, meaning that on average, the QD-emission is enhanced by a factor 4 by the disc resonators. In Fig. 5.1b-c we see further examples of a coherent QD dip in drop port transmission scans. Every coupled cavity-emitter system represented by a decay rate plotted in the histogram of Fig. 5.1a has a similarly looking transmission scan. The

histogram contains 17 data points of different QDs in disc resonators. In order to improve the statistics of the enhanced decay rates, it would have been beneficial with a larger set of data. However, given the long duration of the measurement routine, this has not been prioritised for the scope of this work.

5.2 Exemplary cavity-QD coupling

In this section we investigate an exemple of a QD coupled to a cavity. The cavity in question has a radius $r = 3.5$ μm, a gap size of $d = 100$ nm and a waveguide tapering width of 220 nm. The raw data of the frequency scan of this specific cavity was presented in Fig. 4.3. This measurement is done with an input power of $P = 5$ μW at 7 K.

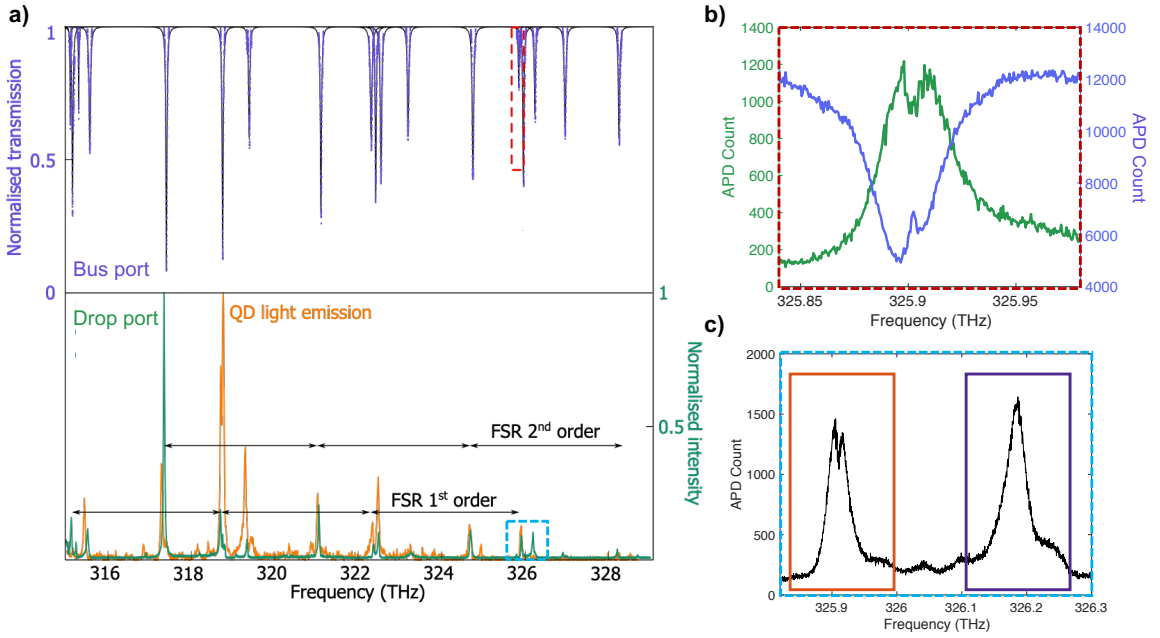

Figure 5.2.: Measurements on device with radius $r = 3.5$ μm, gap size of $d = 100$ nm and waveguide tapering width of 220 nm at $T = 7K$ and input power $P = 5$ μW. a) Normalised resonant transmission in bus port (blue) and drop port (green) along with QD emission from above band excitation on disc (yellow). b) Zoom-in on fundamental mode with characteristic QD interference. c) Zooming-in showing fundamental mode (orange) and second order mode (purple) in close spectral vicinity.

The blue curve of Fig. 5.2a shows the bus port data. Here, we have normalised and fitted all cavity modes as described in Sec. 4.2. We have additionally plotted the QD emission from above band excitation on the disc with the yellow curve. Here, we see that the out-coupled emission is highly correlated to the measured cavity modes in drop port. Zooming in on the resonant transmission of the fundamental cavity mode at frequency $f = 325.9$ THz in Fig. 5.2b, we observe a characteristic QD dip and peak in drop port and bus port, respectively. Here, the QD is on resonance with the cavity. We furthermore notice an asymmetry in the drop port data, as the transmission at higher frequencies does not go fully down to the dark count level. This is due to a second order cavity mode at higher frequency affecting the fundamental mode as seen in Fig. 5.2c.

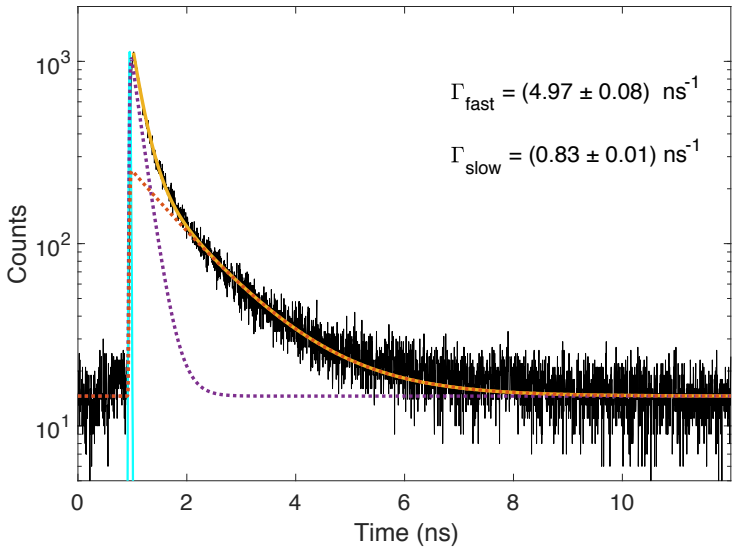

Figure 5.3.: Lifetime measurement of a QD on resonance with cavity using a fast single photon detector with instrument response function (IRF) curve depicted in blue. Data is fitted to a biexponential decay (yellow) with fast component (purple dotted) $\gamma_{\text{fast}} = (4.97 \pm 0.08)$ ns^{-1} and a slow component (orange dotted) $\gamma_{\text{slow}} = (0.83 \pm 0.01)$ ns^{-1}.

The QD is on resonance with the cavity at $T = 7$ K. A lifetime measurement of the coupled QD is depicted in Fig. 5.3. The lifetime measurement is done using a time-correlated single photon system, PicoHarp, as described in Sec. 4.1. Here, we have fitted the data to a biexponential decay. We attribute the two decay rates to the two orthogonally polarised QD transition dipoles [34]. One dipole (the fast component, γ_{fast}) is well-aligned with the incoming field while the other is orthogonal to the well-aligned dipole and thus weakly coupled to the incoming field (γ_{slow}). We obtain a fast decay rate[1] of $\gamma_{\text{tot,fast}}/2\pi = \gamma_{\text{cav}}/2\pi + \gamma_{\text{leak}}/2\pi = (0.79 \pm 0.01)$ GHz for the well-coupled dipole, while we obtain a slow decay rate of $\gamma_{\text{slow}}/2\pi = (0.31 \pm 0.002)$ GHz for the weakly-coupled dipole. By comparing the decay rate of the well-coupled dipole $\gamma_{\text{tot,fast}}$ to that of the bulk decay rate γ_{bulk}, we obtain a cavity-induced lifetime enhancement of 7.9.

5.2.1 Power saturation of quantum dot

The linewidth of the QD is given by $\gamma_{\text{tot}} = \gamma_{\text{cav}} + \gamma_{\text{leak}}$. Following the transmission equation, Eq. (2.38), there are two factors leading to an emission linewidth broadening, as observed in the frequency transmission scans; pure dephasing, γ_{dp}, and spectral diffusion, σ_{sd}. From lifetime measurements alone we have now established values for γ_{cav} and γ_{leak}. Following the reported results of Ref. [63], we estimate pure dephasing rate of the embedded QDs to be $\gamma_{\text{dp}} = 0.01$ GHz within the temperature range of 6 K – 12 K.

By repeating the drop port frequency scan of Fig. 4.3c at increasing power of the CTL excitation laser at constant temperature $T = 7$ K, we obtain the data depicted in Fig. 5.4a. Here, the background

[1] While lifetime measurements are performed in time domain yielding $\gamma_{\text{fast}} = (4.97 \pm 0.08)$ ns^{-1} we prefer to write the decay rates in angular frequency, $\gamma_{\text{fast}}/2\pi = (0.79 \pm 0.01)$ GHz, in order to compare QD decay rates with cavity linewidths.

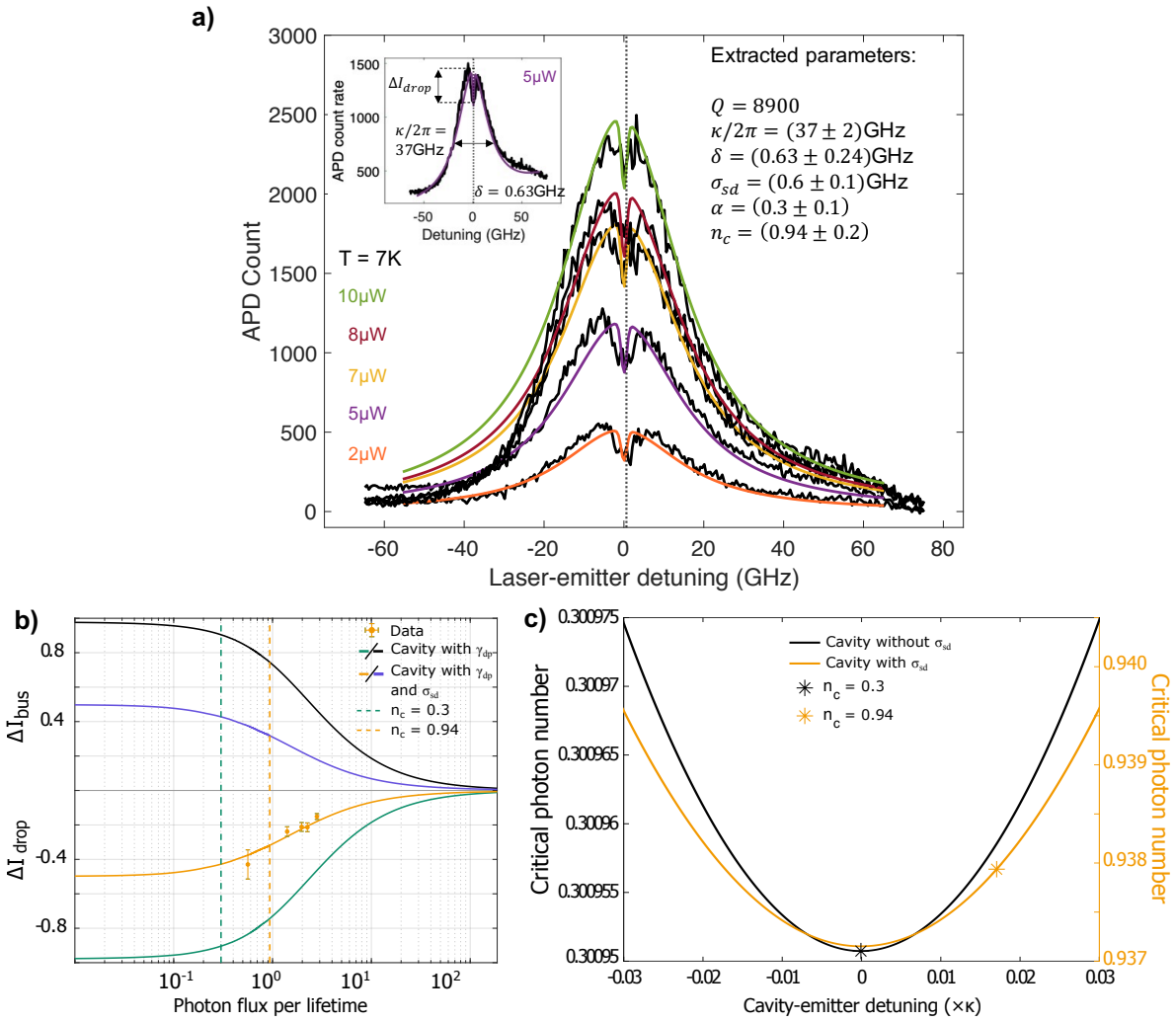

Figure 5.4.: Power tuning of the QD at temperature $T = 7$ K. a) 5 sets of power tunings fitted simultaneously in order to estimate the parameters of Eq. (2.38). The background due to a second order mode in the spectral vicinity of our primary cavity has been subtracted during the fitting routine. b) Measured extinction data at $\delta = 0.6$ GHz as a function of power (yellow dots) compared to the theoretical predicted extinctions with (yellow curve) and without (green curve) spectral diffusion σ_{sd}. The critical photon numbers for the case with and without σ_{sd} are shown as vertical dashed lines and found using 2.33. c) Following Eq. 2.33, the critical photon number varies according to cavity-emitter detuning δ, here as a function of cavity linewidth.

due to the spectrally adjoining second order cavity mode has been subtracted. This is done by fitting our fundamental cavity mode to the sum of Eq. (2.38) and the Lorentzian lineshape, Eq. (2.2), at the frequency of the second order mode. Subsequently, we subtract the fitted Lorentzian to eliminate the background. Returning to our primary cavity mode, this allows us to obtain the cavity linewidth, κ, along with the remaining QD-parameters being the cavity-emitter detuning, δ, and the spectral diffusion, σ_{sd}. The fitting of the power dependent data furthermore allows us to obtain the coupling efficiency parameter, α, from Eq. (2.35) as the input power through the access waveguides corresponds to the incident number of photons, n_{in}. From the same equation we are likewise able to obtain the saturation parameter S at all input powers. All fitted variables are presented in Fig. 5.4a.

The depth of the transmission dip is termed QD-extinction and labelled ΔI as indicated in the inset of Fig. 5.4a. The QD-extinction at each power is plotted in Fig. 5.4b as a function of photon flux per lifetime, which is found using the critical photon number. The critical photon number, n_c, given by Eq. (2.33), is defined by the cavity and QD parameters and marked by the yellow dashed line in Fig. 5.4b. We estimate the critical photon number to $n_c = (0.94 \pm 0.2)$ at a cavity-emitter detuning of $\delta = 0.02\kappa$. This is a noteworthy result as a value < 1 suggests operation at single-photon level. We model the power-dependent saturation curve of Eq. (2.38) at $\delta = 0.6$ GHz, as depicted in yellow in Fig. 5.4b.

The minimally measured[2] QD-extinction measured in the drop port at power $P = 2$ μW is given by[3] $\Delta I_{\mathrm{drop},2\mu\mathrm{W}} = (-43 \pm 8)\%$, where these photons are re-routed into the drop waveguide by the QD. By comparison, a peak extinction of 8% has previously been reported for non-electrically contacted QDs, using slow-light photonic crystals [64]. In the low power regime of $S = 0$ we extrapolate a maximal extinction of $\Delta I_{\mathrm{drop,max}} = (-53 \pm 4)\%$. By modelling our system and excluding the spectral diffusion, $\sigma_{\mathrm{sd}} = 0$ GHz, we obtain a drop port saturation curve given by the green line in Fig. 5.4b. By eliminating the charge noise induced spectral diffusion, we expect a low-power maximal extinction of $\Delta I_{\mathrm{drop,max}} = (-98 \pm 2)\%$. Looking at Fig. 5.4c we additionally see that this would result in a lowering of the critical photon number to $n_c = 0.3$. Given the expected high extinction and low critical photon number, it would be intriguing to perform these measurements with electrically contacted structures, as the charge noise would in this case become negligible [34].

In summary, from a lifetime measurement of the QD on resonance with the cavity, we measured a decay rate of $\gamma_{\mathrm{tot}}/2\pi = (0.79 \pm 0.01)$ GHz. By varying the excitation power, resonant transmission and excitation of the cavity-QD system was performed. By simultaneously fitting the power series we were able to extract relevant cavity and QD parameters, ultimately leading to a critical photon number of $n_c = (0.94 \pm 0.2)$. The maximal extinction measured is given at $\Delta I_{\mathrm{drop},2\mu\mathrm{W}} = (-43 \pm 8)\%$ while the maximal extinction in our system is modelled to be $\Delta I_{\mathrm{drop,max}} = (-53 \pm 4)\%$.

5.2.2 Coherent routing of single photons

Up until this point, all data analysis of the cavity-QD coupling has been made with data collected in the drop port. When studying single-photon routing, we need to observe the absent photons in the drop port routed to another channel. Within this design, the photons are re-routed to the bus port, as has been measured and shown in Fig. 5.2b. By altering the temperature and doing resonant transmission with collection in both bus and drop port, we can observe the single-photon routing at varying detuning, as depicted in Fig. 5.5. As the cavity-QD coupling is strongest when the QD is on resonance, the routing efficiency is also expected to be at a maximum when cavity and emitter are on resonance. Within our temperature tuning range (6 K to 12 K) the QD resonance is tuned from $\delta = -0.3\kappa$ to $\delta = 0.09\kappa$, which is visible in both bus and drop port marked by ΔI_{bus} and ΔI_{drop}, respectively. We note that there is an asymmetry in the bus port measurements relative to the drop port measurements, making it seem as if the QD is differently detuned between the two ports. The lifetime measurements indicate maximal enhancement at $T = 7$ K, which supports the cavity-QD detuning found by drop port measurements, therefore we attribute this asymmetry to the irregular background of the bus

[2] Further power-dependent measurements were performed at even lower powers than depicted in Fig. 5.4a, but the signal-to-noise ratio became too poor to obtain good fit results.
[3] We will use negative values, $\Delta I_{\mathrm{drop},2\ \mu\mathrm{W}} = (-24 \pm 4)\%$, to indicate measurements done in drop port.

port measurements as discussed in Sec. 4.2. When fitting the sets of data depicted in Fig. 5.5 with

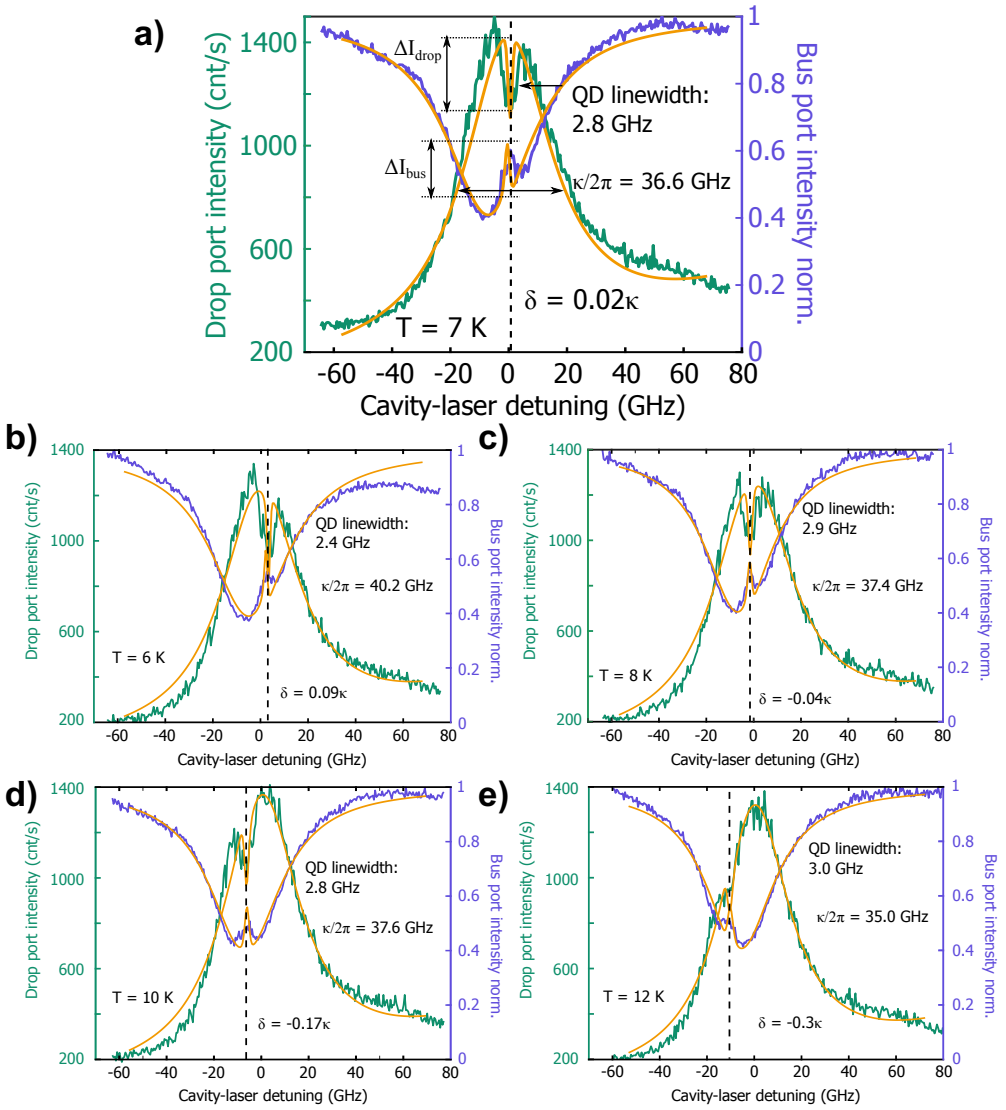

Figure 5.5.: Resonant transmission in our primary mode at input power $P = 5\ \mu$W and at various temperatures from 6K to 12K showing a resonance tuning of the QD in a)-e). Here, drop port data is depicted in green and bus port data in blue while the theoretical fits are depicted in yellow. The QD is on resonance with the cavity in a).

Eq. (2.38) we use the saturation parameter $S = 1.5$ at input power $P = 5\ \mu$W as obtained from the power fitting routine. From the figure we clearly see how the QD-resonance is tuned across the cavity resonance. From the fits we attain a correlation between cavity-QD detuning, δ, and temperature and also between spectral diffusion, σ_{sd} and temperature. Both temperature-dependent parameters are depicted in the inset of Fig. 5.6. Here, both δ and σ_{sd} are fitted to linear curves with respect to temperature. While cavity-QD detuning is expected to have a prominent temperature dependency, it is not obvious that the spectral diffusion would show a similar trend. Temperature dependence of spectral diffusion is non-trivial as it depends on the nature of the charge noise, which will vary from sample to sample. For electrical conductors, including quantum dots, the Johnson-Nyquist noise is a well-known linearly temperature dependent heat and charge noise [65]. While we have assumed a constant pure

dephasing rate throughout this work, it *is* possible that an amount of the QD-linewidth broadening is in fact due to pure dephasing or heat noise, and not solely due to an increase in spectral diffusion. This would require further investigation. For the time being, we will treat the broadening as charge noise-induced spectral diffusion.

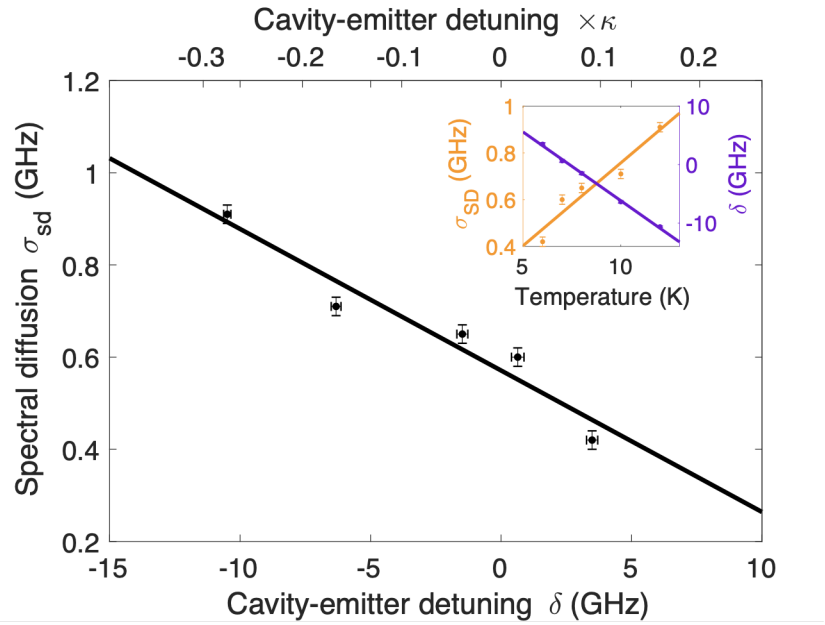

Figure 5.6.: The fitted spectral diffusion (σ_{sd}) varies linearly according to temperature as seen in the inset (yellow) and so does the cavity-emitter detuning (δ) (purple), resulting in a linear relation between σ_{sd} and δ as shown in the main figure.

Since both the cavity-emitter detuning, δ, and the spectral diffusion, σ_{sd}, have a linear dependency on temperature, they can additionally be fitted linearly to each other as depicted in Fig. 5.6. This fitting becomes relevant when we set out to model the cavity-QD interaction as a function of cavity-emitter detuning. The QD-extinction, ΔI, is expected to be largest when the QD is on resonance with the cavity ($\delta = 0$ GHz), as depicted by the solid line in Fig. 5.7. From the inset we clearly see a parabolic shape of the expected QD-extinction as a function of cavity-emitter detuning. However, by including the convolution of the linearly increasing spectral diffusion, σ_{sd}, found from temperature tunings, we obtain the dashed yellow curve in Fig. 5.7. From this, we see that large positive detuning would theoretically result in a higher extinction than when the QD is on resonance. Since a blue-shift of the QD-resonance is obtained by *lowering* the temperature, this is in accordance with our results.

From the transmission measurements and fits depicted in Fig. 5.5 and from the linear fit of the cavity-emitter detuning, δ, we are able to plot the QD extinction as a function of cavity-emitter detuning as depicted in Fig. 5.8a. Here, the yellow dashed line and the yellow solid line correspond to the system with and without spectral diffusion, respectively. We see that the measured QD extinction follows the theoretical curve both in bus port and drop port. Fig. 5.8a effectively illustrates the photon re-routing efficiency of the system as we can here see that while the drop port extinction, ΔI_{drop}, becomes more negative (as we approach cavity-emitter resonance from negative detuning), the bus port extinction, ΔI_{bus}, becomes more positive. This shows that photons are being routed from one channel to the other. For saturation level $S = 1.5$ a maximum of $\Delta I_{\mathrm{drop}} = (-23 \pm 3)\%$ of the single photons are seen to be

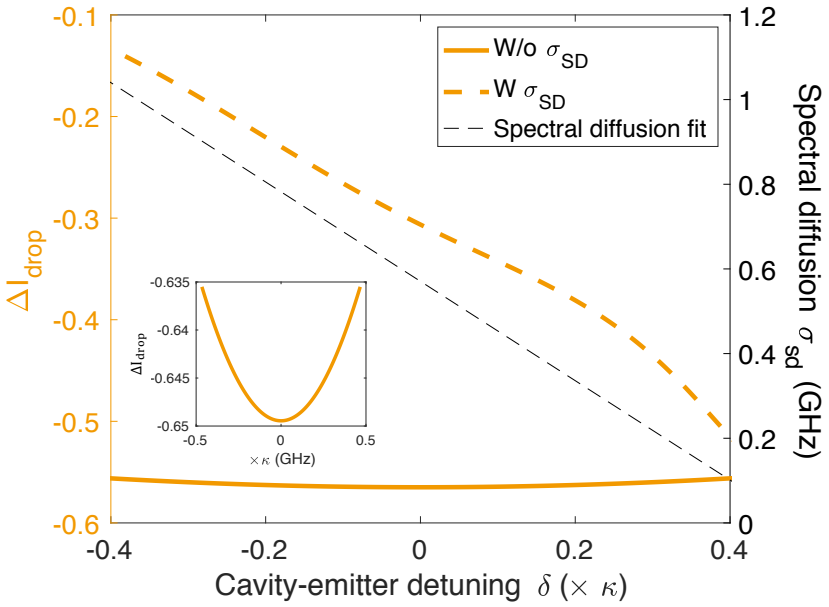

Figure 5.7.: Theoretical drop port QD extinction (ΔI_{drop}) as a function of cavity-emitter detuning. Solid yellow line shows a parabolic extinction as a function of detuning (also seen from inset) while the linear spectral diffusion (black dashed line) results in an extinction pattern that does *not* peak at resonance (yellow dashed line).

routed between the two ports[4]. Theoretically, we calculate our system to have a peak routing efficiency of $\Delta I = (31 \pm 4)\%$. The switching strength of the device is depicted in Fig. 5.8b. Here, the transmission through the cavity-emitter system at cavity resonance ($\Delta f = \omega_{\text{cav}} - \omega_{\text{laser}} = 0$ GHz) is measured and compared to the theoretical transmission through a bare cavity given by Eq. (2.2) as a function of cavity-emitter detuning. While the QD is on resonance with the cavity we experimentally measure a re-routing efficiency of $(23 \pm 3)\%$ on cavity resonance, as previously mentioned. From Fig. 5.8b we furthermore see that the minimally measured efficiency of the routing device is $(1 \pm 3)\%$ measured *on cavity resonance* with a QD detuning of $\delta = -0.28\kappa$. This implies that the cavity resonance is barely affected by the cavity-emitter coupling while at this cavity-emitter detuning. From these curves we can observe how the WGM-device can be used as a coherent photon router in practice. For our system we observe that a QD-detuning of $\delta = 0.39\kappa$ (corresponding to a temperature change of only 6 K) is sufficient to completely switch off the routing device. This detuning corresponds to a shift the size of 5.1 QD-linewidths, which is achievable using temperature tuning.

Temperature control within a cryostat is, however, slow compared to other control mechanisms such as stage placement and electric field control. By using a p-i-n heterostructure as wafer, the band structures of the QD can be controlled by applying a bias voltage. By electrically contacting disc resonators fabricated onto such a wafer, we would be able to control the resonance frequency of the QD via DC Stark tuning [43] with high precision, thus being able to alter the efficiency of the routing within the device. By applying an electric field across the devices we furthermore eliminate charge noises ($\sigma_{\text{sd}} = 0$ GHz). This is modelled by the dashed lines in Fig. 5.8a-b. For such a system we expect a peak efficiency of $\Delta I = (56 \pm 3)\%$, while operating with the same level of saturation. An electrically gated

[4]Regrettably, no cavity-emitter detuning experiments at $P = 2$ μW were performed

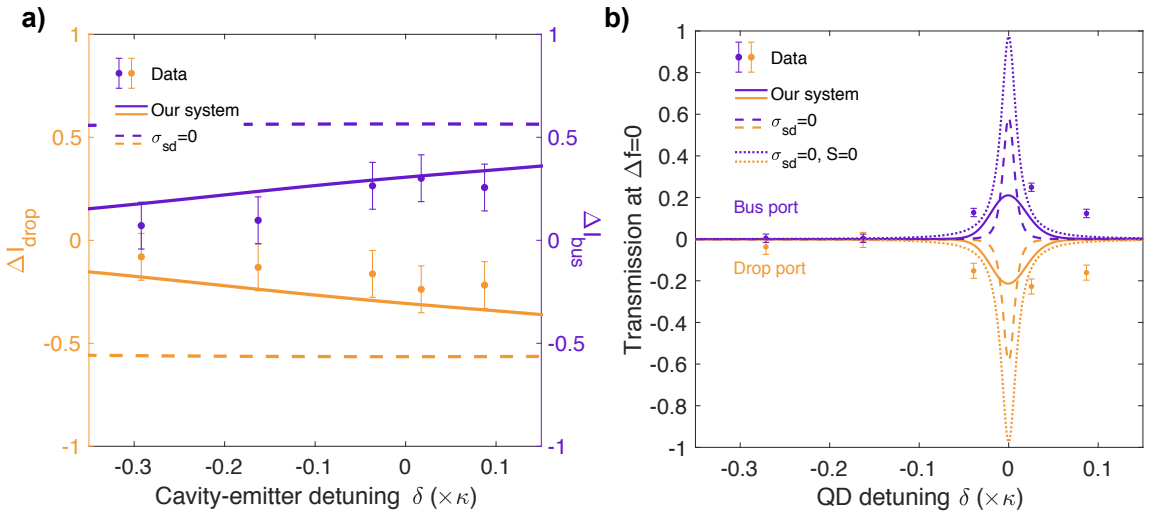

Figure 5.8.: Tuning the QD across the cavity at $S = 1.5$. a) QD extinction in drop port (yellow) and bus port (purple) as a function of cavity-emitter detuning (δ) along with the theoretical curves with spectral diffusion (solid) and without spectral diffusion (dashed). b) Switching strength measured as extinction at cavity resonance as a function of cavity-emitter detuning (δ) along with theoretical curves. The solid lines include the fitted spectral diffusion and saturation parameter while the dashed lines assume no spectral diffusion and the dotted lines assume both low power and no spectral diffusion ($S = 0$, $\sigma_{\mathrm{sd}} = 0$ GHz) .

system in the low power regime ($\sigma_{\mathrm{sd}} = 0$ GHz, $S = 0$) is expected to have a peak routing efficiency of $\Delta I = (98 \pm 2)\%$.

In conclusion, spectral tuning of the QD is an effective method of controlling the routing device. Throughout this work, this has been achieved through temperature tuning. Applying a tuning range from 6 K − 12 K we observe coherent routing of single-photons at a measured maximal efficiency of $\Delta I_{\mathrm{drop}} = (-23 \pm 3)\%$. We furthermore find that the routing device is completely switched off at a detuning of $\delta = 0.39\kappa$, corresponding to a temperature change of $6K$, while the minimal switching strength is measured at $\Delta I_{\mathrm{drop}} = (-1 \pm 3)\%$ at a detuning of $\delta = -0.28\kappa$.

5.2.3 Purcell enhancement and coupling strength of coupled system

Another factor determining the routing efficiency of the device is the Purcell enhancement. Given the estimated mode volume of the first order mode we can calculate an upper bound of the expected Purcell factor using Eq. (2.19), yielding $F_{\mathrm{ideal}} = 38$. This is the expected Purcell factor if the QD dipole was physically located at the cavity-mode maximum.

In Fig. 5.9 we observe how temperature tuning affects the decay rate, thus increasing the emission enhancement. A fast (blue) and a slow (yellow) component has been fitted to each lifetime measurement. We notice that even the slow component is slightly affected by the Purcell enhancement. As the QD is tuned out of the cavity (around $T = 12$ K) we see the slow component going towards the bulk decay rate marked with the black dashed line. At $T = 7$ K we measure a decay rate of $\gamma_{\mathrm{tot,fast}}/2\pi =$

$\gamma_{cav}/2\pi + \gamma_{leak}/2\pi = (0.79 \pm 0.01)$ GHz for the well-coupled dipole, while we obtain a slow decay rate of $\gamma_{slow}/2\pi = (0.31 \pm 0.002)$ GHz for the weakly-coupled dipole. Since we assume that $\gamma_{bulk} \approx \gamma_{leak}$, we can estimate the Purcell enhancement using Eq. (2.22), giving us an experimental Purcell factor of $F_{exp} = 6.9 \pm 0.9$.

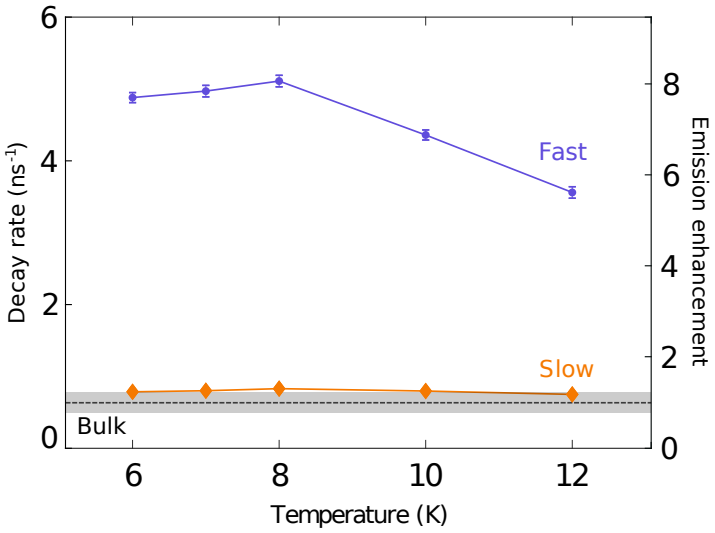

Figure 5.9.: Lifetime measurements from above-band excitation on disc at $f = 325.9$ THz at varying temperature. A biexponential fitting yields a fast (blue) and a slow (orange) component of the QD. The bulk decay rate, γ_{bulk}, along with its standard variation is depicted by the black dashed line and the grey area. Right axis shows ratio between bulk *GaAs* decay rate, γ_{bulk} and measured decay rate.

By extracting the cavity and QD parameters from the power-dependent fitting routine, we are able to estimate the coupling strength, coupling efficiency and cooperativity of our system, following Eqs. (2.23)-(2.25). For the coupling strength we obtain $g/2\pi = (2.5 \pm 0.3)$ GHz. Given the factors $\{g, \kappa, \gamma_{tot}\}/2\pi = \{2.5, 36.6, 0.79\}$ GHz it is clear that the cavity-emitter coupling is within the weak-coupling regime. For the β-factor we obtain an experimental value of $\beta = 0.87 \pm 0.01$, meaning that the control of the single-photon emission is comparable to contemporary standards [43]. Lastly, we estimate the cooperativity of the coupled cavity-emitter system to be $C = 6.9 \pm 0.9$. Following Eq. (2.26) this will yield a cavity quantum electrodynamics Bell-state analyser success rate of $P_{success} = (86 \pm 11)\%$. For commercial use, this success rate would have to approach $\approx 100\%$.

As previously discussed, a large Purcell enhancement results in an increased emission rate of single photons into the cavity modes as $\gamma_{cav} = F\gamma_0$. The emitter-cavity coupling efficiency is described by the β-factor, and the effects of Purcell enhancement on the emission into cavity modes are depicted by the green curve in Fig. 5.10a. Our experimentally found Purcell factor of $F_{exp} = 6.9 \pm 0.9$ and the subsequent β-factor of $\beta_{exp} = 0.87 \pm 0.01$ would potentially rise to $F_{ideal} = 38$ and $\beta = 0.97$ if we were able to control the location and alignment of the coupled QD. From this follows a decrease of the relative effects of decoherence mechanisms such as spectral diffusion, σ_{sd}, and pure dephasing, γ_{dp} [66], as depicted by the red curves in Fig. 5.10a.

Likewise, looking at Fig. 5.10b we see that by increasing the Purcell enhancement from $F_{exp} = 6.9 \pm 0.9$ to $F_{ideal} = 38$, we also decrease the critical photon number to $n_{c,F=38} = 0.3$. However, our experimental Purcell factor is already sufficient to obtain a critical photon number < 1. Finally, the increase in

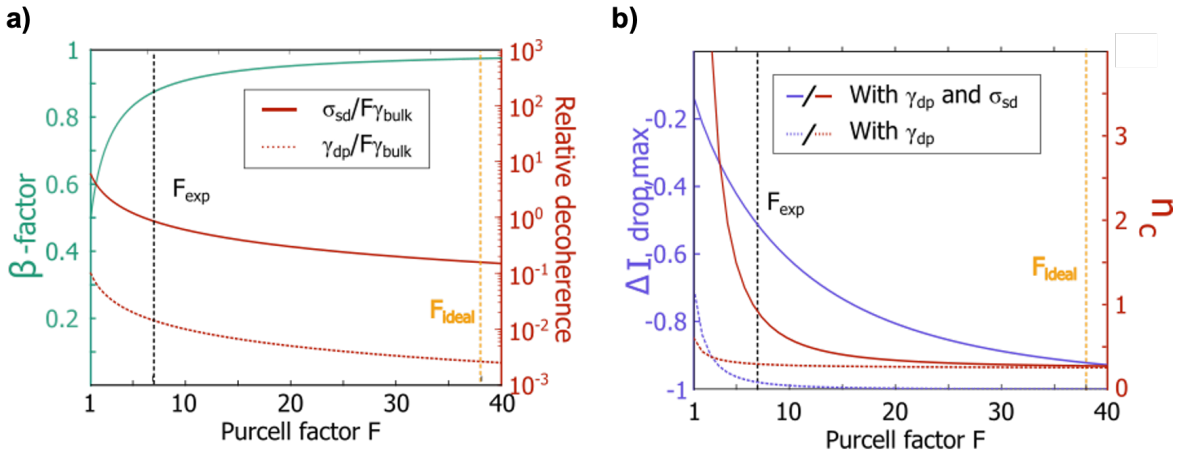

Figure 5.10.: Effects of Purcell enhancement. a) Theoretical β-factor (green) and relative decoherence defined as $\sigma_{\mathrm{sd}}/F\gamma_{\mathrm{bulk}}$ or $\gamma_{\mathrm{dp}}/F\gamma_{\mathrm{bulk}}$ as a function of Purcell factor F. Vertical lines are shown at our experimentally measured Purcell factor of $F = 6.9$ (black) and at the theoretical maximum $F = 38$. b) Maximal outing efficiency from drop port, $\Delta I_{\mathrm{drop,max}}$ and critical photon number, n_{c}, both with and without spectral diffusion, σ_{sd}.

Purcell enhancement leads to an increase of the maximal QD extinction (effectively being the routing efficiency) from $\Delta I_{\mathrm{drop,max,exp}} = (-53 \pm 4)\%$ to $\Delta I_{\mathrm{drop,max,ideal}} = (-93 \pm 4)\%$.

In summary, the experimental maximal Purcell enhancement of the QD measured from a lifetime measurement is given by $F_{\mathrm{exp}} = (6.9 \pm 0.9)$. The coupling parameters of our cavity-emitter system are given by $\{g, \kappa, \gamma_{\mathrm{tot}}\}/2\pi = \{2.5, 36.6, 0.79\}$ GHz, indicating operation within the weak-coupling regime. While we at $F_{\mathrm{exp}} = (6.9 \pm 0.9)$ observe a critical photon number $n_{\mathrm{c}} < 1$, the maximal routing efficiency of our system is $\Delta I_{\mathrm{drop,max}} = (-53 \pm 4)\%$. From calculations of the mode volume, the upper limit Purcell factor for an ideally aligned QD is given by $F_{\mathrm{ideal}} = 38$. Achieving this Purcell enhancement would result in a maximal routing efficiency of $\Delta I_{\mathrm{drop,max}} = (-93 \pm 4)\%$. In the following section we will discuss methods for realising these improvements for the optical router.

5.2.4 Towards experimental realisation of high-efficient optical routing

Having discussed multiple ways of increasing the routing efficiency, we summarise the theoretical effects of these approaches in Fig. 5.11. Here, we see that a combination of low power and elimination of spectral diffusion ($S = 0$ and $\sigma_{\mathrm{sd}} = 0$ GHz) is sufficient to achieve a routing efficiency of $\Delta I = (98 \pm 2)\%$. Combining all discussed controllable factors ($\sigma_{\mathrm{sd}} = 0$ GHz, $S = 0$, $F = 38$) we approach 100% efficiency of our routing device.

Every method of increasing routing efficiency shown in Fig. 5.11 pose experimental challenges. An experimental implementation is the power control for getting the system towards $S \to 0$. From Fig. 5.4a we see that measurements done at $P = 2$ μW have a maximal count rate at ≈ 500 counts. Higher count rate can be obtained by increasing the integration time of the APD. This would, however, not influence the signal-to-noise ratio, which has been the limiting factor when measuring at low powers within this

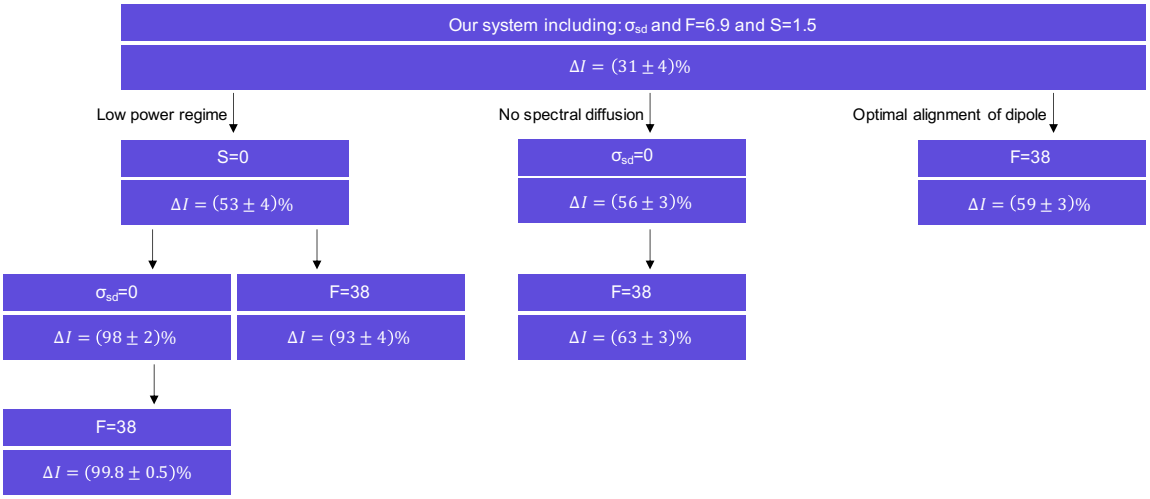

Figure 5.11.: Increases in routing efficiency, ΔI, in disc resonator routing devices by applying low power ($S = 0$), elimination of charge noise via electrical contacts ($\sigma_{\mathrm{sd}} = 0$ GHz) and deterministic placement of QD ($F = 38$).

work. However, by optimising the collection path of the experimental setup, the signal-to-noise ratio can be lowered, thus making a low-power regime of operation a reality.

As the effective mode volume of the cavity mode depends on the dipole placement and alignment within the cavity, the Purcell factor is highly governed by the physical location of the QD within the cavity. As the QDs are epitaxially grown, their positions within the devices are random. It is therefore rare to find a resonant QD well-positioned and well-aligned within the cavity mode. The deterministic growth of QDs is an ongoing field of research of its own [30], [67], [68]. Methods for locating epitaxially grown QDs using micro-photoluminescence and fabricating nanoscale devices around these QDs have been investigated [69], [70].

Finally, the elimination of spectral diffusion could be obtained by electrically contacting the disc resonators and tuning the QDs within. This approach not only reduces charge noises, but also allows for a broader selection of QDs, as non-resonant but well-aligned QDs can be tuned into resonance. The challenges imposed by electrically contacting isolated devices are described in Sec. 3.3 and include the fabrication of metal wires above and across trenches. Initial investigations have been made concerning the possibility of contacting the discs with metal wires and the results are displayed in the next chapter.

In conclusion, we have within this work successfully coupled a QD to a WGM disc resonator with a coupling strength of $g/2\pi = (2.5 \pm 0.3)$ GHz and a cavity-emitter emission efficiency of $\beta = 0.87 \pm 0.01$. With a Purcell enhancement of $F = 6.9 \pm 0.9$ at saturation level $S = 1.5$ we measure a maximal routing efficiency of $\Delta I_{\mathrm{drop}} = (-23 \pm 3)\%$. Various experimental implementations are expected to lead to a higher routing efficiency, and initial investigations towards electrically contacting individual disc resonators have been made within this work.

6 Optical characterisation of disc resonators with epoxy claddings and metal wires

While the electrical contacting of individual disc resonators could potentially increase the single photon routing efficiency to near unity, it is in itself a fabricational challenge to access the isolated disc resonators with metal wires. In order to achieve this, we propose a solution using epoxy claddings on top of the devices, that connect the unpatterned wafer with the isolated disc as discussed in Sec. 3.3. As seen in the fabrication results depicted in Fig. 3.11e-f, we succeeded in creating metal wires crossing from the wafer onto the disc resonators. In this chapter, we will investigate how the epoxy claddings, the metal wires and the metal pads on the disc affect the optical modes within the disc. We will demonstrate the functionality of the epoxy cladded devices and compare them to the regular disc resonators. By analysing the optical Q-factors of the epoxy cladded devices we can estimate the losses introduced by the claddings.

6.1 Measuring losses in disc resonators with epoxy cladding

Transmission loss induced by epoxy claddings on $GaAs$ nanoscale structures has not previously been explored. While being a means towards bridging metal wires, the epoxy design in itself poses opportunities for new designs of nanoscale quantum circuits. By covering a large area of a device with cladding, the epoxy structure can potentially hold the entire device, thus rendering the use of tethers, as briefly discussed in Chp. 3, obsolete. In order to investigate the effects of large epoxy claddings, multiple epoxy designs have been fabricated on both disc resonators and straight nanobeam waveguides. As the main objective within this chapter is to characterise and compare disc resonators with and without epoxy claddings, a summary and discussion of the work done with straight nanobeam waveguides can be found in Appendix D.

For the disc resonators, the parameter space of Epoxy Mask includes varying designs of epoxy cladding as well as metal deposition. The discs are fabricated with a radius ranging from $r = 3.15$ μm to $r = 4$ μm and a constant gap size and waveguide tapering width at $d = 100$ nm and $w = 200$ nm, respectively. We introduce a shorthand notation to describe the different structures within the mask design consisting of EPO_n and MET_m, epoxy design and the metal design, respectively. Here, $n = \{0, 1, 2, 3\}$ and $m = \{0, 1, 2\}$, and the corresponding designs are depicted in Fig. 6.1. The mask contains several reference devices, meaning the well-characterised bare disc resonators without epoxy or metal deposition

as depicted in Fig. 6.1a, in order to compare the new devices under investigation[1]. Using the shorthand notation the reference structures are referred to as EPO_0MET_0.

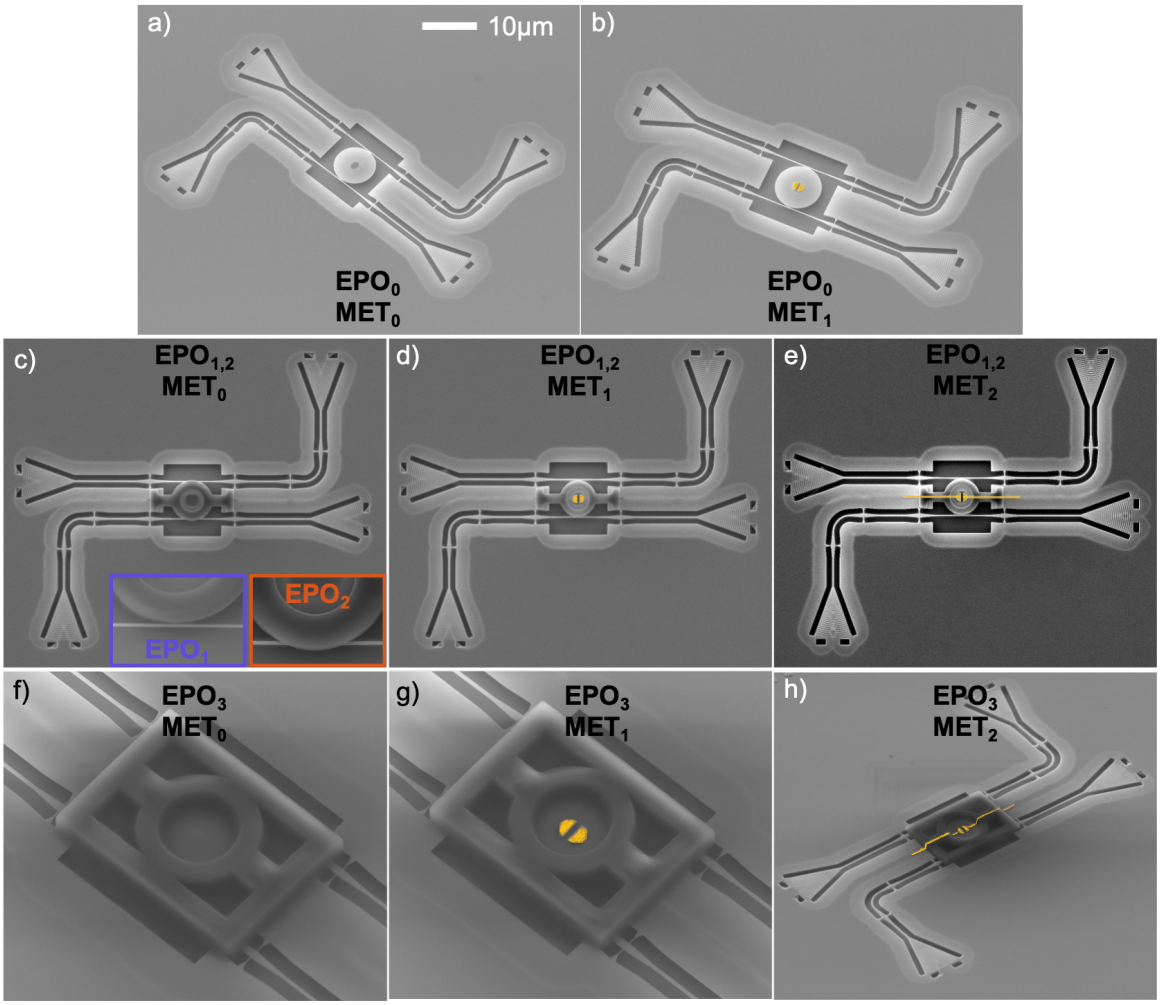

Figure 6.1.: SEM images of full mask of successfully fabricated disc resonators with varying amount of epoxy and metal. 4 designs of epoxy, $EPO_{0,1,2,3}$, were applied to the resonators, while 3 designs of metal, $MET_{0,1,2}$ (false-coloured in yellow), were deposited. Here, EPO_0 indicates no epoxy deposited on devices (a,b) while EPO_1 indicates a donut corresponding to the size of the disc resonator (c,d,e). EPO_2 indicates a donut larger than the disc, thus overlapping with the access waveguide (c,d,e). The difference is seen by the purple and orange inset on (c). EPO_3 indicates a large epoxy structure including a donut and beams along both access waveguides (f,g,h). MET_0 indicates no metal deposition on the device (a,c,f). MET_1 indicates only pads deposited on the discs (b,d,g). Finally, MET_2 indicates metal wires across the epoxy claddings (e,h).

The parameter space is designed such that it is possible to determine whether a significant loss is introduced by either:

- **An increasing amount of epoxy.** As the epoxy claddings have a higher refractive index from the surrounding air or vacuum, the confinement of the optical mode is potentially reduced. The

[1] We cannot directly compare results of this mask to previously characterised devices as the wafers differ, which can lead to a difference in quality factors.

interface between air and epoxy can furthermore serve as a point of scattering for the optical mode.

- **Metal deposition on the disc.** As gold has a high absorption coefficient, proximity between the optical mode and the deposited gold on the disc can lead to absorption losses. As the fundamental mode is shown to propagate in the perimeter of the disc, we assume only higher order modes would be affected by the pads in the center of the disc.

- **Metal wires on top of epoxy claddings.** In line with the proximity dependent absorption loss mentioned above, a wire crossing the region of the fundamental mode can introduce absorption losses.

From Fig. 6.1 we see that the largest epoxy design is given by EPO_3, and that the epoxy cladding covers both the perimeter of the disc as well as the tapered waveguide region. Fig. 6.2 depicts the resonant transmission measured at bus port of three individual disc resonators with epoxy design EPO_3. From the figure it is clear, that while there is a high transmission from excitation port to bus port with counts in the order of 10^5, there is no observable cavity response from the devices, meaning that we do not measure any dips in transmission.

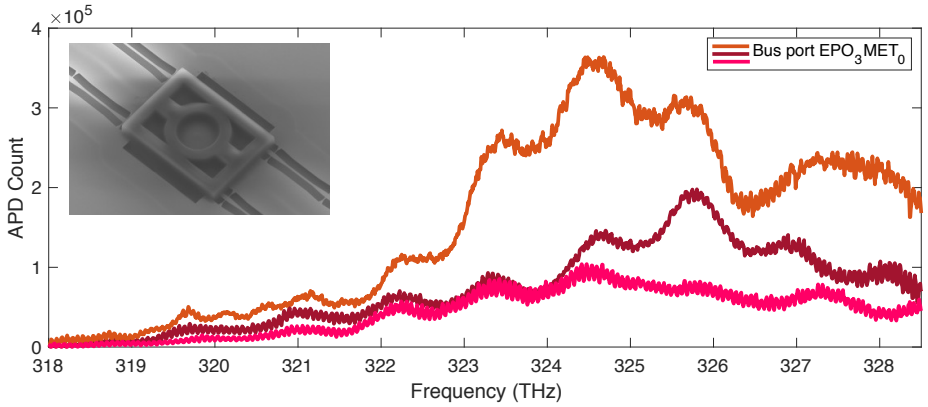

Figure 6.2.: Transmission through three individual disc resonators with epoxy design EPO_3 measured at bus port.

The lack of cavity response can be due to an insufficient underetching of the device. Following the fabrication procedure presented in Sec. 3.3, the etching of the sacrificial *AlGaAs*-layer is completed. The extent of the underetch is determined by the amount of time the chip is immersed in acid. The duration has been optimised for these devices and amounts to ≈ 50 s and results in an underetch of ≈ 3 μm. In the inset of Fig. 6.2 is a zoom-in of an EPO_3 device. Distinct from the other epoxy designs presented in Fig. 6.1a-e, we see no indications of an *AlGaAs*-pillar at the center of the disc. This implies that the disc has not not been adequately suspended, leading to a poor or non-existing cavity-coupling. Ultimately, this lead to full transmission from excitation port to bus port.

From Fig. 6.1c-e we do, however, observe the characteristic *AlGaAs*-pillar. Depicted in Fig. 6.3 are two examples of resonant transmission frequency scans from epoxy cladded devices. Similar to frequency scans previously presented in this thesis we are able to observe fundamental and higher order

radial modes in the cavity, separated by their respective FSR. By scanning a vast number of devices and fitting the observed cavity modes to a Lorentzian lineshape given by Eq. (2.2) we are able to plot the distribution of cavity Q-factors in Fig. 6.3b. Here, we see that the average Q-factor for disc resonators without epoxy, EPO_0, is given by $\bar{Q} = 10400$, and a standard deviation of $\sigma = 7000$. This is indeed comparable to the devices from Second Mask. Neither metal pads on the discs nor metal wires crossing over the discs show features of affecting the cavity modes. In the histogram we have combined structures EPO_1 and EPO_2 along with all metal designs, as the difference in cavity Q-factors was imperceptible. Structures with epoxy have an average Q-factor of $\bar{Q} = 8000$, and a standard deviation of $\sigma = 7200$, thereby differing marginally from the reference structures. Both histograms have been fitted to a Gaussian distribution as seen in the figure. The variance of both curves is broad, indicating that the difference in average Q-factor is not significant. Based on the data depicted in Fig. 6.3b we suspect epoxy cladded disc resonators to have higher losses than the bare structures, thus introducing an on average lower Q-factor. A thorough study including epoxy cladded concentric waveguides can potentially determine the magnitude of loss introduced by the claddings [59].

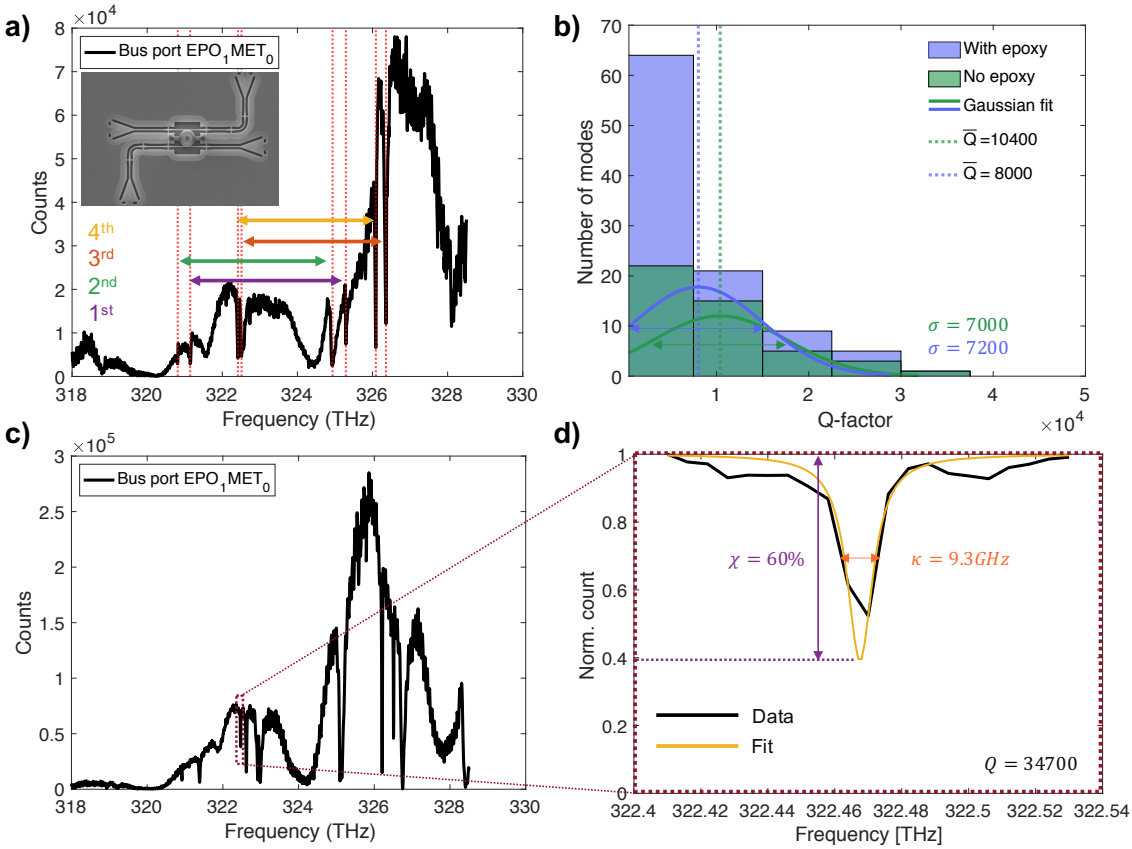

Figure 6.3.: Data analysis of Epoxy Mask a) CW-laser frequency scan of EPO_1MET_0 epoxy structure with collection at bus port. Clear cavity modes are present and their modal order indicated by the arrows. b) Histogram of Q-factors for devices with and without epoxy along with Gaussian fits. The epoxy parameter $n = 3$ is not included. c) CW-laser frequency scan of another EPO_1MET_0 epoxy structure. A cavity mode is marked and zoomed in on in d) where a Lorentzian fit estimates a mode extinction of $\chi = 60\%$ and a Q-factor of $Q = 34700$.

From the histogram in Fig. 6.3b we see that we are still able to observe high cavity Q-factors (> 30000) for devices with epoxy claddings. Depicted in Fig. 6.3c is a resonant transmission frequency scan of a device identical to the device used in Fig. 6.3a, EPO_1MET_0. We notice that the resonance frequencies of the cavity modes share high resemblance between the two devices. The cavity mode marked with red is depicted in a zoom-in in Fig. 6.3d. The cavity mode is fitted to have an extinction of $\chi = 60\%$ and a cavity linewidth of $\kappa = (9.3 \pm 0.6)$ GHz, leading to a cavity Q-factor of $Q = 34700$. While we routinely measure Q-factors above 20000, the extinction of the high-Q modes tends to be low due to weak coupling, as discussed in Sec. 2.1.3. It is therefore possible that modes of higher Q-factors are present, but that the resolution of the frequency scans is not high enough.

In conclusion, we have observed reproducible cavity effects in suspended epoxy cladded disc resonators. By analysing Q-factors of the cavity modes in structures with and without epoxy claddings, we find that the loss of optical mode introduced by the epoxy structures is sufficiently small, and that devices show high Q-factors averaging at $\bar{Q} = 8000$ for devices with epoxy and $\bar{Q} = 10400$ for devices without epoxy.

Conclusions and Outlook

7

We have within this thesis outlined a theoretical foundation for whispering gallery modes in a quantum dot-embedded disc resonator with access waveguides. A four-port device was designed, fabricated and ultimately optically characterised. The disc resonators within this thesis show average cavity quality factors of $Q \approx 10000$ while maximal quality factors > 30000 have been measured.

We focus on a specific cavity-quantum dot coupling in a cavity mode at $f = 325.9$ THz with linewidth $\kappa/2\pi = 37$ GHz. From power saturation and lifetime measurements of the quantum dot we measure a Purcell enhancement of $F = (6.9 \pm 0.9)$, a cavity-emitter emission efficiency of $\beta = (0.87 \pm 0.01)$ and a coupling strength of $g/2\pi = (2.5 \pm 0.3)$ GHz. We furthermore show coherent routing between bus port and drop port of single-photon emission from the coupled quantum dot. The quantum dot is spectrally tuned across the cavity using temperature tuning. While the quantum dot is on resonance, a peak routing efficiency of $\Delta I = (23 \pm 3)\%$ is measured at saturation level $S = 1.5$.

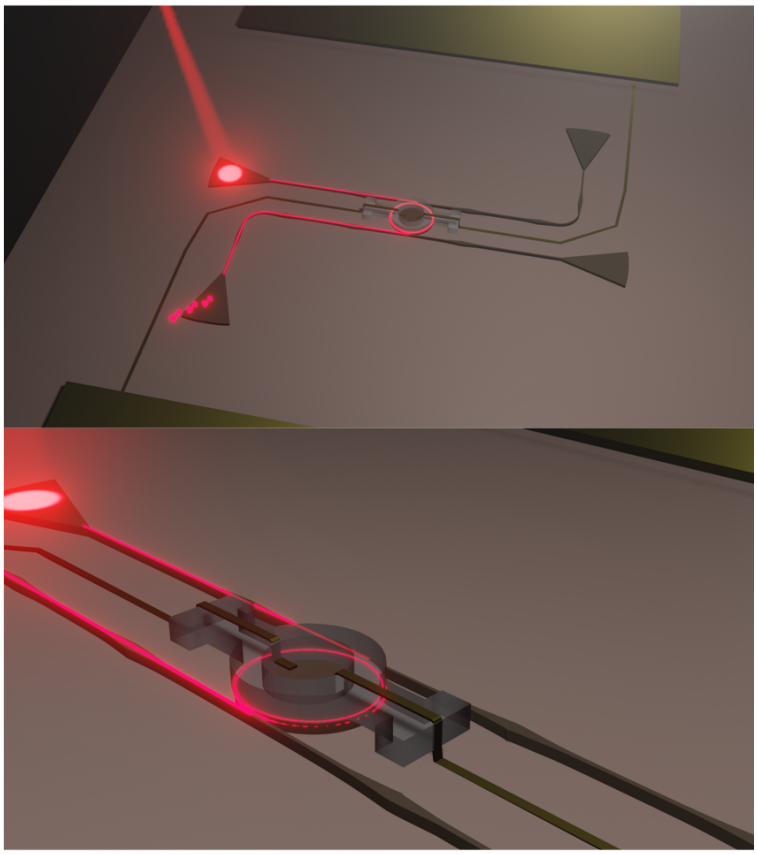

Figure 7.1.: Optical routing in electrically gated disc resonator. Large bonding pads with wires (gold) are connected to the center of the disc via epoxy in order to spectrally tune the resonance of the embedded quantum dots.

Theoretical modelling predicts a peak routing efficiency of $\Delta I = (56 \pm 3)\%$ when evading charge noise from spectral diffusion ($\sigma_{\mathrm{sd}} = 0$ GHz) and a peak routing efficiency of $\Delta I = (98 \pm 2)\%$ when additionally approaching the low-power regime ($\sigma_{\mathrm{sd}} = 0$ GHz and $S = 0$). Within this work we propose a method for eliminating charge noises by fabricating the disc resonators using a p-i-n junction wafer and electrically contacting the isolated discs. This further allows control of the spectral resonance of the quantum dot. Within this work we have optimised the fabrication procedure for metal wires crossing epoxy claddings, in order to guide metal wires from wafer to disc. The successfully fabricated epoxy cladded disc resonators were optically characterised and average quality factors for devices with epoxy were measured at $Q \approx 8000$, indicating that the optical loss associated with the epoxy is not severe. A succession of the optimisation of the metal wire bridges would be the realisation of electrically contacted disc resonators on a p-i-n junction wafer as depicted in Fig. 7.1, where we expect routing efficiency to significantly increase.

The fabrication of device-wire intersections utilised by epoxy claddings not only serves as a sequent to the device-specific challenges of electrically contacting isolated discs, but also paves the way for the upscaling of integrated planar nanophotonic circuits. An upscaling of highly efficient photonic networks is an advancement of quantum technology that will lead the way towards a globally incorporated quantum network, ultimately resulting in broadly distributive secure long-distance communication.

Bibliography

8

[1] S. Wehner, D. Elkouss, and R. Hanson, „Quantum internet: A vision for the road ahead“, *Science*, vol. 362, p. 6412, 2018 (cit. on p. 1).

[2] J. P. Dowling and G. J. Milburn, „Quantum technology: The second quantum revolution“, *Philos. Trans. R. Soc. London. Ser. A Math. Phys. Eng. Sci.*, vol. 361, p. 1655, 2003 (cit. on p. 1).

[3] H. J. Kimble, „The quantum internet“, *Nature*, vol. 453, p. 1023, 2008 (cit. on p. 1).

[4] R. Horodecki, P. Horodecki, M. Horodecki, and K. Horodecki, „Quantum entanglement“, *Reviews of mordern physics*, vol. 81, p. 865, 2009 (cit. on p. 1).

[5] A. S. Cacciapuoti, M. Caleffi, R. V. Meter, and L. Hanzo, „When Entanglement Meets Classical Communications: Quantum Teleportation for the Quantum Internet“, *IEEE Transactions on communications*, vol. 68, p. 3808, 2020 (cit. on p. 1).

[6] W. K. Wootters and W. H. Zurek, „The no-cloning theorem“, *Physics Today*, vol. 62, pp. 76–77, 2009 (cit. on p. 1).

[7] J. L. O'Brien, A. Furusawa, and J. Vučković, „Photonic quantum technologies“, *Nature Photonics*, vol. 3, p. 687, 2009 (cit. on p. 1).

[8] J. Borregaard, A. S. Sørensen, and P. Lodahl, „Quantum networks with deterministic spin–photon interfaces“, *Adv. Quant. Tech.*, vol. 2, p. 1 800 091, 2019 (cit. on pp. 1, 10).

[9] L.-M. Duan and H. J. Kimble, „Scalable photonic quantum computation through cavity-assisted interactions“, *Phys. Rev. Lett.*, vol. 92, p. 127 902, 2004 (cit. on p. 1).

[10] R. Uppu, L. Midolo, X. Zhou, J. Carolan, and P. Lodahl, „Single-photon quantum hardware: Towards scalable photonic quantum technology with quantum advantage“, *ArXiv*, p. 2103.001110v1, 2021 (cit. on pp. 1, 6).

[11] L. Midolo, A. Schliesser, and A. Fiore, „Nano-opto-electro-mechanical systems“, *Nature Nanotechnology*, vol. 13, pp. 11–18, 2018 (cit. on p. 1).

[12] K. M. Rosfjord, J. K. W. Yang, E. A. Dauler, A. J. Kerman, V. Anant, B. M. Voronov, G. N. Goltsman, and K. K. Berggren, „Nanowire single-photon detector with an integrated optical cavity and anti-reflection coating“, *Optics Express*, vol. 14, pp. 527–534, 2006 (cit. on p. 1).

[13] F. T. Pedersen, Y. Wang, C. T. Olesen, *et al.*, „Near transform-limited quantum dot linewidths in a broadband photonic crystal waveguide“, *ACS Photonics*, vol. 7, pp. 2343–2349, 2020 (cit. on pp. 1, 18, 19, 25).

[14] J.-H. Kim, S. Aghaeimeibodi, J. Carolan, D. Englund, and E. Waks, „Hybrid integration methods for on-chip quantum photonics“, *Optica*, vol. 7, p. 291, 2020 (cit. on p. 1).

[15] A. H. Atabaki, S. Moazeni, F. Pavanello, *et al.*, „Integrating photonics with silicon nanoelectronics for the next generation of systems on a chip“, *Nature*, vol. 556, p. 350, 2018 (cit. on pp. 2, 25).

[16] B. E. A. Saleh and M. Teich, *Fundamentals of Photonics*, 2nd ed. Wiley, 2007 (cit. on p. 5).

[17] C. C. Gerry and P. L. Knight, *Introductory Quantum Optics*, 3rd ed. Cambridge, 2008 (cit. on pp. 5, 7).

[18] P. Meystre and M. Sargent, *Elements of Quantum Optics*, 1st ed. Springer-Verlag, 1991 (cit. on p. 5).

[19] M. S. A. Hilico, E. Will, J. Volz, and A. Rauschenbeutel, „Quantum optical circulator controlled by a single chirally coupled atom“, *Science*, vol. 354, pp. 1577–1580, 2016 (cit. on pp. 5, 10).

[20] D. Wang, H. Kelkar, D. Martin-Cano, D. Rattenbacher, A. Shkarin, T. Utikal, S. Götzinger, and V. Sandoghdar, „Turning a molecule into a coherent two-level quantum system“, *Nature Physics*, vol. 15, pp. 483–489, 2019 (cit. on p. 5).

[21] A. W. Bruch, C. Xiong, B. Leung, M. Poot, J. Han, and H. X. Tang, „Broadband nanophotonic waveguides and resonators based on epitaxial gan thin films“, *Appl. Phys. Lett.*, vol. 107, p. 141 113, 2015 (cit. on pp. 5, 17).

[22] M. Soltani, S. Yegnanarayanan, and A. Adibi, „Ultra-high q planar silicon microdisk resonators for chip-scale silicon photonics“, *Optics Express*, vol. 15, pp. 4694–4704, 2007 (cit. on p. 6).

[23] D. Rafizadeh, J. P. Zhang, S. C. Hagness, A. Taflove, K. A. Stair, and S. T. Ho, „Waveguide-coupled AlGaAs/GaAs microcavity ring and disk resonators with high finesse and 21.6-nm free spectral range“, *Optics Letters*, vol. 22, p. 184, 1997 (cit. on pp. 6, 17, 39).

[24] E. Peter, P. Senellart, D. Martrou, A. Lemaitre, J. Hours, J. M. Gérard, and J. Bloch, „Exciton-photon strong-coupling regime for a single quantum dot embedded in a microcavity“, *PRL*, vol. 95, p. 067 401, 2005 (cit. on pp. 6, 17, 39).

[25] P. Michler, A. Kiraz, L. Zhang, C. Becher, E. Hu, and A. Imamoglu, „Laser emission from quantum dots in microdisk structures“, *Appl. Phys. Lett.*, vol. 77, pp. 4694–4704, 2000 (cit. on pp. 6, 39).

[26] B. Gayral, J. M. Gérard, B. Sermage, A. Lemaître, and C. Dupuis, „Time-resolved probing of the purcell effect for InAs quantum boxes in GaAs microdisks“, *Appl. Phys. Lett.*, vol. 78, pp. 2828–2830, 2001 (cit. on pp. 6, 39).

[27] E. M. Purcell, H. C. Torrey, and R. V. Pound, „Resonance absorption by nuclear magnetic moments in a solid“, *PRL*, vol. 69, p. 37, 1946 (cit. on p. 9).

[28] B. Romeira and A. Fiore, „Purcell effect in the stimulated and spontaneous emission rates of nanoscale semiconductor lasers“, *IEEE Journal of Quantum Electronics*, vol. 54, 2018 (cit. on p. 9).

[29] J. Johansen, S. Stobbe, I. S. Nikolaev, T. Lund-Hansen, P. T. Kristensen, J. M. Hvam, W. L. Vos, and P. Lodahl, „Size dependence of the wavefunction of self-assembled InAs quantum dots from time-resolved optical measurements“, *Phys. Rev. B*, vol. 77, p. 073 303, 2008 (cit. on p. 9).

[30] F. Albert, S. Stobbe, C. Schneirder, T. Heindel, S. Reitzenstern, S. Höfling, P. Lodahl, L. Worschech, and A. Forchel, „Quantum efficiency and oscillator strength of site-controlled InAs quantum dots“, *Applied Physics Letters*, vol. 96, p. 151 102, 2010 (cit. on pp. 9, 55).

[31] S. Strauf, N. G. Stoltz, M. T. Rakher, L. A. Coldren, P. M. Petroff, and D. Bouwmeester, „High-frequency single-photon source with polarization control“, *Nature Photonics*, vol. 1, pp. 704–708, 2007 (cit. on p. 9).

[32] K. Srinivasan and O. Painter, „Linear and nonlinear optical spectroscopy of a strongly coupled microdisk–quantum dot system“, *Nature*, vol. 450, pp. 862–866, 2007 (cit. on p. 9).

[33] T. C. Ralph, I. Söllner, S. Mahmoodian, A. G. White, and P. Lodahl, „Photon sorting, efficient bell measurements, and a deterministic controlled-z gate using a passive two-level nonlinearity“, *Phys. Rev. Lett.*, vol. 114, p. 173 603, 2015 (cit. on p. 9).

[34] P. Lodahl, S. Mahmoodian, and S. Stobbe, „Interfacing single photons and single quantum dots with photonic nanostructures“, *Rev. Mod. Phys.*, vol. 87, p. 347, 2015 (cit. on pp. 10, 18, 19, 25, 37, 44, 46, 48).

[35] L. Scarpelli, B. Lang, F. Masia, *et al.*, „99% beta factor and directional coupling of quantum dots to fast light in photonic crystal waveguides determined by spectral imaging“, *Physical Review B*, vol. 100, p. 035 311, 2019 (cit. on p. 10).

[36] D. Wang, H. Kelkar, D. Martin-Cano, T. Utikal, S. Götzinger, and V. Sandoghdar, „Coherent coupling of a single molecule to a scanning fabry-perot microcavity“, *Phys. Rev. X*, vol. 7, p. 021 014, 2017 (cit. on p. 10).

[37] T. Hümmer, F. J. Garcia-Vidal, L. Martin-Moreno, and D. Zueco, „Weak and strong coupling regimes in plasmonic qed“, *Physical Review B*, vol. 87, p. 115 419, 2013 (cit. on p. 10).

[38] V. Loo, L. Lanco, A. Lemaître, I. Sagnes, O. Krebs, P. Voisin, and P. Senellart, „Quantum dot-cavity strong-coupling regime measured through coherent reflection spectroscopy in a very high-q micropillar“, *Appl. Phys. Lett.*, vol. 97, p. 241 110, 2010 (cit. on p. 10).

[39] G. Khitrovaa, H. M. Gibbs, M. Kira, S. W. Koch, and A. Scherer, „Vacuum Rabi splitting in semiconductors“, *Nature*, vol. 2, pp. 81–90, 2006 (cit. on p. 10).

[40] A. Brooks, X.-L. Chu, Z. Liu, R. Schott, A. Ludwig, A. D. Wieck, L. Midolo, P. Lodahl, and N. Rotenberg, „An integrated whispering-gallery-mode resonator for solid-state coherent quantum photonics“, *ArXiv*, vol. 2107.12188v2, 2021 (cit. on pp. 10, 38).

[41] A. Aufféves-Garnier, C. Simon, J.-M. Gérard, and J.-P. Poizat, „Giant optical nonlinearity induced by a single two-level system interacting with a cavity in the purcell regime“, *Phys. Rev. A*, vol. 75, pp. 1–16, 2007 (cit. on pp. 10, 11).

[42] A. Kiraz, P. Michler, C. Becher, B. Gayral, A. Imamoglu, L. Zhang, and E. Hu, „Cavity-quantum electrodynamics using a single InAs quantum dot in a microdisk structure“, *Appl. Phys. Lett.*, vol. 78, p. 3932, 2001 (cit. on pp. 10, 19).

[43] H. L. Jeannic, T. Ramos, S. F. Simonsen, *et al.*, „Experimental reconstruction of the few-photon nonlinear scattering matrix from a single quantum dot in a nanophotonic waveguide“, *Phys. Rev. Lett.*, vol. 126, p. 023 603, 2021 (cit. on pp. 14, 19, 51, 53).

[44] A. Yariv, „Critical coupling and its control on optical waveguide-ring resonator systems“, *IEEE Photonics Technology Letters*, vol. 14, 2002 (cit. on p. 14).

[45] L. Ding, P. Senellart, A. Lemaître, S. Ducci, G. Leo, and I. Favero, „GaAs micro-nanodisks probed by a looped fiber taper for optomechanics applications“, *Proc. SPIE*, vol. 7712, p. 771 211, 2010 (cit. on p. 15).

[46] V. Van, P. P. Absil, J. V. Hryniewicz, and P.-T. Ho, „Proopagation Loss in Single-Mode GaAs-AlGaAs Microring Resonators: Measurement and Model“, *Journal of lightwave technology*, vol. 19, p. 1734, 2001 (cit. on p. 17).

[47] C. Xiong, W. Pernice, K. K. Ryu, C. Schuck, K. Y. Fong, T. Palacios, and H. T. Tang, „Integrated gan photonic circuits on silicon (100) for second harmonic generation“, *Optics Express*, vol. 19, p. 10 462, 2011 (cit. on p. 17).

[48] D. Martin-Cano, H. R. Haakh, and N. Rotenberg, „Chiral emission into nanophotonic resonators“, *ACS Photonics*, vol. 6, pp. 961–966, 2019 (cit. on p. 17).

[49] C. Sauvan, J. P. Hugonin, I. S. Maksymov, and P. Lalanne, „Theory of the spontaneous optical emission of nanosize photonic and plasmon resonators“, *Phys. Rev. Lett.*, vol. 110, p. 237 401, 2013 (cit. on p. 18).

[50] M. Schwartz, E. Schmidt, U. Rengstl, F. Hornung, S. Hepp, S. L. Portalupi, K. Ilin, M. Jetter, M. Siegel, and P. Michler, „Fully on-chip single-photon hanbury-brown and twiss experiment on a monolithic semiconductor–superconductor platform“, *Nano Letters*, vol. 18, pp. 6892–6897, 2018 (cit. on p. 18).

[51] X. Zhou, R. Uppu, Z. Liu, C. Papon, R. Schott, A. D. Wieck, A. Ludwig, P. Lodahl, and L. Midolo, „On-chip nanomechanical filtering of quantum-dot single-photon sources“, *Laser & photonics reviews*, vol. 14, p. 1 900 404, 2020 (cit. on pp. 18, 21, 25).

[52] R. Uppu, J. H. Prechtel, A. V. Kuhlmann, J. Houel, S. R. Valentin, and R. J. W. A. D. Wieck, „Ultra-low charge and spin noise in self-assembled quantum dots“, *Journal of Crystal Growth.*, vol. 477, pp. 193–196, 2017 (cit. on p. 18).

[53] E. Rosencher and B. Vinter, *Optoelectronics*, 1st ed. Cambridge University Press, 2002 (cit. on p. 18).

[54] Y. Wang, R. Uppu, X. Zhou, C. Papon, S. Scholz, A. D. Wieck, A. Ludwig, P. Lodahl, and L. Midolo, „Electroabsorption in gated GaAs nanophotonic waveguides“, *Appl. Phys. Lett.*, vol. 118, p. 131 106, 2021 (cit. on p. 18).

[55] D. Englund, A. Faraon, I. Fushman, N. Stoltz, P. Petroff, and J. Vučković, „Controlling cavity reflectivity with a single quantum dot“, *Nature*, vol. 450, pp. 857–861, 2007 (cit. on p. 19).

[56] S. Sun, H. Kim, G. S. Solomon, and E. Waks, „Strain tuning of a quantum dot strongly coupled to a photonic crystal cavity“, *Appl. Phys. Lett.*, vol. 103, p. 151 102, 2013 (cit. on p. 19).

[57] A. Faraon, D. Englund, I. Fushman, N. Stoltz, P. Petroff, and J. Vučković, „Local quantum dot tuning on photonic crystal chips“, *Appl. Phys. Lett.*, vol. 90, p. 213 110, 2007 (cit. on p. 19).

[58] X. Zhou, I. Kulkova, T. Lund-Hansen, S. L. Hansen, P. Lodahl, and L. Midolo, „High-efficiency shallow-etched grating on GaAs membranes for quantum photonic applications“, *Appl. Phys. Lett.*, vol. 113, p. 251 103, 2018 (cit. on pp. 21, 23).

[59] C. Papon, X. Zhou, H. Thyrrestrup, Z. Liu, S. Stobbe, R. Schott, A. D. Wieck, A. Ludwig, P. Lodahl, and L. Midolo, „Nanomechanical single-photon routing“, *Optica*, vol. 6, pp. 524–530, 2019 (cit. on pp. 21, 60).

[60] G. J. Iafrate, C. F. C. Jr, and J. Kwiatkowski, „Proximity Effects in Electron Beam Lithography“, ARMY ELECTRONICS RESEARCH and DEVELOPMENT COMMAND FORT MONMOUTH NJ ..., Tech. Rep., 1981 (cit. on p. 21).

[61] F. Pagliano, Y. Cho, T. Xia, F. v. Otten, R. Johne, and A. Fiore, „Dynamically controlling the emission of single excitons in photonic crystal cavities“, *Nature Communications*, vol. 5, pp. 1–6, 2014 (cit. on p. 25).

[62] S. K. Martham, K. K. Nan, and M. M. Shahimin, „Refractive Index Modification of SU-8 Polymer Based Waveguide Via Fabrication Parameters“, *IEEE Student Conference on Research and Development*, pp. 1–5, 2014 (cit. on p. 26).

[63] P. Tighineanu, C. L. Dreeßen, C. Flindt, P. Lodahl, and A. S. Sørensen, „Phonon decoherence of quantum dots in photonic structures broadening of the zero-phonon line and the role of dimensionality“, *Phys. Rev. Lett.*, vol. 120, p. 257 401, 2018 (cit. on p. 46).

[64] A. Javadi, I. Söllner, M. Arcari, *et al.*, „Single-photon non-linear optics with a quantum dot in a waveguide“, *Nat. Commun.*, vol. 6, p. 8655, 2015 (cit. on p. 48).

[65] A. Crépieux, „Electronic heat current fluctuations in a quantum dot“, *Physical Review B*, vol. 103, p. 045 427, 2021 (cit. on p. 49).

[66] C., Santori, D. Fattal, J. Vučkovic, G. S. Solomon, and Y. Yamamoto, „Indistinguishable photons from a single-photon device“, *Nature*, vol. 419, pp. 594–597, 2002 (cit. on p. 53).

[67] J. Hendrickson, M. Helfrich, M. Gehl, D. Hu, D. Schaadt, M. Wegener, B. Richards, H. Gibbs, and G. Khitrova, „Development of site-controlled quantum dot arrays acting as scalable sources of indistinguishable photons“, *Appl. Phys. Lett. Photonics*, vol. 5, p. 096 107, 2020 (cit. on p. 55).

[68] J. Große, M. von Helversen, A. Koulas-Simos, M. Hermann, and S. Reitzenstein, „Development of site-controlled quantum dot arrays acting as scalable sources of indistinguishable photons“, *Appl. Phys. Lett. Photonics*, vol. 5, p. 096 107, 2020 (cit. on p. 55).

[69] T. Pregnolato, X.-L. Chu, T. Schröder, R. Schott, A. D. Wieck, A. Ludwig, P. Lodahl, and N. Rotenberg, „Deterministic positioning of quantum dots in nanophotonic waveguides“, *Appl. Phys. Lett. Photonics*, vol. 5, p. 086 101, 2020 (cit. on p. 55).

[70] P. Schnauber, J. Schall, S. Bounouar, *et al.*, „Deterministic integration of quantum dots into on-chip multimode interference beamsplitters using in situ electron beam lithography“, *Nano Lett.*, vol. 18, pp. 2336–2342, 2018 (cit. on p. 55).

Convolution of cavity lineshape and spectral diffusion

A

The transmission lineshape of the coupled cavity-emitter system discussed in Sec. 2.1.2 is depicted in Fig. 2.3. The characteristic transmission dip is caused by the coherent interaction with the emitter. The quantum dots embedded in the disc resonators are subject to a finite amount of charge noise which ultimately causes a linewidth broadening of the transmission dip. The spectral diffusion solely affects the quantum dot and not the cavity loss rate. However, in Fig. A.1 it is clear that by convoluting the entire cavity with a spectral diffusion in the order of $\sigma_{\mathrm{sd}} = 1.5$ GHz the cavity lineshape is barely affected, which is visible from the residuals being less than 1% in the center of the cavity. The residuals increase to $> 2\%$ towards the extremities of the cavity. We are however not able to distinguish the coherent interaction of the quantum dots at this detuning, making this issue quite obsolete.

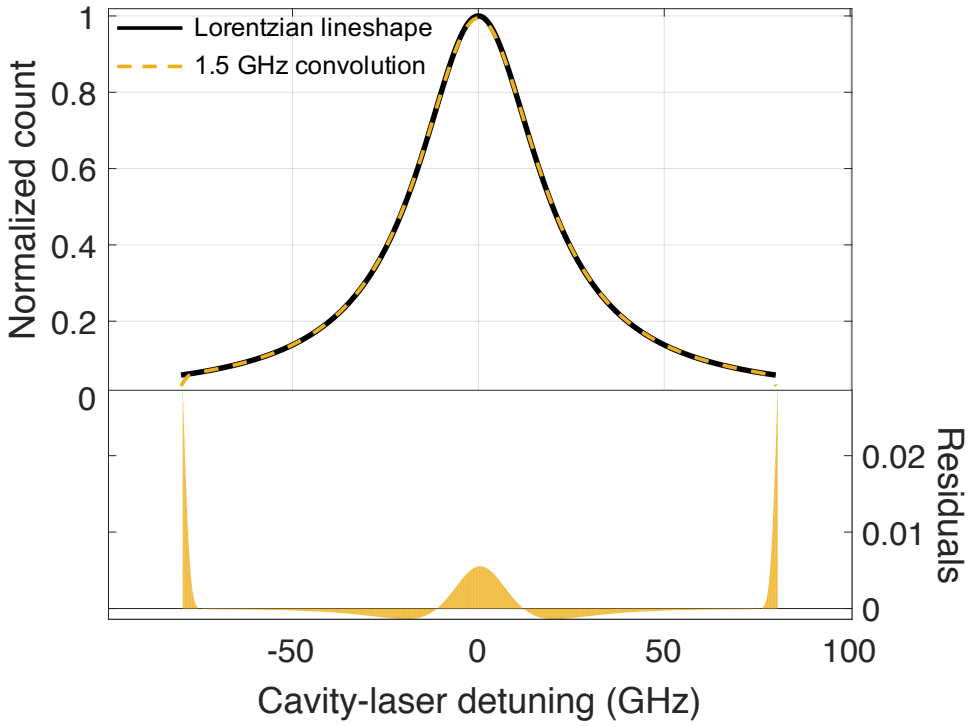

Figure A.1.: Convolution of bare cavity lineshape (black) with spectral diffusion $\sigma_{\mathrm{sd}} = 1.5$ GHz (yellow). The residuals between the bare cavity and the convoluted cavity are below the normalised counts of the cavity.

Fabrication protocol

B

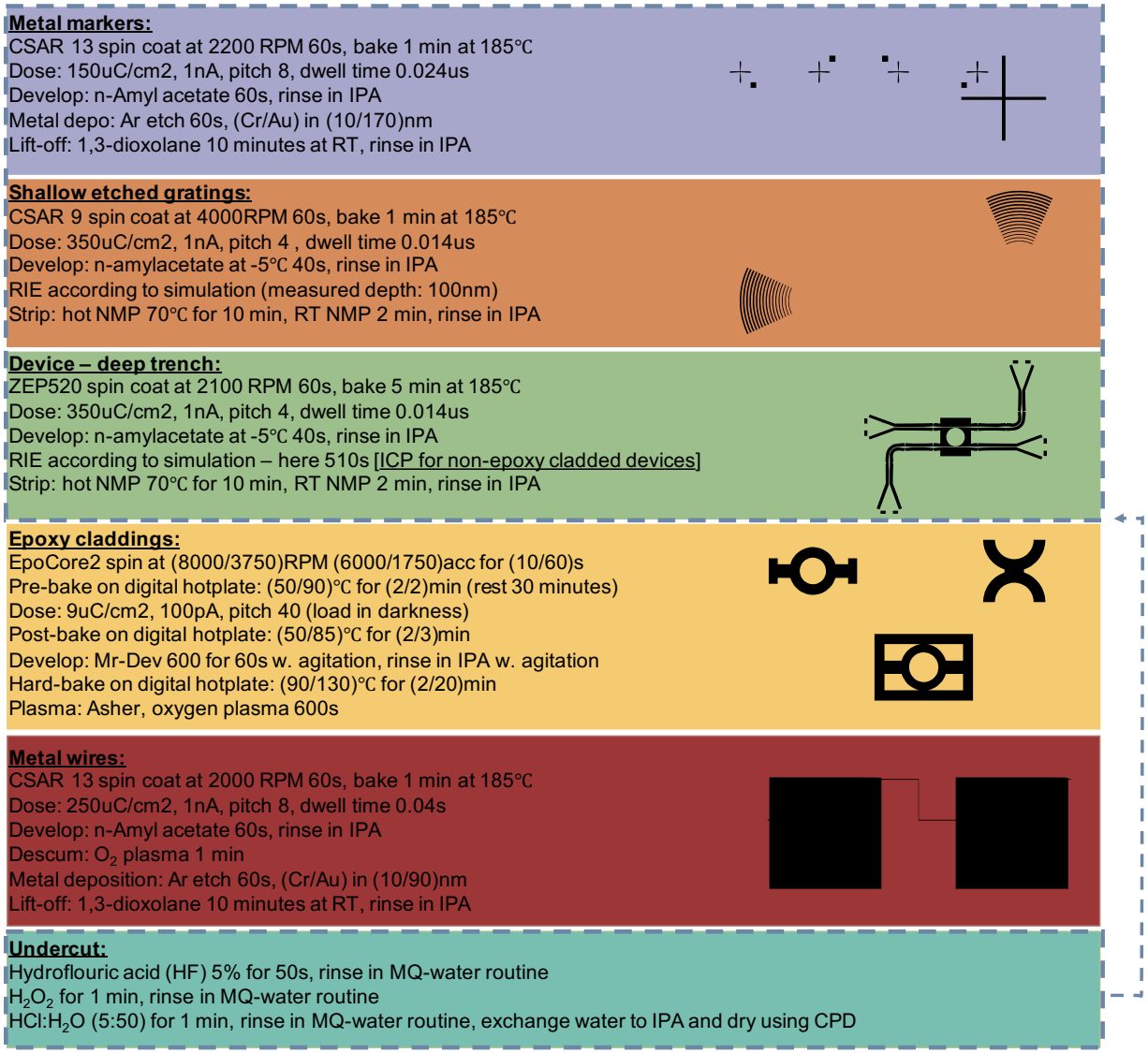

Figure B.1.: Fabrication protocol of photonic nanoscale devices. For epoxy cladded devices the protocol follows the protocol vertically downwards, while the non-epoxy cladded devices follows the protocol for the first three steps (purple, orange, green) after which the protocol jumps to the undercut (blue).

Measurements from First Mask

C

Measurements done on First Mask follow the same experimental setup as the remainder of the experiments, except that the laser source was a SuperK white light source. The white light source emits a broad band of near-infrared light. The laser was coupled into the devices through the gratings, and light was collected from both drop and bus port. As the out coupled light was also consist of a broad band, it was sent to the spectrometer. The resolution of the spectrometer is $\approx 1nm$ and was therefore not able to resolve the cavity modes. As resonant transmission with the CTL is far more time-consuming this was not chosen for the First Mask, as the purpose of this mask solely was to specify a working parameter space of the disc resonators.

Results from First Mask measurements are depicted in Fig. C.1. From Fig. C.1a we see a drop port measurement showing clear cavity response. The peaks are fitted to Lorentzian lineshapes, and the average Q-factor of this device is estimated at $Q = 500 \pm 200$. From the inset we see that exact copies of this device behave very similarly, showing cavity responses at the same wavelengths.

From Fig. C.1b we see both a bus port and a drop port measurement, and it is clear that the two ports are highly correlated.

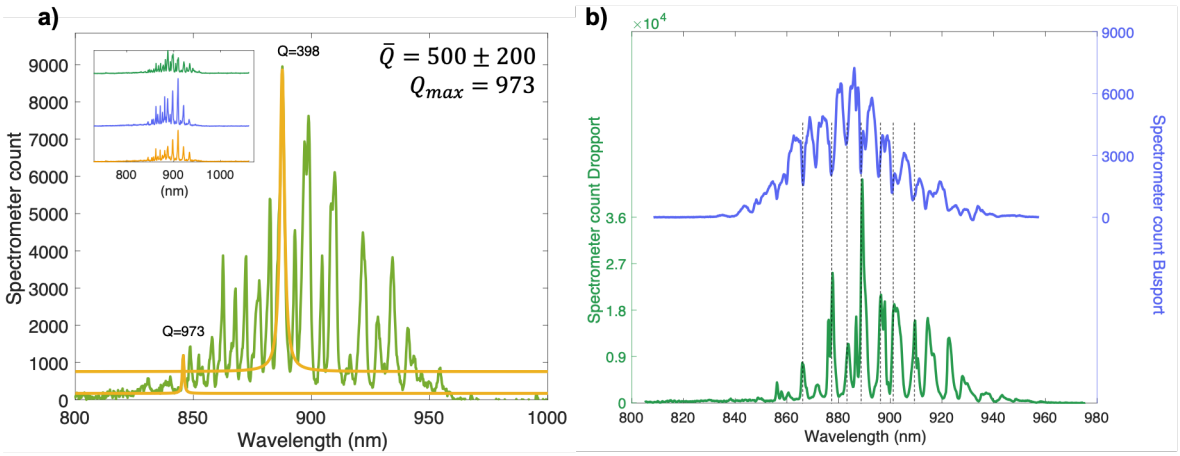

Figure C.1.: Data from white light source (SuperK) coupled to disc resonators measured with a spectrometer. a) Exemplary drop port data. Yellow lines show exemplary Lorentzian fits. The maximal Q-factor is $Q = 973 \pm 1$ while the average Q-factor for this device is $\bar{Q} = 500 \pm 200$. The inset shows data from three devices that are exact copies of the primary device. b) Data from a device at drop port (left) and bus port (right) showing the correlation between peaks in drop port and dips in bus port.

D

Epoxy claddings on straight nanobeam waveguides

The development of stable and reproducible epoxy claddings is important in regards to the upscaling of quantum photonic circuits, as the claddings serve as bridges for metal wires across intersections. Here, we present a design of epoxy claddings that potentially have a manyfold purpose: Bridging metal wires across device-wire intersections and retaining fully suspended devices. Depicted in Fig. D.1 are SEM images of straight nanobeam waveguides with and without epoxy claddings, along with transmission count rates.

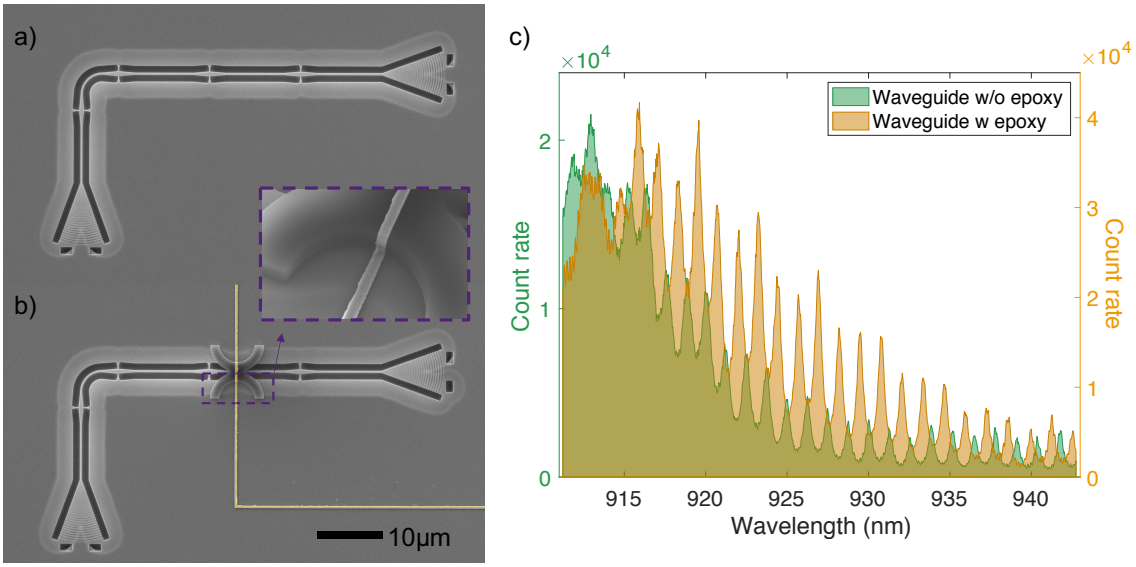

Figure D.1.: Transmission through straight nanobeam waveguides. a) SEM image of a nanobeam waveguide with in- and out-coupling grating. b) Epoxy cladded nanobeam waveguide. A wire (false coloured in yellow) is bridged across the waveguide. A zoom in indicates good metal continuity. c) ADP counts from transmission of near-infrared light through waveguides with (orange) and without (green) epoxy.

In Fig. D.1c we see that the transmission pattern through devices with and without epoxy is highly comparable. The absolute amount of counts is seen to be *higher* for the device with epoxy, which is due to in- and out-coupling differences from alignment variances. The high count rate of both types of devices indicates that the optical loss introduced from the claddings is not severe. Further tests to determine loss can entail several epoxy structures across one device as depicted in red in Fig. D.1b. A design of this nature can potentially replace the tethers of the device as the epoxy structures will adhere the suspended devices to the remainder of the wafer. It is, however, unclear whether the main source of loss is the presence of the epoxy along the path of mode propagation, or if it is the introduction of a scattering point at the beginning of each epoxy structure. This too will require further investigation.

"The most effective way to do it, is to do it."

- Amelia Earhart